

MINISTRY OF EDUCATION
FEDERAL UNIVERSITY OF RIO GRANDE DO SUL
GRADUATE PROGRAM IN MECHANICAL ENGINEERING

NEW WSGG CORRELATIONS ACCOUNTING FOR VARIATIONS ON THE MOLE
RATIO AND THE PARTIAL PRESSURE OF THE PARTICIPATING SPECIES

by

Alexandre Huberto Balbino Selhorst

Dissertation submitted for the Degree of
Master in Engineering

Porto Alegre, July 2020

MINISTÉRIO DA EDUCAÇÃO
UNIVERSIDADE FEDERAL DO RIO GRANDE DO SUL
PROGRAMA DE PÓS-GRADUAÇÃO EM ENGENHARIA MECÂNICA

NOVAS CORRELAÇÕES WSGG CONSIDERANDO VARIAÇÕES NA FRAÇÃO
MOLAR E PRESSÃO PARCIAL DAS ESPÉCIES PARTICIPANTES

por

Alexandre Huberto Balbino Selhorst

Dissertação submetida para obtenção do Título de
Mestre em Engenharia

Porto Alegre, Julho de 2020

NOVAS CORRELAÇÕES WSGG CONSIDERANDO VARIAÇÕES NA FRAÇÃO
MOLAR E PRESSÃO PARCIAL DAS ESPÉCIES PARTICIPANTES

por

Alexandre Huberto Balbino Selhorst

Engenheiro Mecânico

Dissertação submetida ao Corpo Docente do Programa de Pós-Graduação em Engenharia Mecânica, PROMEC, da Escola de Engenharia da Universidade Federal do Rio Grande do Sul, como parte dos requisitos necessários para a obtenção do Título de

Mestre em Engenharia

Área de Concentração: Fenômenos de Transporte

Orientador: Prof. Dr. Francis Henrique Ramos França

Aprovada por:

Prof. Dr. Hadi Bordbar Dep. of Civil Eng. / Aalto University

Prof. Dr. Fernando Marcelo Pereira PROMEC / UFRGS

Prof. Dr. Andrés Armando Mendiburu Zevallos PROMEC / UFRGS

Prof. Dr. Fernando Marcelo Pereira

Coordenador do PROMEC

Porto Alegre, Julho de 2020

I would rather have questions that can't be answered than answers that can't be questioned.

Richard Phillips Feynman
(1918 - 1988)

AGRADECIMENTOS

Agradeço ao meu orientador, Dr. Francis França, por todo apoio e orientação fornecidos, os quais transcenderam os limites de qualquer expectativa. Aos meus pais, por terem me apoiado, mesmo que de longe. A minha noiva, a qual me apoiou fora do âmbito acadêmico. Aos amigos de laboratório, os quais me ajudaram nas dúvidas que apareceram ao longo da execução desse trabalho. Aos colegas que iniciaram essa jornada junto comigo e foram de grande valor para o bom aproveitamento das disciplinas cursadas. Ao Conselho Nacional de Desenvolvimento Científico e Tecnológico (CNPq) pelo suporte financeiro.

RESUMO

Neste trabalho é proposto um método alternativo para se obter coeficientes para o modelo de soma-ponderada-de-gases-cinza (WSGG). Ainda que a literatura ofereça um número elevado de formulações aplicáveis para diferentes cenários, nenhuma delas analisa a influência da pressão parcial das espécies participantes no modelo WSGG na solução da equação da transferência radiativa (RTE). Além disso, também é apresentado um novo método para se obter coeficientes do modelo WSGG para problemas com variação na fração molar. São apresentados cinco diferentes conjuntos de correlações WSGG, cada um para seu respectivo cenário. O primeiro cenário lida com processos de combustão em atmosfera aberta e considera uma fração molar fixa com variação na pressão parcial ao longo do meio. São apresentadas duas correlações para esse cenário, para frações molares iguais a 1,0 e a 2,0. No segundo cenário, as correlações foram ajustadas para considerar a variação da fração molar ao longo do meio, uma situação usual em oxicombustão. As correlações são geradas a partir da emitância total, que são ajustadas a partir de dados obtidos do banco de dados spectral de alta resolução HITEMP-2010. No primeiro cenário, os espectros de absorção são extraídos do HITEMP-2010 para 9 diferentes pressões parciais e 23 temperaturas, sobre as quais são computadas diferentes emitâncias totais para 24 valores de uma variável que representa o produto entre a pressão parcial e o comprimento percorrido pela radiação ao longo do meio, $p_a S$. Para o segundo cenário são consideradas as mesmas quantidades de temperatura e $p_a S$, porém, a alteração não ocorre nas pressões parciais, mas na fração molar, para a qual são considerados 17 diferentes valores. Além desse ajuste, em uma nova abordagem, o intervalo da fração molar é dividido, dando origem a dois novos conjuntos de emitância total. O método proposto por Levenberg-Marquardt é empregado para efetuar o ajuste de coeficientes para todos os diferentes conjuntos de emitância. A acurácia das correlações resultantes é verificada através de uma comparação com resultados obtidos pela integração linha-por-linha em um domínio unidimensional. A equação da transferência radiativa é solucionada para 21 diferentes perfis de temperatura, pressão parcial e fração molar. Os resultados obtidos para o cenário com pressão parcial variável são mistos, o que pode indicar não haver a necessidade de considerar a variação da pressão parcial, desde que respeitada a fração molar, quando se trabalha com chamas em atmosfera aberta. Por outro lado, os resultados obtidos para o

cenário onde ocorre a variação da fração molar ao longo do meio mostram um incremento na acurácia do método WSGG e os resultados obtidos pelas duas correlações que lidam com intervalos menores de fração molar sugerem que não há necessidade de se utilizar uma única correlação que abrange todo o intervalo de fração molar, de 0.125 a 4.0.

Palavras-chave: Radiação térmica; Radiação em meios participantes; Soma-ponderada-de-gases-cinzas; Oxicombustão.

ABSTRACT

In this work, it is proposed an alternative way to obtain weighted-sum-of-gray-gas (WSGG) models. Despite the wide variety of WSGG models formulations available in the literature, applicable to different scenarios, none of them is concerned with the influence of the partial pressure of the participating species on the results given by the WSGG method when solving the radiative transfer equation (RTE). In addition, it is presented a new approach to obtain WSGG models for problems with varying mole ratios. Five different sets of WSGG correlations are provided, each one for its respective scenario. The first scenario deals with open-atmosphere combustions and considers a fixed mole ratio (MR) with varying partial pressure over the media. There are two different correlations for this scenario, one for a MR equals to one; and the other for a MR equals to two. In the second scenario, the correlations are designed to deal with a varying MR along the pressure-path-length, $p_a S$, a situation that is common in oxy-fuel combustions. The correlations are generated from total emittance fit to data obtained from the high-resolution spectral database HITEMP-2010. For the first scenario, absorption spectra are extracted from HITEMP-2010 for 9 different partial pressures and 23 temperatures, based on which emittance values are computed for 24 $p_a S$. For the second scenario, it is considered the same amount of temperature and $p_a S$; however, the change is not in the partial pressure, but in the molar ratio, for which are considered 17 different values. Furthermore, for another set of coefficients, the MR range is divided, yielding two new sets of total emittances. The Levenberg-Marquardt algorithm is employed to fit WSGG coefficients to these data. The performance of the resulting correlations is evaluated for one-dimensional radiative transfer calculations, using the solution provided by the line-by-line integration method as a benchmark. The radiative transfer equation is solved for 21 different profiles of temperature, partial pressure, and molar ratio. The results obtained for the varying partial pressure scenario are mixed, which may indicate that there is no need to account for the partial pressure when dealing with open-atmosphere combustion flames, inasmuch as the MR value is adequate. Conversely, the results obtained for the varying MR scenario show an increment on the exactness of the WSGG method; and the results obtained by the two correlations that deal with a narrow MR may indicate that splitting in two the WSGG correlations for mole ratios from 0.125 to 4.0 leads to more accuracy.

Keywords: Thermal radiation; Radiation in participating media; Weighted-sum-of-gray-gases; Oxy-fuel combustions.

CONTENTS

1	INTRODUCTION	1
1.1	Bibliography Review	2
1.2	Objectives	4
1.3	Dissertation Organization	5
2	RADIATION IN PARTICIPATING MEDIA	6
2.1	The Blackbody	6
2.2	Radiation Intensity	7
2.2.1	Intensity Attenuation Due to Absorption	8
2.2.2	Intensity Augmentation Due to Emission	10
2.3	The Radiative Transfer Equation	10
2.4	Total Emittance	11
2.5	Fundamentals of Radiation Absorption and Emission in Molecular Gases	11
2.5.1	Natural Broadening	12
2.5.2	Doppler Broadening	12
2.5.3	Stark Broadening	13
2.5.4	Collision Broadening	13
2.6	Spectroscopic Databases	14
2.7	The Absorption Coefficient	15
2.8	Methods for Spectral Integration of the RTE	15
2.8.1	LBL Integration	16
2.8.2	WSGG method	17
3	METHODOLOGY	20
3.1	Generating the Absorption Spectra	20
3.1.1	The Absorption Spectra for Partial Pressure Variations	21
3.1.2	The Absorption Spectra for Mole Ratio Variations	21
3.2	Obtaining the Total Emittance	22
3.3	Obtaining the WSGG Correlations	23
3.3.1	WSGG Correlations Accounting for Partial Pressure Variations	23
3.3.2	WSGG Correlations Accounting for Mole Ratio Variations	27

4	DESCRIPTION OF THE TEST CASES	32
4.1	Cases for Varying Partial Pressures	32
4.2	Cases for Varying Mole Ratio	36
4.3	Assessment of WSGG Correlations Deviations	40
5	RESULTS AND DISCUSSION	41
5.1	Results for Varying Partial Pressures	41
5.1.1	Results for Total Emittance	41
5.1.2	Results for the Radiative Heat Source and Heat Flux	45
5.2	Results for Varying MR	60
5.2.1	Results for the Total Emittance	60
5.2.2	Results for the Radiative Heat Source and Heat Flux	62
6	FINAL COMMENTS AND CONCLUSIONS	78
6.1	Possibilities for Future Work	80
	BIBLIOGRAPHIC REFERENCES	80
	APPENDIX A WSGG Coefficients for Other Configurations	84

LIST OF FIGURES

Figure 2.1	Blackbody surrounded by a hemispherical detector [adapted from Howell et al., 2015].	6
Figure 2.2	Spectral intensity emitted by a infinitesimal area dA [adapted from Incropera et al., 2007].	7
Figure 2.3	Spectral radiation intensity normal to an absorbing infinitesimal volume [adapted from Howell et al., 2015].	9
Figure 2.4	Spectral absorption coefficient for H_2O at 1400 K, and $p_a=0.2$ atm.	12
Figure 2.5	One-dimensional domain.	16
Figure 3.1	Differences in total emittances due to partial pressure variation at a pressure-path-length of 6 atm.m.	23
Figure 4.1	Temperature profiles for cases with varying partial pressure.	35
Figure 4.2	Molar concentration profiles for cases with varying partial pressure.	35
Figure 4.3	Temperature profiles for cases with a varying MR.	39
Figure 4.4	Molar concentration profiles for cases with a varying MR.	39
Figure 4.5	MR variations within the proposed profiles.	40
Figure 5.1	Comparison between emittances for MR= 1 and $p_a = 0.05$ atm.	41
Figure 5.2	Comparison between emittances for MR= 1 and $p_a = 0.2$ atm.	42
Figure 5.3	Comparison between emittances for MR= 1 and $p_a = 0.5$ atm.	42
Figure 5.4	Comparison between emittances for MR= 1 and $p_a = 1.0$ atm.	43
Figure 5.5	Comparison between emittances for MR= 2 and $p_a = 0.075$ atm.	43
Figure 5.6	Comparison between emittances for MR= 1 and $p_a = 0.3$ atm.	44
Figure 5.7	Comparison between emittances for MR= 2 and $p_a = 0.6$ atm.	44
Figure 5.8	Comparison between emittances for MR= 2 and $p_a = 1.0$ atm.	45
Figure 5.9	Comparison of results for the radiative heat source for Case p1.1.	46
Figure 5.10	Comparison of results for the radiative heat flux for Case p1.1.	46
Figure 5.11	Comparison of results for the radiative heat source for Case p1.2.	47
Figure 5.12	Comparison of results for the radiative heat flux for Case p1.2.	48
Figure 5.13	Comparison of results for the radiative heat source for Case p1.3.	48
Figure 5.14	Comparison of results for the radiative heat flux for Case p1.3.	49

Figure 5.15	Comparison of results for the radiative heat source for Case p1.4. . .	50
Figure 5.16	Comparison of results for the radiative heat flux for Case p1.4. . .	50
Figure 5.17	Comparison of results for the radiative heat source for Case p1.5. . .	51
Figure 5.18	Comparison of results for the radiative heat flux for Case p1.5. . .	52
Figure 5.19	Comparison of results for the radiative heat source for Case p2.1 . .	53
Figure 5.20	Comparison of results for the radiative heat flux for Case p2.1. . .	53
Figure 5.21	Comparison of results for the radiative heat source for Case p2.2. . .	54
Figure 5.22	Comparison of results for the radiative heat flux for Case p2.2. . .	55
Figure 5.23	Comparison of results for the radiative heat source for Case p2.3. . .	55
Figure 5.24	Comparison of results for the radiative heat flux for Case p2.3. . .	56
Figure 5.25	Comparison of results for the radiative heat source for Case p2.4. . .	57
Figure 5.26	Comparison of results for the radiative heat flux for Case p2.4. . .	57
Figure 5.27	Comparison of results for the radiative heat source for Case p2.5. . .	58
Figure 5.28	Comparison of results for the radiative heat flux for Case p2.5. . .	60
Figure 5.29	Comparison between emittances for MR= 0.5.	61
Figure 5.30	Comparison between emittances for MR= 1.	61
Figure 5.31	Comparison between emittances for MR= 2.	62
Figure 5.32	Comparison of results for the radiative heat source for Case m2.1. . .	63
Figure 5.33	Comparison of results for the radiative heat flux for Case m2.1. . .	64
Figure 5.34	Comparison of results for the radiative heat source for Case m2.2. . .	65
Figure 5.35	Comparison of results for the radiative heat flux for Case m2.2. . .	65
Figure 5.36	Comparison of results for the radiative heat source for Case m3.1. . .	66
Figure 5.37	Comparison of results for the radiative heat flux for Case m3.1. . .	67
Figure 5.38	Comparison of results for the radiative heat source for Case m3.2. . .	68
Figure 5.39	Comparison of results for the radiative heat flux for Case m3.2. . .	68
Figure 5.40	Comparison of results for the radiative heat source for Case m3.3. . .	69
Figure 5.41	Comparison of results for the radiative heat flux for Case m3.3. . .	70
Figure 5.42	Comparison of results for the radiative heat source for Case m3.4. . .	71
Figure 5.43	Comparison of results for the radiative heat flux for Case m3.4. . .	71
Figure 5.44	Comparison of results for the radiative heat source for Case m3.5. . .	72
Figure 5.45	Comparison of results for the radiative heat flux for Case m3.5. . .	73
Figure 5.46	Comparison of results for the radiative heat source for Case m4.1. . .	73

Figure 5.47	Comparison of results for the radiative heat flux for Case m4.1 . . .	74
Figure 5.48	Comparison of results for the radiative heat source for Case m4.2. . .	75
Figure 5.49	Comparison of results for the radiative heat flux for Case m4.2. . .	75

LIST OF TABLES

Table 1.1	Brief summary for the reviewed WSGG correlations.	4
Table 3.1	WSGG Correlations for a varying p_a , and MR= 1	27
Table 3.2	WSGG Correlations for a varying p_a , and MR= 2	27
Table 3.3	WSGG Correlations for a varying MR.	30
Table 3.4	WSGG Correlations for smaller MR range.	31
Table 4.1	Cases summary for partial pressure variations.	34
Table 4.2	Cases summary for MR variations.	38
Table 5.1	Deviations from LBL calculations for cases using correlations from Tables 3.1.	59
Table 5.2	Deviations from LBL calculations for cases using the correla- tions from Tables 3.3 and 3.4.	77
Table A.1	WSGG Correlations for a varying MR with $p_{H_2O} + p_{CO_2} = 1$	84

LIST OF ACRONYMS

CFD	Computational Fluid Dynamics
DOM	Discrete Ordinates Method
EWBM	Exponential Wide Band Model
FORTTRAN	Formula Translator
FSK	Full-Spectrum-k-distribution
HITEMP	High-Temperature Spectroscopic Absorption Parameters
HITRAN	High-Resolution Transmission Molecular Absorption Database
IEA	International Energy Agency
LBL	Line-by-Line
MR	Mole Ratio
PROMECC	Programa de Pós-Graduação em Engenharia Mecânica
PTES	Primary Total Energy Supply
RTE	Radiative Transfer Equation
SLW	Spectral-Line-Weighted-Sum-of-Gray-Gases
SNB	Spectral Narrow Band
UFRGS	Universidade Federal do Rio Grande do Sul
WSGG	Weighted-Sum-of-Gray-Gases

LIST OF SYMBOLS

Latim Symbols

$a_{i,j}$	Weighting factor component related to the i -th gray-gas and j -th temperature polynomial
A	Area, m ²
$b_{i,k}$	Weighting factor component related to the i -th gray-gas and k -th partial pressure polynomial or mole ratio
c_0	Light velocity in vacuum, m/s
$c_{i,j}$	Temperature polynomial coefficient of the WSGG weighting factor
C_1	First Planck's constant, W.μ m ⁴ /m ² .sr
C_2	Second Planck's constant, μ m.K
C_η	Absorption cross-section, cm ² /molecule
$d_{i,k}$	Partial pressure or mole ratio polynomial coefficient of the WSGG weighting factor
D	Atom diameter, m
E_b	Total emissive power of a blackbody, W/m ²
$E_{b,\eta}$	Spectral emissive power of a blackbody, W/μm.m ²
k_η	Spectral absorption coefficient, atm ⁻¹ .m ⁻¹
I	Radiation intensity, W/m ²
I_b	Total radiation intensity of a blackbody, W/m ²
$I_{b,\eta}$	Spectral radiation intensity of a blackbody, W/m ² μm
I_η	Spectral radiation intensity, W/m ² μm
I_i	Radiation intensity of the i – th gray-gas, W/μm.m ² .sr
M	Particle mass, kg
N	Molecular density, molecule/cm ² .m
N_a	Avogadro's number, mol-1
p	Total pressure, atm
p_a	Partial pressure of molecular species, atm
$p_{a_{ref}}$	Reference partial pressure, atm
$p_a S$	Pressure-path-length, atm.m
q''	Radiative heat flux, W/m ²

R_{ug}	Universal gas constant, $\text{J/mol}^{-1}.\text{K}^{-1}$
S	Length, m
S_i	Spectral-line intensity, $\text{cm}^{-1}/\text{molecule.cm}^{-2}$
T	Temperature, K
T_{ref}	Temperature of reference, K
w_i	Weighting factor related to the <i>i-th</i> gray-gas
w_0	Weighting factor related to the transparent window
X	Distance between the two parallel plates of the domain, m
Y	Molar concentration

Greek Symbols

δ	Deviation for the radiative heat source, %
η	wavenumber, cm^{-1}
γ	Band halfwidth, m
μ_l	Cosine of angle l
$\nabla q''$	Radiative heat source, W/m^3
ρ	Specific mass, kg/m^3
σ	Stefan-Boltzmann constant, $\text{W/m}^2\text{K}^4$
θ	Polar coordinate, rad
ε	Total emittance
ε_η	Spectral total emittance
φ	Azimuthal coordinate, rad
χ	Deviation for the radiative heat flux, %
ω	Solid angle, sr

1 INTRODUCTION

According to data obtained from the International Energy Agency (IEA) website, around 90% of the world's primary total energy supply (PTES) originates from sources that must pass through a combustion process to generate the desired type of energy, [IEA, 2020]. Such a scenario leads to the emission of tons of CO₂, a gas that contributes to the greenhouse effect. Finding a way to minimize the emission of such gases is of extreme importance in the actual scenario, and numerical simulation is a great help to reduce those emissions due to its concept of virtual testing before prototyping.

It is also widely known that radiation is the predominant heat transfer mechanism in combustion processes, due to the high temperatures generated by the burning of the fuel. During the combustion process, due to chemical reactions, some gases are formed. These gases alter the behavior of the radiative heat transfer within the medium. In other words, the gases participate actively in the radiative heat transfer. Thus the phenomenon is called radiative heat transfer within participating media. Two gases are the ones that most participate in radiative heat transfer, one of these gases is the aforementioned CO₂, and the other is water vapor, H₂O.

Regarding numerical simulations, computing radiative heat transfer in a participating medium is, in general, computationally costly. The abrupt change in temperature and concentration of species participating in the heat transfer poses problems of numerical convergence. Also, there are millions of spectral lines representing the radiative behavior of each participating gas according to each wavenumber. The most accurate method is the line-by-line integration (LBL), which calculates the radiative transfer equation (RTE) for each wavenumber of the spectrum. However, due to the number of required calculations, the LBL is very time demanding, which makes it not appropriate for engineering applications.

Over the last decades, to reduce the computational cost, as well as the complexity of radiative heat transfer in participating media, several models were developed. The simplest of these models is the gray gas model, which assumes a single value to represent the absorption coefficient. However, it has been shown by many authors (for example, Cassol et al., 2015, and Wang et al., 2014) that this utter simplicity can lead to unacceptable deviations when calculating the radiative heat transfer in participating media.

As a more accurate alternative, there is the weighted-sum-of-gray-gases (WSGG) model, introduced by Hottel, 1954; it latter received contributions from Sarofim, presented in Hottel and Sarofim, 1965. In the WSGG model, it is considered a set of gray-gases to represent the spectrum, each one having a specific absorption coefficient and a weighting function that varies accordingly with the temperature. Although it seems very simple, the WSGG model has been proved capable of providing relatively good results and can be computed with any method of spatial integration, [Modest, 1991].

There are many other models in the literature to solve the RTE within a participating media, such as the spectral-line-weighted-sum-of-gray-gases (SLW) and the full-spectrum- k -distribution (FSK) model. Each one of these methods has its particularities and accuracy. However, this work does not aim to discuss the differences among several models to solve the RTE but to study the characteristics and limitations of the WSGG method by investigating the changes in the results when varying different parameters. If one needs more information about the plethora of ways to solve the RTE, the books from Howell et al., 2015, and by Modest, 2013, are good points to start.

1.1 Bibliography Review

Hottel, 1954, introduced the WSGG method, which represents the multitude of the spectral lines with a relatively small number of gray gases, and a transparent window. Each of these grey-gases has a constant absorption coefficient that covers a given part of the spectrum and is independent of the medium temperature, and concentration of its species.

There are plenty of studies reporting different WSGG coefficients. The way the coefficients are obtained vary from study to study, producing different results in terms of accuracy. One of the most popular WSGG coefficients in use is those presented by Smith et al., 1982, which are embedded in some commercial CFD software. In that study, Smith et al., 1982, obtained coefficients for $p_{H_2O}/p_{CO_2} = 2$, and $p_{H_2O}/p_{CO_2} = 1$, by fitting emittance data obtained from the exponential wide band model (EWBM) [Edwards and Menard, 1964]. However, with the development of new spectral databases, such as the HITEMP-2010, [Rothman et al., 2010], new correlations that are more accurate than those proposed by Smith et al., 1982, were developed. Moreover, the model presented by Smith et al. uses only three gray gases, which has been shown to be more inaccurate than

when using four gray gases as pointed out by Dorigon et al., 2013, and Kangwanpongpan et al., 2012.

In recent years, were developed WSGG models considering different scenarios, each one with a distinct application in terms of media mole concentration, total pressure, and mole ratio (MR), to name a few. Johansson et al., 2011, obtained WSGG coefficients for a mixture of CO₂, and H₂O by fitting emittances calculated by using the spectral narrow-band (SNB) model within an MR range from 0.125 to 2, temperature from 500 to 2500 K, and a pressure-path-length between 0.01 and 60 bar.m. The authors presented a method to incorporate the changes in the MR of the mixture into the absorption coefficient and the blackbody emissivity fraction.

Kangwanpongpan et al., 2012, provided new coefficients with a broad range and better accuracy in comparison with the correlation presented by Johansson et al., 2011. It was obtained a series of emittances within an MR range from 0.125 to 4, and a temperature range of 400-2500 K using LBL integration, and the HITEMP-2010 database. These emittances were used for fitting a series of coefficients related to each MR separately. Then, the authors proposed two methods to correlate each of these coefficients and the variance of the MR within a medium, resulting in two distinct sets of correlations. It is worth mentioning that each set of correlations proposed by Kangwanpongpan et al., 2012, works separately.

Later, Bordbar et al., 2014 presented new correlations with a model very similar to that used by Kangwanpongpan et al., 2012. However, Bordbar et al., 2014, considered a vast range for the MR, from 0.01 to 4, and a temperature range of 500-2400 K. Bordbar et al., 2014, also tested the obtained correlations within a three-dimensional medium and achieved satisfactory results.

In a different scenario than those two previously mentioned, Dorigon et al., 2013, presented coefficients for open-atmosphere combustions of methane, and fuel-oil with partial pressure ratios of $p_{H_2O}/p_{CO_2} = 2$, MR equals to 2, and $p_{H_2O}/p_{CO_2} = 1$, MR equals to 1. In this study, Dorigon et al., 2013, obtained the coefficients by fitting emittances generated from the HITEMP-2010 database, [Rothman et al., 2010]. The emittances obtained were within the pressure-path-length from 0.0001 atm.m to 10 atm.m, and temperature range of 400-2500 K. The media profiles used by Dorigon et al., 2013, to test the coefficients considered an average mole concentration of CO₂, Y_{CO_2} , equal to 0.1. Note that

the mole concentration did vary, though.

Cassol et al., 2014, developed a method to use together coefficients initially obtained for individual species. It was presented correlations for CO₂, H₂O, and soot fitted from emittance obtained with the HITEMP-2010 database. Then, using the proposed method, the coefficients were combined according to the medium concentration. The results obtained were within a good range of deviations when compared in a 1D medium against the results obtained from the LBL integration.

Coelho and França, 2018, presented different WSGG correlations to be used at total pressures ranging from 1 atm to 40 atm at an MR equals to 2. It was considered a range of medium path-length from 0.01 m to 30 m, and temperatures varying from 400 K to 2500 K. The mole concentration was kept at 0.3.

Recently, Wang and Xuan, 2019, proposed a modification in the traditional WSGG method to account for the variation of the total pressure within a medium, obtaining results with smaller deviations when compared against the other two authors' correlations. Instead of generating different absorption coefficients, the authors proposed a single set of absorption coefficients, and modified the weighting function, so that it depends on the temperature and total pressure. The emittances were generated for a pressure-path-length from 0.0001 atm.m to 10 atm.m and temperature range of 500-2500 K.

As it can be inferred, there are a wide variety of WSGG correlations with different applications. However, none of them accounted for the importance of including the partial pressure, and the mole ratio in the weighting function. Table 1.1 shows a brief summary with some parameters of the reviewed WSGG correlations.

Table 1.1 – Brief summary for the reviewed WSGG correlations.

Reference	Mole ratio	Temperature range	Number of gray-gases	Total pressure
Smith et al. [1982]	1 and 2	600-2400 K	3	1.0 atm
Johansson et al. [2011]	0.125-2.0	500-2500 K	4	1.0 bar
Kangwanpongpan et al. [2012]	0.125-4.0	400-2500 K	4	1.0 bar
Bordbar et al. [2014]	0.01-4.0	500-2400 K	4	1.0 bar
Dorigon et al. [2013]	1 and 2	400-2500 K	4	1.0 atm
Coelho and França [2018]	2	400-2500 K	4	1.0, 2.0, 5.0, 10, 20, and 40 atm
Wang and Xuan [2019]	1	500-2500 K	5	1.0, 2.0, 5.0, 10, 15, 20, 25, and 30 atm

1.2 Objectives

Using the approach proposed by Wang and Xuan, 2019, this work aims to compare the importance of the partial pressure and the mole ratio at the final results obtained from

simulations on an one-dimensional domain.

To do so, WSGG correlations that account for the changes in the local partial pressure are developed and compared with the WSGG correlations provided by Dorigon et al., 2013. Later, using the same methodology, it is developed and compared WSGG correlations that account for the mole ratio variation along a path-length against the other two WSGG models, from Kangwanpongpan et al., 2012, and Bordbar et al., 2014.

1.3 Dissertation Organization

This work is divided into six Chapters. The first Chapter presents the importance of problems involving radiation in participating media along with a review of the literature concerning this matter.

The second Chapter, Radiation in Participating Media, establishes the foundations to solve problems involving thermal radiation in gases.

Next, the third Chapter, Methodology, explains how data from HITEMP-2010 is used to generate the absorption coefficients, the total emittance, and finally how this work fits this data to obtain the WSGG correlations.

The fourth Chapter, Description of the Test Cases, describes each temperature profile and medium mole concentration, using equations to model and graphs to illustrate each case.

The obtained results are exposed in Chapter 5, Results and Discussion, which presents the results that are obtained for the two proposed scenarios of this work.

Finally, Chapter 6, Final Comments And Conclusions, draws the possible inferences obtained throughout this work and poses a few topics for further research.

2 RADIATION IN PARTICIPATING MEDIA

Radiation is the only mean of energy transfer that happens through a vacuum medium [Incropera et al., 2007]. According to Howell et al., 2015, this occurs because the radiation propagates as an electromagnetic wave along a given path. The radiative spectrum comprises an infinitude of wavelengths; however, as a subject of this study, only the thermal portion of the spectrum will be considered. The thermal parcel, in other words, the thermal radiation, occurs from a wavelength range of 0.1-100 μm and encompasses the ultraviolet, the visible light, and the infrared spectra.

2.1 The Blackbody

The blackbody is a crucial concept to the study of radiation. It is idealized as a body capable of emitting all of its energy uniformly in all directions and wavelengths, [Howell et al., 2015]. Also, the blackbody is capable of absorbing all the incident radiation on its surface.

Consider a blackbody with a temperature T surrounded by a sensor that covers the whole hemisphere, as in Figure 2.1.

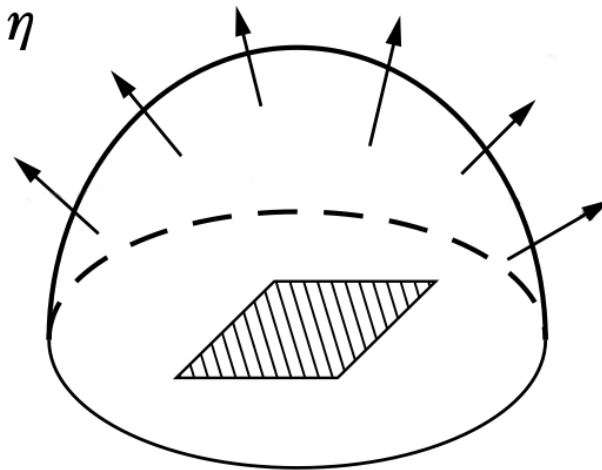


Figure 2.1 – Blackbody surrounded by a hemispherical detector [adapted from Howell et al., 2015].

The blackbody hemispherical spectral emissive power, $E_{b,\eta} (W/m^2 \mu m)$, for a given wavenumber $\eta (cm^{-1})$, and temperature $T(K)$ is given by Planck's spectral distribution, [Howell et al., 2015]:

$$E_{b,\eta}(\eta, T) = \frac{2C_1\pi\eta^3}{e^{C_2\eta/T} - 1} \quad (2.1)$$

where C_1 and C_2 are the first, and second Planck's constants, which are equivalent to $0.59552137 \times 10^8 W.\mu m^4/m^2.sr$, and $1.4387752 \times \mu m^4$, respectively.

Equation (2.1) can be integrated over the whole spectrum leading to the Stefan-Boltzmann law, which is the blackbody total emissive power, $E_b(W/m^2)$:

$$E_b = \sigma T^4 \quad (2.2)$$

in which σ is the Stefan-Boltzmann constant, that equals to $5.6704 \times 10^{-8} W/m^2 K^4$.

2.2 Radiation Intensity

Consider the radiation emitted by an infinitesimal area dA , in a direction described by the angles $d\theta$, and $d\varphi$, depicted in Figure 2.2. Imagine an observer looking from the infinitesimal area dA to the projected area dA_n , which is normal to the emitted radiation. If this observer can see the radiation through its whole path, then the observer is able to see what is called the solid angle $d\omega$, which is the conical area that comprises the propagation of the radiation from its origin to its destiny.

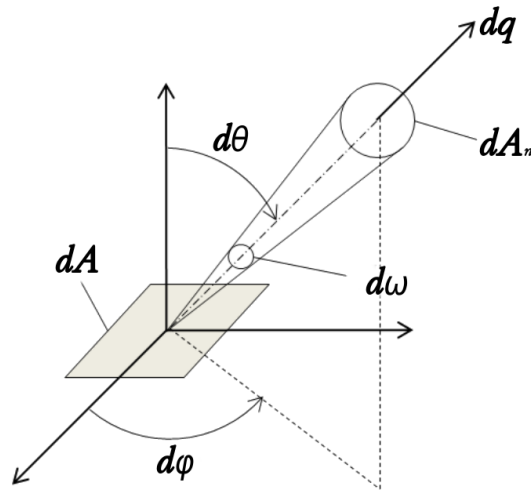


Figure 2.2 – Spectral intensity emitted by a infinitesimal area dA [adapted from Incropera et al., 2007].

The spectral radiation intensity is then defined as the rate of which radiation is

emitted by an area dA for a given η wavenumber, per projected area dA_n , per solid angle $d\omega$ around ω , per an infinitesimal wavenumber interval $d\eta$ around η , [Howell et al., 2015]:

$$I_\eta(\eta, \theta, \varphi) = \frac{dq}{dA \cos \theta d\omega d\eta} \quad (2.3)$$

in which $I_\eta(\eta, \theta, \varphi)$ is given in $W/m^2 \cdot \mu m \cdot sr$, $dA \cos \theta$ is the projected area dA_n , and the solid angle $d\omega$ is defined by $\sin \theta d\theta d\varphi$. For the sake of simplicity, $I_\eta(\eta, \theta, \varphi)$ shall be denoted only as I_η from now on.

The blackbody is supposed to emit energy equally in all directions, thus for a blackbody I_η can be denoted as $I_{b,\eta}(\eta, T)$, meaning that the radiation intensity for a blackbody depends only on the wavenumber, and temperature. From the literature, [Howell et al., 2015], the blackbody radiation intensity is given by the Planck's spectral distribution as:

$$I_{b,\eta}(\eta, T) = \frac{E_{b,\eta}}{\pi} = \frac{2C_1\eta^3}{e^{C_2\eta/T} - 1} \quad (2.4)$$

given in $W/m^2 \cdot \mu m \cdot sr$.

Equation (2.4) is valid only when the medium along the path of radiation does not interfere in the variation of energy intensity. When the medium interferes in the way that energy travels along the path, it is named radiation in participating media, which is going to be covered next.

2.2.1 Intensity Attenuation Due to Absorption

The vast majority of radiative energy exchange that occurs on Earth happens through participating media. When the media interferes in the radiation, some considerations must be done before ensuring proper calculations of the energy transfer. The attenuation within a medium can happen due to absorption and scattering. In this work, only the attenuation due absorption is regarded, for the scattering in methane and fuel-oil combustion is not as significant as in other fuel combustion such as coal.

Consider a spectral radiation intensity I_η incident normally to an infinitesimal volume, show on Figure 2.3.

As the incident radiation passes through the infinitesimal volume, it is dimmed due to the absorption of the medium. As pointed by Modest, 2013, this change in intensity

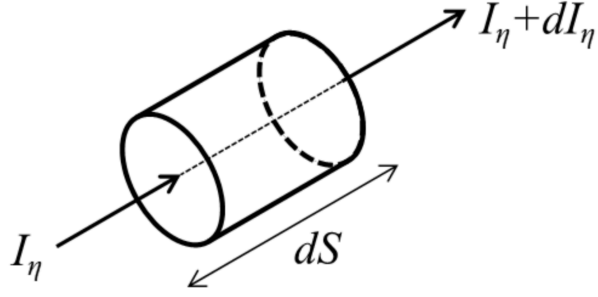


Figure 2.3 – Spectral radiation intensity normal to an absorbing infinitesimal volume
[adapted from Howell et al., 2015].

is in proportion with the magnitude of the local intensity and the path-length traveled by the radiation. For a non-scattering medium, the reduction in the intensity can be described by:

$$dI_\eta(S) = -k_\eta(S)I_\eta(S)dS \quad (2.5)$$

where $k_\eta(S)$ is the medium absorption coefficient at any given position S , and dS is the path-length. It is very important to point out that the equations henceforth are presented as a function of a position S , meaning that at each position the medium may depend on either or both different temperatures and species concentration, which directly contributes to changes in the radiative behavior.

One clear example is that, as pointed by Modest, 2013, the absorption coefficient $k_\eta(S)$ in molecular gases is strongly dependent on the number of receptive molecules per unit volume. Therefore, if the molar concentration of a gas varies along the path-length, so does the absorption coefficient $k_\eta(S)$. Contrariwise, in some radiation models, the absorption coefficient is assumed to be independent of the path-length.

Because of the absorption coefficient dependence on the amount of receptive molecule per unit volume, it can be presented as $k_{p,\eta} = k_\eta/p_a$ or $k_{\rho,\eta} = k_\eta/\rho$, where p and ρ are used to denote the dependence on the partial pressure or specific mass of the participating species. It is noteworthy to point out that in this work, $k_{\rho,\eta}$ is not regarded.

2.2.2 Intensity Augmentation Due to Emission

Like the intensity attenuation due to absorption, the change in intensity due to emission must also be proportional to the distance traveled by the radiation and the local intensity of the medium, [Modest, 2013]. Thus, the augmentation in the spectral radiation intensity can be written, as:

$$dI_\eta(S) = f_\eta(S)dS \quad (2.6)$$

in which $f_\eta(S)$ is the emission coefficient, defined as $k_\eta(S)I_{b,\eta}(S)$ for media that are in a local thermodynamic equilibrium (LTE), [Modest, 2013]. Thus Equation (2.6) becomes:

$$dI_\eta(S) = k_\eta(S)I_{b,\eta}(S)dS \quad (2.7)$$

2.3 The Radiative Transfer Equation

The radiative transfer equation (RTE) is the equation that governs radiative heat transfer in participating media. It arises from an energy balance on the infinitesimal volume of Figure 2.3, accounting for both the attenuation and augmentation of the radiation intensity as it crosses a path-length. Thus, for a participating and non-scattering medium, this equation can be written, as [Howell et al., 2015; Modest, 2013]:

$$\frac{dI_\eta(S)}{dS} = -k_\eta(S)I_\eta(S) + k_\eta(S)I_{b,\eta}(S) = k_\eta(S) [I_{b,\eta}(S) - I_\eta(S)] \quad (2.8)$$

in which $I_{b,\eta}(S)$, and $I_\eta(S)$ are the blackbody spectral intensity and the spectral intensity at position S on any given path. To obtain the total radiative heat transfer, the RTE must be integrated on the whole spectrum and in all spacial directions θ , and φ , which can be time demanding. Further, it will be presented two ways for solving the RTE, although there are other methods of solution. The reason for presenting only two methods lies in the main focus of this work, which is the WSGG method, and the plethora of other works that show an elegant framework in showing other methods, [Brittes, 2015; Howell et al., 2015; Mazurek, 2019; Modest, 2013], to name a few.

2.4 Total Emittance

The total emittance is a fraction of the energy emitted by a medium over the energy that is emitted by a blackbody, so that, [Howell et al., 2015]:

$$\varepsilon(T) = \frac{\int_{\eta=0}^{\infty} I_{b,\eta}(\eta, T) \varepsilon_{\eta}(T) d\eta}{\int_{\eta=0}^{\infty} I_{b,\eta}(\eta, T)} \quad (2.9)$$

in which $\varepsilon_{\eta}(T)$ is the spectral emittance.

Kirchhoff's Law states that the spectral emittance ε_{η} is equal to the spectral absorptance α_{η} , which is defined by, [Howell et al., 2015]:

$$\alpha_{\eta} = 1 - e^{(-k_{p,\eta} p_a S)} \quad (2.10)$$

Substituting Equations (2.2), (2.4), and (2.10) into Equation (2.9), gives:

$$\varepsilon(T, p_a S) = \frac{\int_{\eta=0}^{\infty} I_{b,\eta}(\eta, T) [1 - \exp(-k_{p,\eta} p_a S)] d\eta}{\sigma T^4 / \pi} \quad (2.11)$$

in which $p_a S$ is the pressure path-length of the medium.

2.5 Fundamentals of Radiation Absorption and Emission in Molecular Gases

The spectral behavior of molecular gases has a great complexity when compared with solid surfaces, for the radiative properties of a molecular gas can spike up and down with small changes in the wavenumber, as shown in Figure 2.4. This way, the determination of radiative properties for molecular gases relies on some quantum mechanical laws, [Howell et al., 2015].

A photon must be captured or liberated within a given frequency for absorbing or emitting energy. Theoretically, there is a certain amount of energy that must be reached to the absorption or emission of a photon to happen. If photons were absorbed or emitted only at those specific levels, a graph with vertical bars representing any spectral properties, such as the absorption coefficient, at each wavenumber would be the consequence. However, some phenomena interfere in the absorption or emission of a photon, and these phenomena cause the spectral lines to have a broadened shape, thus are called broadening effects.

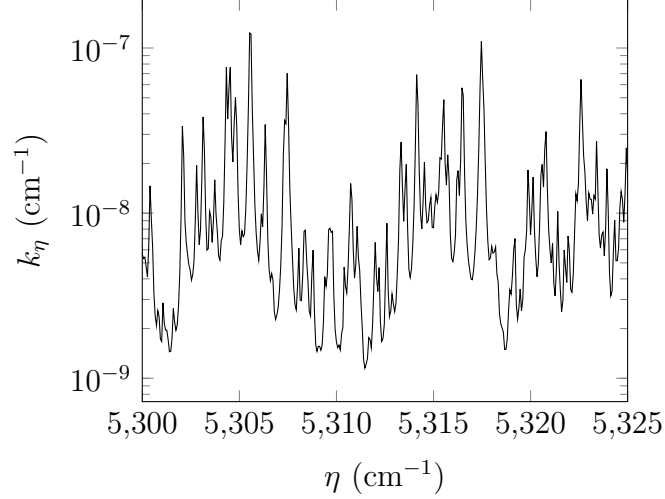


Figure 2.4 – Spectral absorption coefficient for H₂O at 1400 K, and $p_a=0.2$ atm.

2.5.1 Natural Broadening

The Heisenberg uncertainty principle establishes that the energy of an electron in a certain atomic level can not be determined exactly. This uncertainty in the atomic levels is then the cause of the natural broadening, [Bhatia, 2001]. Dirac's relativistic quantum theory can describe the shape of the lines that are originated by the natural broadening phenomenon. However, these lines can also be obtained by the Schrödinger's non-relativistic quantum theory according to the Lorentz profile, [Howell et al., 2015]:

$$\frac{C_{\eta,i,j}(\eta)}{S_{i,j}} = \frac{\gamma_N/\pi}{\gamma_N^2 + (\eta - \eta_{i,j})^2} \quad (2.12)$$

where $C_{\eta,i,j}$ is the absorption cross-section, in $cm^2/molecule$, γ_N is the line half-width at half-maximum for the natural broadening, and $S_{i,j}$ is the line intensity.

2.5.2 Doppler Broadening

The Doppler broadening is a result of aleatory molecule movement of the species, which leads to a change in the wavelength. If the molecule is in the direction of the observer, the wavelength will appear shorter. This effect can be described by [Howell et al., 2015]:

$$\frac{C_{\eta,i,j}(\eta)}{S_{i,j}} = \frac{1}{\gamma_D} \sqrt{\frac{\ln 2}{\pi}} e^{\left[-(\eta - \eta_{i,j})^2 \frac{\ln 2}{\gamma_D^2}\right]} \quad (2.13)$$

in which γ_D is the line half-width at half-maximum for the Doppler broadening, i.e. Voigt profile, given by:

$$\gamma_D = \frac{\eta_{i,j}}{c_0} \left(\frac{2k_B T}{M} \ln 2 \right)^{\frac{1}{2}} \quad (2.14)$$

where c_0 is vacuum light velocity, k_B is the Boltzmann constant, and M the particles mass, in kg .

Note that the higher the temperature, the higher the Doppler broadening line half-width. Numerically speaking, the Doppler broadening is only significant above temperatures of 2500 K, [Wang and Modest, 2004].

2.5.3 Stark Broadening

This type of spectral line broadening happens when the disturbing particles are charged electrically, i.e., there are free ions and electrons. The Stark broadening gives to the spectral line a Lorentz profile followed by an oscillation in the wavelength, [Bhatia, 2001]. It is important to mention that the Stark broadening is not relevant in this study and most engineering problems, [Howell et al., 2015].

2.5.4 Collision Broadening

In engineering applications, the Collision broadening is the most relevant spectral line broadening phenomenon. It happens when a collision between two or more particles, atoms or molecules, disturbs the energy level within a particle. The higher the pressure, the higher the spectral line broadening due to the Collision broadening, [Modest, 2013].

The shape of the spectral lines is also given by the Lorentz profile, as in:

$$\frac{C_{\eta,i,j}(\eta)}{S_{i,j}} = \frac{\gamma_C/\pi}{\gamma_C^2 + (\eta - \eta_{i,j})^2} \quad (2.15)$$

where γ_C is the line half-width at half-maximum for the Collision broadening, given by, [Howell et al., 2015]:

$$\gamma_C = \frac{1}{2\pi c_0} \frac{4\sqrt{\pi} D^2 p_a}{(M k_b T)^{\frac{1}{2}}} \quad (2.16)$$

in which D is the atom, or molecule, diameter.

It is noteworthy to say that the line half-width is directly proportional to the

pressure and inversely proportional to the $T^{1/2}$, which suggests that this effect is especially important when the temperature is not too high, and the pressure is relevant. The work from Wang and Modest, 2004, concluded that the Lorentz profile returns good results for temperatures up to 2500 K, and pressures of at least 1 atm.

In this work, the maximum temperature is of 2500 K, and the total pressure is kept at 1 atm, which indicates that adopting the Lorentz profile for the collision broadening is the best choice.

2.6 Spectroscopic Databases

Spectroscopic databases are a compilation of experimental results for parameters relevant to spectral radiation, such as the energy difference between the initial and final state ν_i , given as a vacuum wavenumber, the energy of the lower state E_i , the line self-broadening $\gamma_{self,i}$, the broadening caused by air $\gamma_{air,i}$, and the temperature dependence coefficient n_c . All of the aforementioned parameters are functions of a given wavenumber. Thus, they can be readily used to obtain the desired spectral feature.

There is a considerable number of spectral databases differing in parameters such as the reference temperature, number of spectral lines per species, and species in the catalog. This work uses the HITEMP-2010 database, [Rothman et al., 2010], which derives from HITRAN, [Rothman et al., 1995]. The HITEMP-2010 contains 114241164 spectral lines for H₂O, and 11193608 spectral lines for CO₂. There are data for three more species, namely CO, OH, and NO; however, in this study, they are not considered.

The line intensity can be calculated from the following equation, [Rothman et al., 2010]:

$$S_i(T) = S_i(T_{ref}) \frac{Q(T_{ref})}{Q(T)} \frac{e^{(-C_2 E_i T)}}{e^{(-C_2 E_i T_{ref})}} \frac{[1 - e^{(-C_2 \nu_i T)}]}{[1 - e^{(-C_2 \nu_i T_{ref})}]} \quad (2.17)$$

where the temperature T_{ref} is kept at 296 K, and the total internal partition sums Q depends on molecule characteristics and is the sum of all energy states, such as vibrational, and rotational. Note that from all the quantities presented at Equation (2.17), only Q is obtained through a FORTRAN routine, [Fischer et al., 2003], provided within the database. The other parameters are readily available to be read from the database.

The next important parameter to be determined is the line half-width at half-

maximum, namely γ_C for this work and called γ_i henceforth. γ_i can be determined using the following equation:

$$\gamma_i(p, T) = \left(\frac{T_{ref}}{T}\right)^{n_c} [\gamma_{air,i}(p_{ref}, T_{ref})(p - p_a) + \gamma_{self,i}(p_{ref}, T_{ref})p_a] \quad (2.18)$$

in which the pressure p_{ref} is at 1 atm.

As mentioned before, the line broadening profile that is used on this work is the Lorentz profile, which gives the following equation for obtaining the spectral cross-section C_η , [Howell et al., 2015]:

$$C_\eta = \sum_{i=\eta-\Delta\eta}^{i=\eta+\Delta\eta} \frac{S_i(T)}{\pi} \frac{\gamma_i}{\gamma_i^2 + (\eta - \eta_i)^2} \quad (2.19)$$

where $\Delta\eta(cm^{-1})$ is the spectral span around η .

2.7 The Absorption Coefficient

After determining which spectral broadening effect is the most accurate for the problem under investigation and obtaining the parameters described within the very last section, the absorption coefficient can be readily obtained by [Howell et al., 2015]:

$$k_\eta(\eta, T, p, Y) = N(T, p)Y C_\eta(\eta, T, p, Y) \quad (2.20)$$

in which Y is the molar fraction of the species, and N is the molecular density given in *molecule/cm²m*, that is expressed by:

$$N(p, T) = \frac{pN_a}{R_{ug}T} \quad (2.21)$$

where N_a is the Avogadro's number, and R_{ug} is the universal gas constant.

2.8 Methods for Spectral Integration of the RTE

As stated before, there are several ways to solve the RTE. This work will briefly discuss the LBL integration, used as a benchmark, and the WSGG method, for which are proposed two distinct solutions.

2.8.1 LBL Integration

The LBL integration is usually regarded as a benchmark solution due to the accuracy obtained when a discretization on the wavenumber is performed until a well-established convergence criterion. The high accuracy is achieved because the LBL method will solve the RTE for each absorption coefficient related to its respective wavenumber; therefore, the higher the discretization, the higher the accuracy in the obtained results. However, it is important to stress out that the solutions presented by the LBL method are not exact, for the databases from which the spectral properties are computed, are obtained through experimental methods, which gather some errors throughout the obtention process itself.

Considering the domain represented in Figure 2.5, Equation (2.8) can be divided into two equations according to the Discrete Ordinates Method (DOM), [Chandrasekhar, 1960], as following:

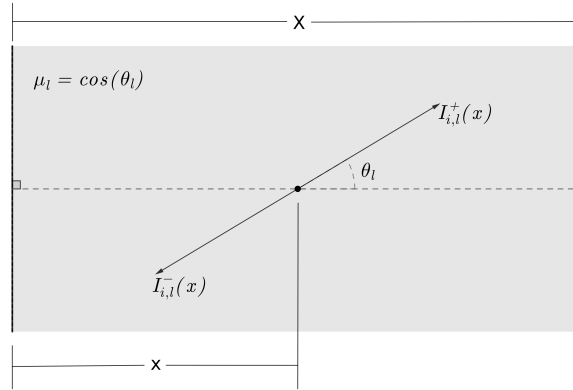


Figure 2.5 – One-dimensional domain.

$$\mu_l \frac{\partial I_{\eta,l}^+(x)}{\partial x} = -k_\eta(x) I_{\eta,l}^+(x) + k_\eta(x) I_{\eta,b}(x) \quad (2.22a)$$

$$-\mu_l \frac{\partial I_{\eta,l}^-(x)}{\partial x} = -k_\eta(x) I_{\eta,l}^-(x) + k_\eta(x) I_{\eta,b}(x) \quad (2.22b)$$

in which μ_l is the cosine of the angle θ_l and $I_{\eta,l}^+$, and $I_{\eta,l}^-$ are the radiation intensity for $\mu_l > 0$, and $\mu_l < 0$.

Equation (2.22) is a set of first order linear differential equations dependant on $I_{\eta,l}(x)$, thus requiring one boundary condition, a known value for $I_{\eta,l}(x)$, for each equation. Considering that the walls of the domain depicted on Figure 2.5 behave like a blackbody,

the boundary conditions for solving Equations (2.22a), and (2.22b) are:

$$I_{\eta,l}^+(x=0) = I_{\eta,b}(x=0) \quad (2.23a)$$

$$I_{\eta,l}^-(x=X) = I_{\eta,b}(x=X) \quad (2.23b)$$

After solving the RTE using Equations (2.22a), and (2.22b), the radiative heat flux, and the radiative heat source can be obtained by:

$$q''(x) = \sum_{l=1}^L \int_{\eta=0}^{\infty} \{2\pi\mu_l g_l [I_{\eta,l}^+(x) - I_{\eta,l}^-(x)]\} d\eta \quad (2.24)$$

$$-\nabla q''(x) = \sum_{l=1}^L \int_{\eta=0}^{\infty} \{2\pi g_l k_{\eta} [I_{\eta,l}^+(x) + I_{\eta,l}^-(x)] - 4\pi k_{\eta} I_{\eta,b}(x)\} d\eta \quad (2.25)$$

where g_l is the quadrature weight in the l direction.

2.8.2 WSGG method

Instead of integrating the RTE for each wavenumber, the WSGG model assumes a certain quantity of i gray-gases that represent the whole spectrum. Each of these gray-gases will assume a portion of the total radiation intensity in a given direction. The relationship between the total radiation intensity and each gray gas is ruled by:

$$I(S) = \sum_{i=1}^I I_i(S) \quad (2.26)$$

in which I_i is the partial intensity corresponding to an i gray gas, given in W/m^2 . Applying the WSGG model to Equation (2.8) gives:

$$\frac{dI_i(S)}{dS} = -k_{p,i} p_a(S) I_i(S) + k_{p,i} p_a(S) w_i(S) I_b(S) \quad (2.27)$$

where $p_a(S)$ is the partial pressure of the species, $k_{p,i}$ is the pressure absorption coefficient, and $w_i(S)$ is the weighting function corresponding to the blackbody fraction. The weighting function w_i is better described on the following section.

Note that, although the WSGG model usually imposes the pressure absorption coefficient $k_{p,i}$ to be constant, the other variables, $p_a(S)$, $w_i(S)$ and $I_b(S)$, are computed locally, which makes the WSGG model suitable to media that are nonhomogeneous, and non-isothermal.

This work takes advantage, again, of the DOM to integrate Equation (2.27) across the spatial domain. In this study, to compute the RTE, thirty l directions are used. Figure 2.5 illustrates the assumptions made by the DOM, as well as the domain considered, which is the same as that considered to solve the RTE using the LBL integration. Thus, Equation (2.27) becomes:

$$\mu_l \frac{dI_{i,l}^+(x)}{dx} = -k_{p,i}p_a(x)I_{i,l}^+(x) + k_{p,i}p_a(x)w_i(x)I_b(x) \quad (2.28a)$$

$$\mu_l \frac{dI_{i,l}^-(x)}{dx} = -k_{p,i}p_a(x)I_{i,l}^-(x) + k_{p,i}p_a(x)w_i(x)I_b(x) \quad (2.28b)$$

As stated before, the walls are considered black, thus the boundary conditions for the problem at $x = 0$ and $x = X$ are $I_{i,l,x=0}^+ = w_i(T_{x=0})I_{b,x=0}$ and $I_{i,l,x=X}^- = w_i(T_{x=X})I_{b,x=X}$.

Like in the LBL integration, after solving Equations (2.28a), and (2.28b), it is possible to calculate the radiative heat flux and radiative heat source, [Howell et al., 2015]:

$$q''(x) = \sum_{l=1}^L \sum_{i=0}^I \{2\pi\mu_l g_l [I_{i,l}^+(x) - I_{i,l}^-(x)]\} \quad (2.29)$$

$$-\nabla q''(x) = \sum_{l=1}^L \sum_{i=1}^I \{2\pi g_l k_{p,i} p_a(x) \{ [I_{i,l}^+(x) + I_{i,l}^-(x)] - 2w_i(x)I_b(x) \}\} \quad (2.30)$$

Note that the radiative heat source equals $-\nabla q''(x)$, which means that the energy balance is assured. Also, it is important to point out that the transparent window, $i = 0$, is only considered when obtaining the radiative heat flux.

2.8.2.1 Total Emittance for the WSGG Method

To obtain the total emittance in the traditional WSGG method, Equation (2.11) is rewritten according to the assumptions made by the WSGG method, [Dorigon et al., 2013]:

$$\varepsilon(T, p_a S) = \sum_{i=1}^I w_i(T) [1 - \exp(-k_{p,i} p_a S)] \quad (2.31)$$

where $p_a S$ is the pressure-path-length, and the weighting function w_i is traditionally given by:

$$w_i(T) = \sum_{j=0}^J a_{i,j}(T)^j \quad (2.32)$$

in which $a_{i,j}(T)$ are the polynomial coefficients corresponding to each gray gas i , and j -th order polynomial obtained after a multiple linear regression. Further, it will be presented the assumptions made by this work regarding the weighting function. To guarantee that the radiative energy is conserved, the model has a transparent window representing the spaces between the high absorption regions, [Smith et al., 1982]. The transparent window is given by:

$$a_0(T) = 1 - \sum_{i=1}^I a_i(T) \quad (2.33)$$

3 METHODOLOGY

There were two distinct problems studied by this work. One was concerned with the effect of partial pressure, p_a , variations in the results obtained when solving the RTE. The second took into account the effects of different mole ratios (MR) along the path-length, which is a typical situation in oxy-fuel combustions.

Independently of the case for which the coefficients are going to be obtained, the first step when it comes to acquiring WSGG coefficients is to generate spectral lines, namely the absorption cross-section, and check its convergence. The second step is to obtain the total emittances for the desired mixtures of species for any given case. Then, a curve fitting is performed using the software SPSS 18, [IBM, 2020], which uses the Levenberg-Marquardt method [Marquardt, 1963], an algorithm to attribute coefficients for the informed equation. These coefficients are then related to polynomial coefficients dependant on the temperature, for the traditional WSGG method, or dependant on the temperature and p_a or MR for the WSGG method presented by this study. The final result forms a WSGG correlation, which is going to be used to calculate the radiative heat flux and radiative heat source over a given domain. Then, the results are compared with a benchmark solution performed against the LBL method. A detailed description of the utilized methodology is presented in the following sections.

3.1 Generating the Absorption Spectra

As mentioned before, the first step to generate any WSGG correlation is the obtention of spectral lines. The spectral lines were acquired for some species and a given range of wavenumber, temperature, pressure, and molar concentration. Using a FORTRAN routine, the parameters necessary to resolve, in this given order, Equations (2.17), (2.18), and (2.19), were read from the HITEMP-2010 database and solved using the same computational routine. Firstly, the absorption cross-section was obtained until numerical convergence for each species individually, and they were mixed using another FORTRAN routine when necessary.

Regarding the convergence for obtaining the absorption cross-section of each species, this work uses the criteria presented by Ziemniczak, 2014 to limit the extent of the calculations. Ziemniczak, 2014 affirms that a spectral span, $\Delta\eta$, of 400 cm^{-1} for CO_2 , and

40 cm^{-1} for H_2O is adequate. The aforementioned study also states that the number of points, i.e., the number of wavenumbers that suffices a good convergence criterion is equal to 150.000.

In this work, the wavenumber varied from 0 to 10000 cm^{-1} for both CO_2 and H_2O , which encompasses the thermal portion of the spectrum. The selected temperature range was from 300 K to 2500 K with steps of 100 K, which resulted in 23 different temperatures for each species. The molar concentration is better presented alongside its respective case, due to its high dependence on the case that is being studied, which are either p_a variations, or MR.

3.1.1 The Absorption Spectra for Partial Pressure Variations

There are two different scenarios regarding variations on the p_a . The first considers a MR between H_2O and CO_2 , of $p_{\text{H}_2\text{O}}/p_{\text{CO}_2} = 1$. The second considers $p_{\text{H}_2\text{O}}/p_{\text{CO}_2} = 2$. These are the stoichiometric ratios for methane, and fuel oil combustions, respectively.

With respect to $p_{\text{H}_2\text{O}}/p_{\text{CO}_2} = 1$, the selected molar concentrations when obtaining the absorption cross-sections were 0.025, 0.05, 0.1, 0.15, 0.2, 0.25, 0.3, 0.4, and 0.5 for CO_2 , and $Y_{\text{H}_2\text{O}} = Y_{\text{CO}_2}$. On the other hand, when $p_{\text{H}_2\text{O}}/p_{\text{CO}_2} = 2$, the selected molar concentrations were 0.0125, 0.025, 0.05, 0.1, 0.125, 0.15, 0.2, 0.25, and 0.333 for CO_2 , and $Y_{\text{H}_2\text{O}} = 2 \times Y_{\text{CO}_2}$.

The choice for using nine different mole concentrations followed after comparisons against coefficients generated using only five different molar concentrations. Although it takes longer to generate coefficients with a higher number of mole concentrations, the computational cost to solve the RTE is the same if the number of gray-gases and polynomial coefficients are not changed. It is noteworthy to mention that the improvements were small; however, since the coefficients were already available and considering the same computational cost, the choice for using the correlations that used nine different molar concentrations seemed appropriate.

3.1.2 The Absorption Spectra for Mole Ratio Variations

Concerning the mole ratio variations, there were also two studied scenarios. However, only one of these scenarios is reported in this study. The reason for that, as will be seen, is that the p_a does not contribute to a significant difference in the results for

the radiative heat source and radiative heat flux. Thus, keeping a value that is within the minimum and maximum range will generate results that are more widely applicable. Oxy-fuel combustion tends to have partial pressures closer to $p_a = 1$ atm, and open-atmosphere combustion of methane to $p_a = 0.3$ atm. Note that these observations were made after studying the varying partial pressure scenario, thoroughly.

Both scenarios considered an MR range of 0.125-4, with steps of 0.25 except the first one, which was a step of only 0.125. The first scenario, which is the one presented, considered a fixed CO_2 concentration equals to 0.2, which implied values in the range of 0.025-0.8 for H_2O concentrations. As this study proceeds, the selection of these molar concentrations will be better understood.

The second scenario considers the same MR range; however, it also considers $Y_{\text{CO}_2} + Y_{\text{H}_2\text{O}} = 1$. The generated coefficients for the second scenario can be consulted in Appendix A if one finds it relevant for its study.

3.2 Obtaining the Total Emittance

The total emittance can be obtained using Equation (2.11). Note that in Equation (2.11), the total emittance is a function of the pressure-path-length, $p_a S$, and the pressure absorption coefficient $k_{p,\eta}$. The pressure absorption coefficient is a function of the temperature, mole concentration, pressure, and wavenumber and can be calculated with Equation (2.20) after the determination of its respective absorption cross-section.

It is noteworthy to point out, that the total emittance was calculated for several mixtures of the two studied species, i.e., the total emittance was obtained after a combination of the absorption cross-section of the two species using a FORTRAN routine.

Because the total emittance is a function of the $p_a S$, the emittances are calculated according to many fixed $p_a S$ values. It is important to stress out that having the same $p_a S$, and the same temperature does not imply identical values for the total emittance under different partial pressures, as shown in Figure 3.1. For this reason, Coelho and França, 2018, decided to plot their results for total emittance as a function of the product between the path-length and the medium concentration, YS . The cause of this variation in the total emittances for the same pressure-path-length is because the broadening effect for the Lorentz profile takes into consideration the value of the partial pressure, as shown in Equation (2.18).

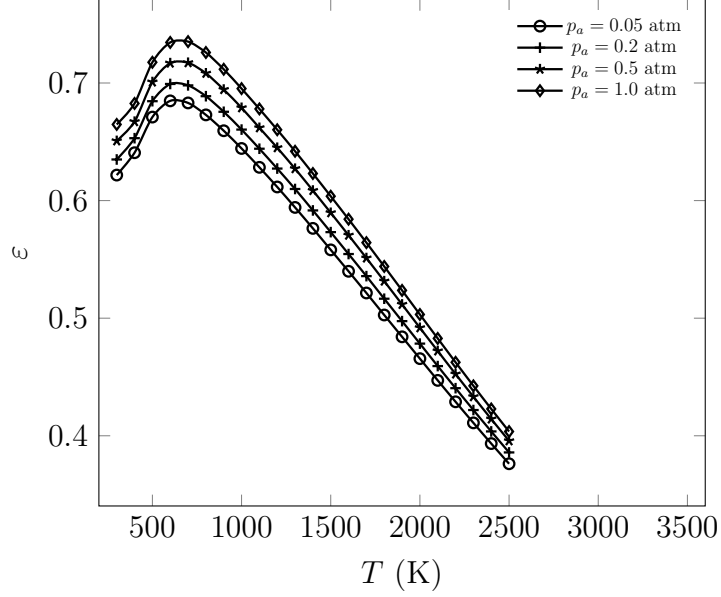


Figure 3.1 – Differences in total emittances due to partial pressure variation at a pressure-path-length of 6 atm.m.

This work, however, plots the total emittances as a function of the pressure-path-length as depicted in Figure 3.1, because the total pressure in this study is kept constant at 1 atm, whereas in the study present by Coelho and França, 2018, it was varying from 1 to 40 atm. Therefore, it was considered pressure-path-lengths varying from 0.0005 to 6 atm.m for both scenarios.

3.3 Obtaining the WSGG Correlations

Traditionally, the WSGG method considers the process outlined in Section 2.8.2.1, this work, however, made different assumptions for the two different scenarios for which the WSGG coefficients are generated. Although the steps are the same for both scenarios, this work found that it was better to present the scenarios in separate sections to assess the differences between each one.

3.3.1 WSGG Correlations Accounting for Partial Pressure Variations

To turn the explanation of the method clear, Equation (2.31) is rewritten:

$$\varepsilon(T, p_a S) = \sum_{i=1}^I w_i(T) [1 - \exp(-k_{p,i} p_a S)]$$

where, in this new method, [Wang and Xuan, 2019], $w_i(T)$ is a weighting function based not only in the temperature, but also in the p_a , as in:

$$w_i(T, p_a) = \sum_{j=0}^J a_{i,j} \left(\frac{T}{T_{ref}} \right)^j \sum_{k=0}^K b_{i,k} \left(\frac{p_a}{p_{a,ref}} \right)^k \quad (3.1)$$

where T_{ref} , fixed at 1000 K, and $p_{a,ref}$, fixed at 1 atm, are respectively the temperature, and partial pressure of reference. Note that $p_{a,ref}=1$ will not change the coefficients mathematically; however, this work decided to keep it as a way of maintaining the term dimensionless. Equation (2.31) becomes:

$$\varepsilon(T, p_a S, p_a) = \sum_{i=1}^I w_i(T, p_a) [1 - \exp(-k_{p,i} p_a S)] \quad (3.2)$$

and Equation (2.33), which represents the transparent window, becomes:

$$w_0(T, p_a) = 1 - \sum_{i=1}^I a_i(T) b_i(p_a) \quad (3.3)$$

To simplify the explanation, Equation (3.2) is rewritten utilizing sub-indexes, as in:

$$\varepsilon_{n,u,v} = \sum_{i=1}^I a_i(T_n) b_i(p_{a,v}) \{1 - \exp[-k_{p,i}(p_a S)_u]\} \quad (3.4)$$

where for the presenting scenario, $n = 23$, $u = 24$, and $v = 9$. Note that the sub-indexes n , u , and v represent the 23 temperatures, the 24 pressure-path-length, and the 9 mole concentrations, described in Section 3.1. Thus, the number of total emittances used on this scenario was 4968. Also, because the total pressure was kept at 1 atm, the molar concentrations have the same value as the partial pressures and are expressed here as the second, namely p_a .

Before proceeding with the use of the Levenberg-Marquardt method, [Marquardt, 1963], to determine the WSGG coefficients, the emittances that were obtained by the LBL integrations of Equation (2.11) were summed up. The summations that follow were a necessity to perform the curve fitting; otherwise, the number of unknown parameters would be too high, which would jeopardize the accuracy of the fitting algorithm.

That being said, the total emittances are firstly summed up for each p_a , as in:

$$\varepsilon_{n,u,V} = \sum_{v=1}^V \varepsilon_{n,u,v} \quad (3.5)$$

where $\varepsilon_{n,u,V}$ is, according to Equation (3.4):

$$\varepsilon_{n,u,V} = \sum_{i=1}^I a_i(T_n) B_i \{1 - \exp[-k_{p,i}(p_a S)_u]\} \quad (3.6)$$

in which B_i is described by:

$$B_i = \sum_{v=1}^V b_i(p_{a,v}) \quad (3.7)$$

Next, the 552 $\varepsilon_{n,u,V}$ emittances with different temperatures were added together as in:

$$\varepsilon_{N,u,V} = \sum_{n=1}^N \varepsilon_{n,u,V} \quad (3.8)$$

which resulted in 24 $\varepsilon_{N,u,V}$ emittances represented by:

$$\varepsilon_{N,u,V} = \sum_{i=1}^I A_i B_i \{1 - \exp[-k_{p,i}(p_a S)_u]\} \quad (3.9)$$

where A_i is composed by:

$$A_i = \sum_{n=1}^N a_i(T_n) \quad (3.10)$$

By having all of the 24 $\varepsilon_{N,u,V}$ emittances, the set of $A_i B_i$ and $k_{p,i}$ could be determined. This study performed analyses with 3, 4, 5, and 6 i gray-gases before choosing the one with a better performance, finding results that concur with those presented by Ziemniczak, 2014. It is noteworthy to say that the correlations with 5, and 6 gray gases returned better results, yet not significantly. The increase in the number of gray gases significantly rises the computation time in complex problems, therefore, this study opted to report a correlation with 4 gray gases. Having 4 gray gases gave an amount of 8 unknowns, 4 $A_i B_i$, and 4 $k_{p,i}$ that were fitted against Equation (3.9) using a non-linear regression by the Levenberg-Marquardt method, [Marquardt, 1963].

In possession of the absorption coefficients, $k_{p,i}$, and the summation of the weighting function, it was possible to obtain each coefficient a_i , and b_i . Note that determining firstly the coefficients a_i or b_i is simply a matter of choice. To fit the coefficients a_i , the

Levenberg-Marquardt method, [Marquardt, 1963], was used over Equation (3.6).

One step that is worth pointing out was the determination of the fraction pertaining to A_i , and B_i . Since $A_i B_i$ is a product from their multiplication, any value could be assumed for either A_i or B_i , insofar the other one respects the limit imposed by the obtained product $A_i B_i$. Wang and Xuan, 2019, let their summation B_i to be equal to 1. This work found that, although the choice of these values does not compromise the final results when using the correlations, leaving B_i equals 1 returned coefficients with different magnitude. Thus, this work preferred to relate A_i , and B_i by:

$$\frac{A_i}{N} = \frac{B_i}{V} \quad (3.11)$$

Note that Equation (3.11) does not guarantee that the coefficients will have the same magnitude, but it increases the likelihood.

The next step was to obtain the coefficients b_i . To do so, all of 23 emittances with different temperature were summed up, which gives:

$$\varepsilon_{N,u,v} = \sum_{i=1}^I A_i b_i(p_{a,v}) \{1 - \exp[-k_{p,i}(p_a X)_u]\} \quad (3.12)$$

The Levenberg-Marquardt method, [Marquardt, 1963], was used over Equation (3.12) to fit the coefficients b_i , which resulted in a set of 36 coefficients, 9 for each gray gas.

Finally, a multiple linear regression was performed over the coefficients a_i , and b_i , according to:

$$a_i = \sum_{j=0}^J c_{i,j} \left(\frac{T}{T_{ref}} \right)^j \quad (3.13)$$

$$b_i = \sum_{k=0}^K d_{i,k} \left(\frac{p_a}{p_{a,ref}} \right)^k \quad (3.14)$$

The best fit was obtained by choosing $J = 6$, and $K = 4$. However, note that some polynomials have a value of 0. The criterion to choose which one should be discarded was excluding those with the lowest statistical significance, in other words, the highest p-value [Neter et al., 1996]. It was tested values for $J = 6$, $J = 5$, $J = 4$, $K = 5$, and $K = 3$ with or without empty polynomials. These polynomials returned results that were either inferior to those chosen by this work, or else with a very small increase in the performance

of the results. The correlations obtained are presented on Tables 3.1, and 3.2.

Table 3.1 – WSGG Correlations for a varying p_a , and MR= 1

i	1	2	3	4
$k_{p,i}(atm^{-1}m^{-1})$	1.80778×10^{-1}	1.56481×10^0	1.03154×10^1	1.14971×10^2
$c_{i,0}$	1.74036×10^{-1}	1.93932×10^{-1}	5.507535×10^{-1}	7.46039×10^{-1}
$c_{i,1}$	1.06395×10^0	9.02860×10^{-1}	1.50900×10^{-1}	-8.03330×10^{-1}
$c_{i,2}$	-9.29222×10^{-1}	-6.71660×10^{-1}	-4.16472×10^{-1}	4.62676×10^{-1}
$c_{i,3}$	2.88206×10^{-1}	1.33405×10^{-1}	1.36001×10^{-1}	-1.28031×10^{-1}
$c_{i,4}$	-	-	-	-
$c_{i,5}$	-	-	-	-
$c_{i,6}$	-3.75740×10^{-3}	-4.25643×10^{-4}	-1.40766×10^{-3}	1.72256×10^{-3}
$d_{i,0}$	6.00348×10^{-1}	4.02562×10^{-1}	2.87996×10^{-1}	2.12769×10^{-1}
$d_{i,1}$	-1.33251×10^{-2}	1.48382×10^{-1}	1.16449×10^{-1}	2.28745×10^{-2}
$d_{i,2}$	-6.09976×10^{-3}	-1.16250×10^{-1}	-5.27849×10^{-2}	-1.68226×10^{-2}
$d_{i,3}$	-	-	-	-
$d_{i,4}$	5.11040×10^{-3}	2.94011×10^{-2}	9.51892×10^{-3}	3.59247×10^{-3}

Table 3.2 – WSGG Correlations for a varying p_a , and MR= 2

i	1	2	3	4
$k_{p,i}(atm^{-1}m^{-1})$	1.83614×10^{-1}	1.54146×10^0	9.56465×10^0	9.24920×10^1
$c_{i,0}$	1.70361×10^{-1}	2.42605×10^{-1}	3.62646×10^{-1}	8.75608×10^{-1}
$c_{i,1}$	9.30902×10^{-1}	6.06662×10^{-1}	7.59691×10^{-1}	-9.95653×10^{-1}
$c_{i,2}$	-7.82713×10^{-1}	-3.22620×10^{-1}	-9.34404×10^{-1}	5.40154×10^{-1}
$c_{i,3}$	2.48942×10^{-1}	2.21434×10^{-2}	2.78388×10^{-1}	-1.35278×10^{-1}
$c_{i,4}$	-	-	-	-
$c_{i,5}$	-	-	-	-
$c_{i,6}$	-3.46030×10^{-3}	7.67925×10^{-4}	-2.72643×10^{-3}	1.60693×10^{-3}
$d_{i,0}$	5.99632×10^{-1}	4.19496×10^{-1}	2.91318×10^{-1}	2.16969×10^{-1}
$d_{i,1}$	-3.97641×10^{-2}	1.58450×10^{-1}	1.83738×10^{-1}	3.72569×10^{-2}
$d_{i,2}$	2.01415×10^{-2}	-1.51614×10^{-1}	-1.04860×10^{-1}	-2.65611×10^{-2}
$d_{i,3}$	-	-	-	-
$d_{i,4}$	-2.88510×10^{-3}	4.49044×10^{-2}	2.23364×10^{-2}	7.42865×10^{-3}

3.3.2 WSGG Correlations Accounting for Mole Ratio Variations

The second scenario proposed by this work was concerned with the variations that occur in the mole ratio between the species along the medium. The steps taken to

determine the coefficients were the same presented on the previous Section and are further described. The changes on the weighting function are described by:

$$w_i(T, MR) = \sum_{j=0}^J a_{i,j} \left(\frac{T}{T_{ref}} \right)^j \sum_{k=0}^K b_{i,k} \left(\frac{MR}{MR_{ref}} \right)^k \quad (3.15)$$

in which the T_{ref} is also fixed at 1000 K, and the mole ratio of reference, MR_{ref} , at 1. Thus, Equation (3.2) becomes:

$$\varepsilon(T, p_a S, MR) = \sum_{i=1}^I w_i(T, MR) [1 - \exp(-k_{p,i} p_a S)] \quad (3.16)$$

and Equation (3.3) becomes:

$$w_0(T, MR) = 1 - \sum_{i=1}^I a_i(T) b_i(MR) \quad (3.17)$$

Equation (3.16) is rewritten utilizing sub-indexes, as in:

$$\varepsilon_{n,u,v} = \sum_{i=1}^I a_i(T_n) b_i(MR_v) \{1 - \exp[-k_{p,i}(p_a S)_u]\} \quad (3.18)$$

however, for this scenario the sub-indexes were $n = 23$, $u = 24$, and $v = 17$. Thus, the number of total emittances used in this scenario was 9384.

Before proceeding with the use of the Levenberg-Marquardt method, [Marquardt, 1963], to determine the WSGG coefficients, the emmittances that were obtained by the LBL integrations of Equation (2.11) were summed up. First, they were summed up for each MR, as in:

$$\varepsilon_{n,u,V} = \sum_{v=1}^V \varepsilon_{n,u,v} \quad (3.19)$$

where $\varepsilon_{n,u,V}$ is, according to Equation (3.18):

$$\varepsilon_{n,u,V} = \sum_{i=1}^I a_i(T_n) B_i \{1 - \exp[-k_{p,i}(p_a S)_u]\} \quad (3.20)$$

in which B_i is described by:

$$B_i = \sum_{v=1}^V b_i(MR_v) \quad (3.21)$$

Next, the 552 $\varepsilon_{n,u,V}$ emittances with different temperatures were added together

as in:

$$\varepsilon_{N,u,V} = \sum_{n=1}^N \varepsilon_{n,u,V} \quad (3.22)$$

which yielded 24 $\varepsilon_{N,u,V}$ emittances represented by:

$$\varepsilon_{N,u,V} = \sum_{i=1}^I A_i B_i \{1 - \exp[-k_{p,i}(p_a S)_u]\} \quad (3.23)$$

where A_i is composed by:

$$A_i = \sum_{n=1}^N a_i(T_n) \quad (3.24)$$

Again, after possessing all of the 24 $\varepsilon_{N,u,V}$ emittances, the set of $A_i B_i$, and $k_{p,i}$ were determined. For 4 gray gases there was a total of 8 uncertainties, 4 $A_i B_i$, and 4 $k_{p,i}$ that were fitted against Equation 3.23 using a non-linear regression by the Levenberg-Marquardt method, [Marquardt, 1963].

Like the previous Section, with the absorption coefficients, $k_{p,i}$, and the summation of the weighting function, it was possible to obtain each coefficient a_i , and b_i . To fit the coefficients a_i , the Levenberg-Marquardt method, [Marquardt, 1963], was used over Equation (3.20). Note that A_i , and B_i are still related by Equation (3.11).

The next step was to obtain the coefficients b_i . To do so, all of 23 emittances with different temperature were summed up, which gave:

$$\varepsilon_{N,u,v} = \sum_{i=1}^I A_i b_i(MR_v) \{1 - \exp[-k_{p,i}(p_a S)_u]\} \quad (3.25)$$

The Levenberg-Marquardt method, [Marquardt, 1963], was then used over Equation (3.25) to fit the coefficients b_i , which resulted in a set of 68 coefficients, 17 for each gray gas.

Finally, a multiple linear regression was performed over the coefficients a_i , and b_i , according to:

$$a_i = \sum_{j=0}^J c_{i,j} \left(\frac{T}{T_{ref}} \right)^j \quad (3.26)$$

$$b_i = \sum_{k=0}^K d_{i,k} \left(\frac{MR}{MR_{ref}} \right)^k \quad (3.27)$$

The best fit was obtained by choosing $J = 6$, and $K = 5$. However, note that some polynomials have a value of 0. In the same way, as in the previous section, it was tested values for $J = 6$, $J = 5$, $J = 4$, $K = 4$, and $K = 3$ with or without empty polynomials, all returning results that were either inferior to those chosen by this work, or else with a very small increase in the performance of the results. The correlations obtained are presented in Table 3.3.

Table 3.3 – WSGG Correlations for a varying MR.

i	1	2	3	4
$k_{p,i}(atm^{-1}m^{-1})$	2.74007×10^{-1}	2.31206×10^0	1.48023×10^1	1.46057×10^2
$c_{i,0}$	2.57823×10^{-1}	3.74157×10^{-1}	6.83747×10^{-1}	1.01631×10^0
$c_{i,1}$	1.34476×10^0	8.97602×10^{-1}	3.63029×10^{-1}	-1.20013×10^0
$c_{i,2}$	-1.08276×10^0	-6.59427×10^{-1}	-7.09822×10^{-1}	6.91435×10^{-1}
$c_{i,3}$	3.09520×10^{-1}	1.17883×10^{-1}	2.21694×10^{-1}	-1.80620×10^{-1}
$c_{i,4}$	-	-	-	-
$c_{i,5}$	-	-	-	-
$c_{i,6}$	-3.66191×10^{-3}	-1.72082×10^{-4}	-2.03789×10^{-3}	2.18097×10^{-3}
$d_{i,0}$	3.71883×10^{-1}	1.46210×10^{-1}	1.20440×10^{-1}	1.54727×10^{-1}
$d_{i,1}$	1.32616×10^{-1}	2.59390×10^{-1}	1.25177×10^{-1}	4.17724×10^{-3}
$d_{i,2}$	-8.79355×10^{-2}	-1.38732×10^{-1}	-5.56956×10^{-2}	-1.23597×10^{-2}
$d_{i,3}$	1.94644×10^{-2}	2.87518×10^{-2}	1.10545×10^{-2}	3.11641×10^{-3}
$d_{i,4}$	-	-	-	-
$d_{i,5}$	-3.09648×10^{-4}	-4.38876×10^{-4}	-1.66442×10^{-4}	-5.19114×10^{-5}

3.3.2.1 WSGG Correlations for the Lower MR Range

One question that arose during the investigations performed by this study was the one concerning the necessity of having coefficients for a wide MR range. It may be the case that the whole MR range can be split into two different ranges, one to dry-FGR, and other to wet-FGR oxy-fuel combustions. As pointed by Kangwanpongpan et al., 2012, the former is characterized by having higher concentrations of CO_2 , whereas the latter has higher H_2O concentrations. Therefore, this work generated two separated correlations, one where the MR range from 0.125 to 1, and the other with a MR range of 1-4. In both cases there were considered 5 different MR, namely 0.125, 0.25, 0.5, 0.75, and 1 for the dry-FGR scenario, and 1, 1.5, 2, 3, and 4 for the wet-FGR.

Also, the partial pressure of the medium when generating these correlations is

different from those for a wider MR range. When the MR range was of 0.125-1, the chosen partial pressures for H₂O were 0.0125, 0.025, 0.05, 0.075, and 0.1. On the other hand, when the MR range was of 1-4, the CO₂ was kept at 0.2 atm, while the H₂O was allowed to vary to return the respective MR values. The process to obtain these correlations was the same one that is presented in the last Section. The final correlations are presented in Table 3.4.

Table 3.4 – WSGG Correlations for smaller MR range.

0.125 ≤ MR < 1				
i	1	2	3	4
$k_{p,i}(\text{atm}^{-1}\text{m}^{-1})$	2.56900×10^{-1}	2.37694×10^0	1.67647×10^1	2.02412×10^2
$c_{i,0}$	1.19287×10^{-1}	2.56460×10^{-1}	5.45102×10^{-1}	3.04252×10^{-1}
$c_{i,1}$	1.11367×10^0	3.58287×10^{-1}	-5.43683×10^{-1}	-1.23141×10^{-1}
$c_{i,2}$	-1.04372×10^0	-3.25104×10^{-1}	3.22953×10^{-1}	1.89903×10^{-2}
$c_{i,3}$	3.06185×10^{-1}	6.91816×10^{-2}	-8.76822×10^{-2}	-1.43750×10^{-2}
$c_{i,4}$	-	-	-	-
$c_{i,5}$	-	-	-	-
$c_{i,6}$	-3.34942×10^{-3}	-2.97552×10^{-4}	9.76511×10^{-4}	5.95146×10^{-4}
$d_{i,0}$	6.30520×10^{-1}	2.64708×10^{-1}	2.47889×10^{-1}	2.50078×10^{-1}
$d_{i,1}$	7.46418×10^{-1}	8.96457×10^{-1}	3.51884×10^{-1}	2.30975×10^{-2}
$d_{i,2}$	-1.01899×10^0	-8.96520×10^{-1}	-2.89348×10^{-1}	-6.19871×10^{-2}
$d_{i,3}$	4.60946×10^{-1}	3.58839×10^{-1}	1.10681×10^{-1}	2.65810×10^{-2}
1 ≤ MR ≤ 4				
i	1	2	3	4
$k_{p,i}$	2.78001×10^{-1}	2.26402×10^0	1.39251×10^1	1.24525×10^2
$c_{i,0}$	2.34031×10^{-1}	3.13909×10^{-1}	4.83381×10^{-1}	1.03359×10^0
$c_{i,1}$	9.76012×10^{-1}	8.05445×10^{-1}	7.31036×10^{-1}	-1.32112×10^0
$c_{i,2}$	-7.09132×10^{-1}	-5.55368×10^{-1}	-9.92786×10^{-1}	7.70431×10^{-1}
$c_{i,3}$	1.99115×10^{-1}	9.02360×10^{-1}	2.99978×10^{-1}	-1.93755×10^{-1}
$c_{i,4}$	-	-	-	-
$c_{i,5}$	-	-	-	-
$c_{i,6}$	-2.50201×10^{-3}	3.80010×10^{-5}	-2.81302×10^{-3}	2.11701×10^{-3}
$d_{i,0}$	4.85986×10^{-1}	2.40638×10^{-1}	1.55673×10^{-1}	1.95398×10^{-1}
$d_{i,1}$	7.74001×10^{-3}	9.75670×10^{-2}	7.24740×10^{-2}	-1.60931×10^{-2}
$d_{i,2}$	-3.95002×10^{-3}	-2.41790×10^{-2}	-1.4170×10^{-2}	1.01801×10^{-3}
$d_{i,3}$	4.65001×10^{-4}	2.29600×10^{-3}	1.20902×10^{-3}	2.10019×10^{-5}

4 DESCRIPTION OF THE TEST CASES

This Chapter will be dedicated to describe all the cases tested. The domain in which all the simulations are performed is the same presented in Figure (2.5), where the length X is fixed at 1 m and divided into 200 finite volumes spaced equally between each other. This mesh refinement was chosen after performing a Grid Convergence Index according to gci, 2008. Once again, it is stressed out that all the cases considered a total pressure of 1 atm.

4.1 Cases for Varying Partial Pressures

There are 10 different cases regarding the scenario accounting for the differences in partial pressure. The first six cases were those presented by Dorigon et al., 2013; the other four were proposed by this paper. In the following discussion the cases name for a varying partial pressure are preceded by the letter p , where the first number describes the MR, and the latter distinguishes the temperature and mole concentration profiles.

For cases p1.1, and p2.1, the temperature profile, as well as the mole concentration profile, has only a peak of temperature and concentration located right in the middle of the domain. The next two equations describe the changes regarding temperature and CO₂ mole concentrations for the two aforementioned cases.

$$T(x) = 400 \text{ K} + (1400 \text{ K})\sin^2(\pi x/X) \quad (4.1)$$

$$Y_{CO_2}(x) = 0.1\sin^2(\pi x/X) \quad (4.2)$$

The Case p1.2, as well as the Case p2.2, have two peaks of temperature, and mole concentrations. Note that the only difference between these two cases lies in the MR. Similarly to the former two cases, the temperature also peaks at 1800 K, as in:

$$T(x) = 400 \text{ K} + (1400 \text{ K})\sin^2(2\pi x/X) \quad (4.3)$$

and Y_{CO_2} peaks at 0.1.

$$Y_{CO_2}(x) = 0.1\sin^2(2\pi x/X) \quad (4.4)$$

The last two cases proposed by Dorigon et al., 2013, p1.3, and p2.3, consist in an asymmetrical profile for temperature, and molar concentration. Also, note that in these cases, one wall was kept at 880 K, and the other was kept at 400 K, as shown by:

$$\begin{aligned} T(x) &= 880 \text{ K} + (920 \text{ K})\sin^2(2\pi x/X) && \text{if } (x/X) \leq 0.25 \\ T(x) &= 400 \text{ K} + (1400 \text{ K}) \left[1 - \sin^{(3/2)} \left(\frac{2\pi x}{3X} - 0.25 \right) \right] && \text{if } (x/X) > 0.25 \end{aligned} \quad (4.5)$$

The peak molar concentration for cases p1.3, and p2.3 is 0.25, according to:

$$\begin{aligned} Y_{CO_2}(x) &= 0.25\sin^2(2\pi x/X) && \text{if } (x/X) \leq 0.25 \\ Y_{CO_2}(x) &= 0.25 \left[1 - \sin^{(3/2)} \left(\frac{2\pi x}{3X} - 0.25 \right) \right] && \text{if } (x/X) > 0.25 \end{aligned} \quad (4.6)$$

Note that in all cases proposed by Dorigon et al., 2013, the partial pressure varied along the path-length; however, the average partial pressures were 0.2 atm for cases with MR= 1, and 0.3 atm for cases with MR= 2. To better assess the influence of the partial pressure variations, this work proposed two extra profiles where the average partial pressures were 0.4, and 0.6 atm for MR= 1, and MR= 2, respectively. The following equation gives the profile temperature for cases p1.4, and p2.4, which has only one peak for temperature right in the middle of the path-length.

$$T(x) = 300 \text{ K} + (1500 \text{ K})\sin^2(\pi x/X) \quad (4.7)$$

Note that for Case p1.4 the peak of Y_{CO_2} equals 0.4, as shown by:

$$Y(x) = 0.4\sin^2(\pi x/X) \quad (4.8)$$

For Case p2.4, the peak for the Y_{CO_2} is a little lower, as:

$$Y(x) = 0.3\sin^2(\pi x/X) \quad (4.9)$$

Finally, there are cases p1.5, and p2.5, which have two peaks for temperature, and two peaks for molar concentrations. The next equation describes the temperature along the path-length.

$$T(x) = 300 \text{ K} + (1500 \text{ K})\sin^2(2\pi x/X) \quad (4.10)$$

For Case p1.5, the equation describing the molar concentration behavior of CO₂ is:

$$Y(x) = 0.4\sin^2(2\pi x/X) \quad (4.11)$$

On the other hand, for the Case p2.5, the equation for Y_{CO_2} is:

$$Y(x) = 0.3\sin^2(2\pi x/X) \quad (4.12)$$

To summarize all the cases regarding variations in the partial pressure, this work presents Table 4.1:

Table 4.1 – Cases summary for partial pressure variations.

Cases	T(x) K	$Y_{CO_2}(x)$
p1.1 & p2.1	$400 + 1400\sin^2(\pi x/X)$	$0.1\sin^2(\pi x/X)$
p1.2 & p2.2	$400 + 1400\sin^2(2\pi x/X)$	$0.1\sin^2(2\pi x/X)$
p1.3 & p2.3	$880 + 920\sin^2(2\pi x/X)$	$0.25\sin^2(2\pi x/X)$
	$400 + 1400 \left[1 - \sin^{(3/2)}\left(\frac{2\pi x}{3X} - 0.25\right)\right]$	$0.25 \left[1 - \sin^{(3/2)}\left(\frac{2\pi x}{3X} - 0.25\right)\right]$
p1.4	$300 + 1500\sin^2(\pi x/X)$	$0.4\sin^2(\pi x/X)$
p1.5	$300 + 1500\sin^2(2\pi x/X)$	$0.4\sin^2(2\pi x/X)$
p2.4	$300 + 1500\sin^2(\pi x/X)$	$0.3\sin^2(\pi x/X)$
p2.5	$300 + 1500\sin^2(2\pi x/X)$	$0.3\sin^2(2\pi x/X)$

Following is a set of figures illustrating the temperature profiles for the cases with varying partial pressure.

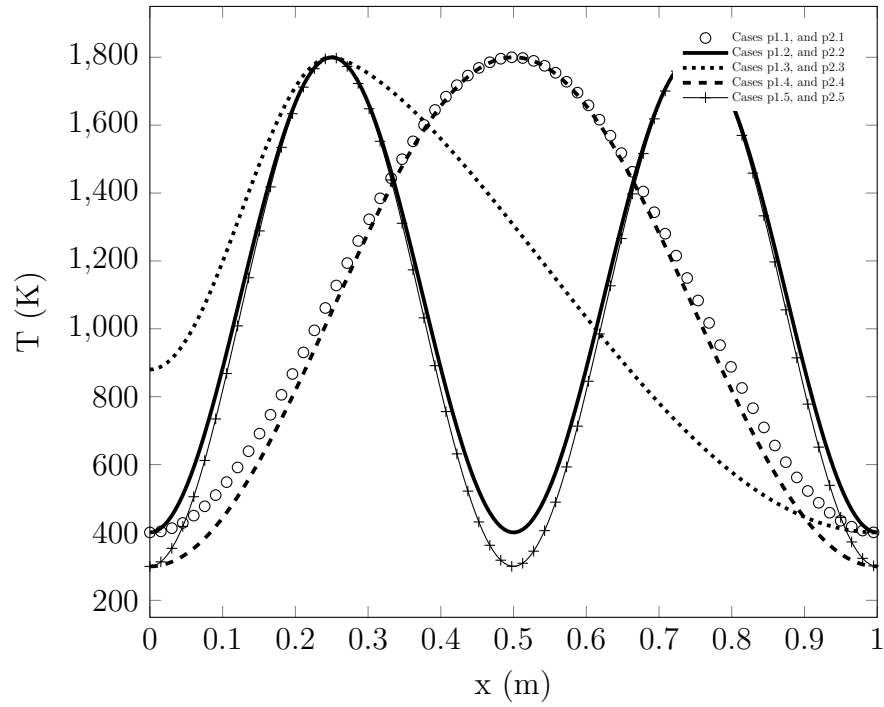


Figure 4.1 – Temperature profiles for cases with varying partial pressure.

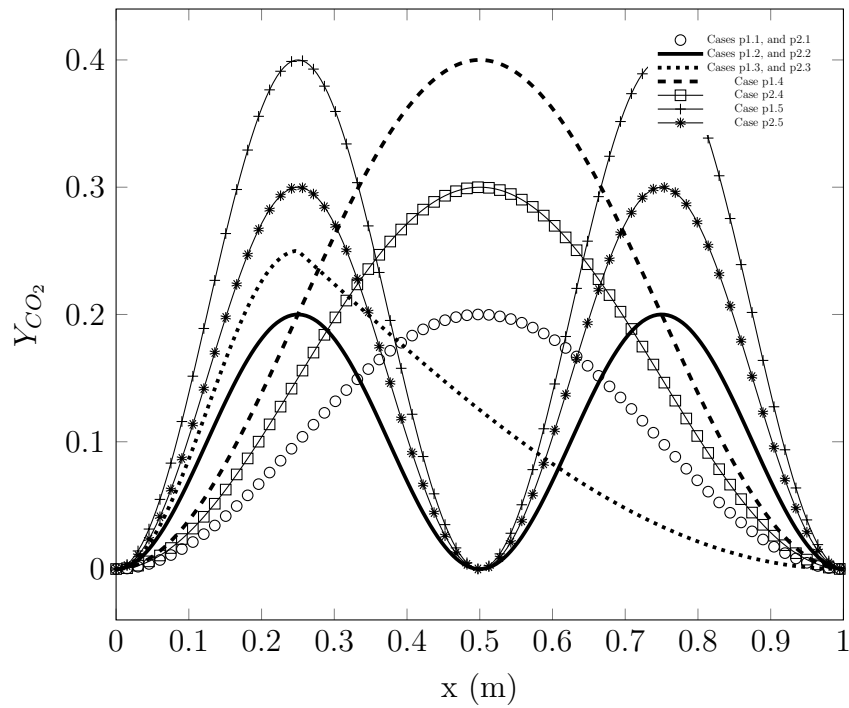


Figure 4.2 – Molar concentration profiles for cases with varying partial pressure.

4.2 Cases for Varying Mole Ratio

When the MR varies, there are a considerable amount of cases being tested. Cases m1.1 to m3.5, are presented in the work of Kangwanpongpan et al., 2012. Note that some of the cases presented in Kangwanpongpan et al., 2012, are similar to those of Johansson et al., 2011. The other two cases, m4.1 and m4.2, are proposed by this work. Note that differently from the last scenario, the nomenclature of this scenario's cases does not follow the same logic. The cases for this scenario are preceded by the letter m , with the number that follows indicating the temperature and MR variations: namely 1 for homogeneous temperature and MR; 2 for non-homogeneous temperature, but homogeneous MR; 3 for both non-homogeneous temperature and MR; and finally 4 to name the profiles proposed by this paper. The last number is used only to distinguish the cases within the same group.

Cases m1.1 and m1.2, as said before, deal with homogeneous temperature media, and mole concentration. The temperature profile for cases m1.1 and m1.2 is given by:

$$\begin{aligned} T_w &= 700 \text{ K} \\ T &= 1200 \text{ K} \end{aligned} \tag{4.13}$$

In the Case m1.1, the mole concentration for CO₂ was kept constant at 0.8, and for H₂O at 0.125. Case m1.2, on the other hand, had both CO₂, and H₂O kept at 0.48.

For cases m2.1 to m3.5 the temperature profile is given by:

$$\begin{aligned} T_w &= 700 \text{ K} \\ T(x) &= 1400 \text{ K} - (400 \text{ K})\cos(2\pi x/X) \end{aligned} \tag{4.14}$$

Cases m2.1, and m2.2, have constant mole concentration within its media. In the Case m2.1 the mole concentrations were 0.8 and 0.125, for CO₂, and H₂O, respectively. In the Case m2.2, both CO₂, and H₂O molar concentrations were kept at 0.48.

The mole concentration for H₂O on Case m3.1 is given by:

$$Y_{H_2O}(x) = 0.12 + 0.04\cos(2\pi x/X) \tag{4.15}$$

and the CO₂ concentration was kept at 0.8, which according to Kangwanpongpan et al., 2012, represents dry-FGR oxy-fuel conditions in practical flames.

Kangwanpongpan et al., 2012, also presented four more media profiles in order

to better test the obtained WSGG coefficients. For cases m3.2, and m3.3, the mole concentration is given by:

$$Y_{(H_2O\text{ or }CO_2)}(x) = 0.12 + 0.09\cos(2\pi x/X) \quad (4.16)$$

In the Case m3.2, CO_2 concentration is represented by Equation (4.16), while H_2O was kept constant at 0.12. In the Case m3.3, H_2O concentration is described by Equation (4.16), while CO_2 was kept constant at 0.12.

The last two cases from Kangwanpongpan et al., 2012, are cases m3.4, and m3.5, which have molar concentrations governed by:

$$Y_{(H_2O\text{ or }CO_2)}(x) = 0.15 + 0.075\cos(2\pi x/X) \quad (4.17)$$

Case m3.4 had H_2O kept constant at 0.15, while the CO_2 concentration is given by Equation (4.17). Conversely, Case m3.5 had CO_2 kept constant at 0.15, and H_2O concentration described by Equation (4.17).

To do a better verification, this work introduced two more profiles. Both of them have varying temperature, and molar concentration. Equation (4.1) represents the temperature profile that is used on cases m4.1, and m4.2.

The idea behind the profiles presented by this work was to evaluate the performance of the WSGG coefficients for values of MR that are either smaller or greater than 1. This way the profiles represented a hypothetical situation of dry-FGR or wet-FGR oxy-fuel combustion.

Case m4.1 has the CO_2 concentration governed by:

$$Y_{CO_2}(x) = 0.1 + 0.7\sin^2(\pi x/X) \quad (4.18)$$

while the H_2O concentration was kept at 0.1. The MR within the media for Case m4.1 varied from 0.125 to 1.

In order to have a profile where the MR is always greater than 1, Case m4.2 was idealized. The H_2O concentration is described by:

$$Y_{H_2O}(x) = 0.1 + 0.3\sin^2(\pi x/X) \quad (4.19)$$

and the CO_2 was kept at 0.1.

The respective cases are summarised on the following table.

Table 4.2 – Cases summary for MR variations.

Case	$Y_{CO_2}(x)$	$Y_{H_2O}(x)$	MR Range	T(x) K
m1.1	0.8	0.125	0.125	1200
m1.2	0.48	0.48	1.0	1200
m2.1	0.8	0.125	0.125	$1400 - (400)\cos(2\pi x/X)$
m2.2	0.48	0.48	1.0	$1400 - (400)\cos(2\pi x/X)$
m3.1	0.8	$0.12 + 0.04\cos(2\pi x/X)$	0.10 to 0.20	$1400 - 400\cos(2\pi x/X)$
m3.2	$0.12 + 0.09\cos(2\pi x/X)$	0.12	0.57 to 4.0	$1400 - 400\cos(2\pi x/X)$
m3.3	0.12	$0.12 + 0.09\cos(2\pi x/X)$	0.25 to 1.75	$1400 - 400\cos(2\pi x/X)$
m3.4	$0.15 + 0.075\cos(2\pi x/X)$	0.15	0.67 to 2.0	$1400 - 400\cos(2\pi x/X)$
m3.5	0.15	$0.15 + 0.075\cos(2\pi x/X)$	0.5 to 1.5	$1400 - 400\cos(2\pi x/X)$
m4.1	$0.1 + 0.7\sin^2(\pi x/X)$	0.1	0.125 to 1.0	$400 + 1400\sin^2(\pi x/X)$
m4.2	0.1	$0.1 + 0.3\sin^2(\pi x/X)$	1.0 to 4.0	$400 + 1400\sin^2(\pi x/X)$

As commented in the work of Dorigon et al., 2013, other profiles for temperature, and molar concentrations could very well be used. However, the other profiles that were tested returned results that were similar to those presented in this study. Following, Figures 4.3 and 4.4 illustrate respectively the temperature, and water vapor molar concentration profiles for some cases with a varying MR.

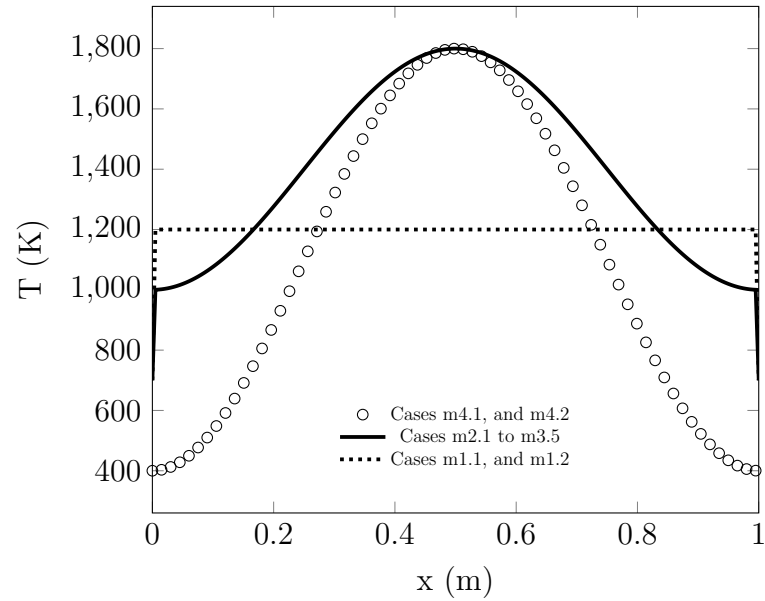


Figure 4.3 – Temperature profiles for cases with a varying MR.

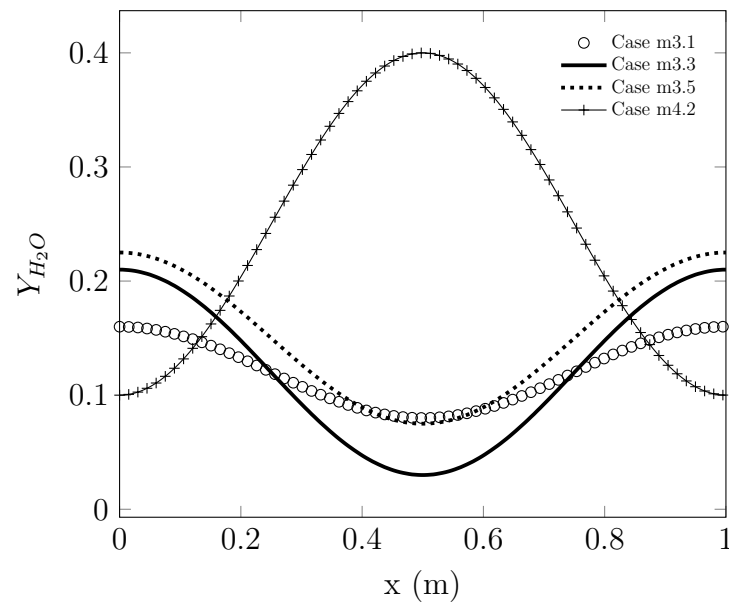


Figure 4.4 – Molar concentration profiles for cases with a varying MR.

Finally, Figure 4.5 shows the MR variations within the proposed cases for a varying MR. Note that the cases with a fixed MR were not plotted.

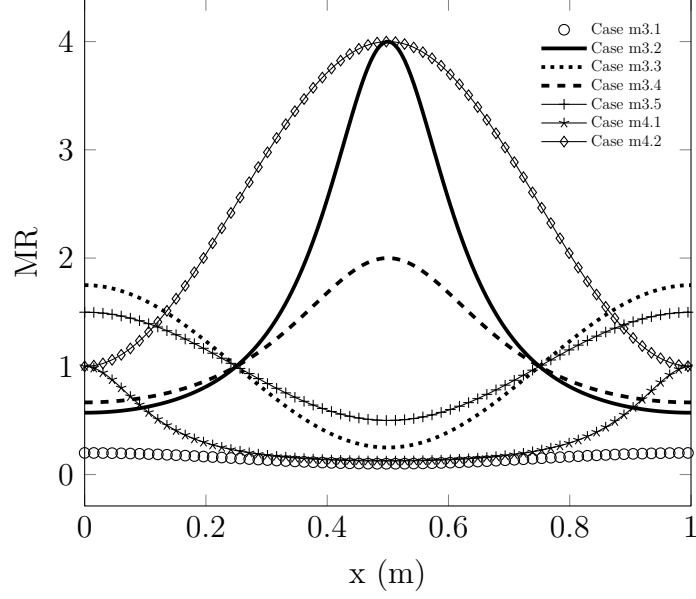


Figure 4.5 – MR variations within the proposed profiles.

4.3 Assessment of WSGG Correlations Deviations

The performance of the WSGG models presented by this study were compared for the maximum and average radiative heat source, and radiative heat flux. The deviations were obtained from the comparison with the LBL benchmark solution as follows:

$$\chi(x) = \frac{|q''_{WSGG}(x) - q''_{LBL}(x)|}{\max|q''_{LBL}|} \times 100\% \quad (4.20a)$$

$$\delta(x) = \frac{|\nabla q''_{WSGG}(x) - \nabla q''_{LBL}(x)|}{\max|\nabla q''_{LBL}|} \times 100\% \quad (4.20b)$$

where $\chi(x)$, and $\delta(x)$ are the local deviations of radiative heat flux and radiative heat source, respectively.

5 RESULTS AND DISCUSSION

In this Chapter are presented the obtained results for all the cases that were pro-posed in the last Chapter. To turn the reading easier, the results are disposed in two distinct sections.

5.1 Results for Varying Partial Pressures

5.1.1 Results for Total Emittance

To test the capabilities of the different WSGG models in solving the RTE, the most important results are those of radiative heat source, and radiative heat flux. This way, it was decided to plot just a few amount of the total emittances obtained using the fitted correlations. Figure 5.1 shows the fitting for emittances at a partial pressure of 0.05 atm.

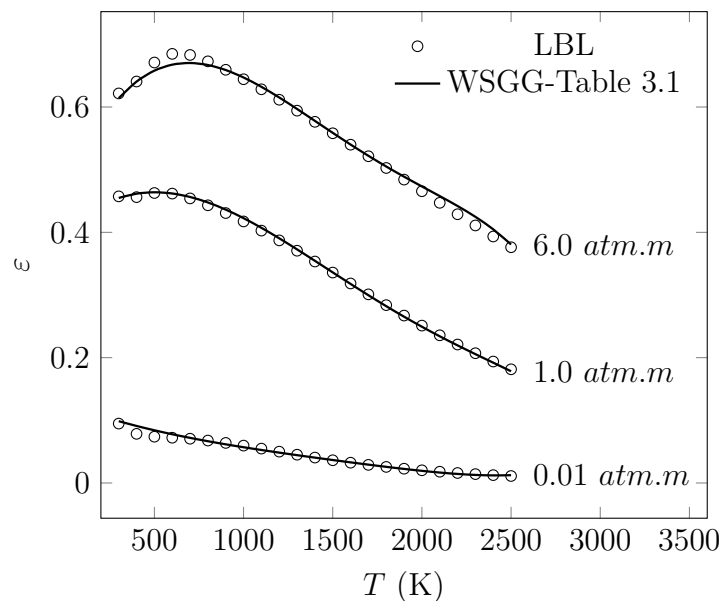


Figure 5.1 – Comparison between emittances for $MR=1$ and $p_a = 0.05 \text{ atm}$.

Figure 5.2 shows the fitted emittances for partial pressure equals 0.2 atm, and different pressure-path-length.

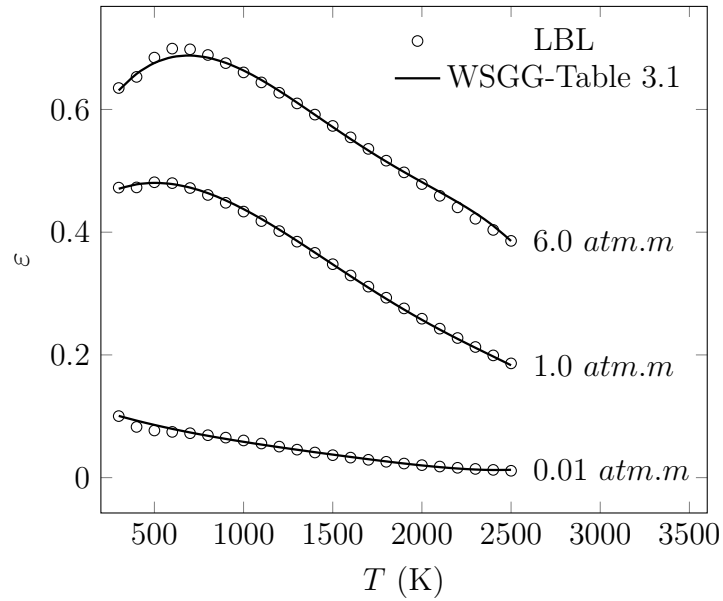


Figure 5.2 – Comparison between emittances for MR= 1 and $p_a = 0.2 \text{ atm}$.

Also, for a MR kept at 1, Figure 5.3 shows the total emittances for a partial pressure of 0.5 atm.

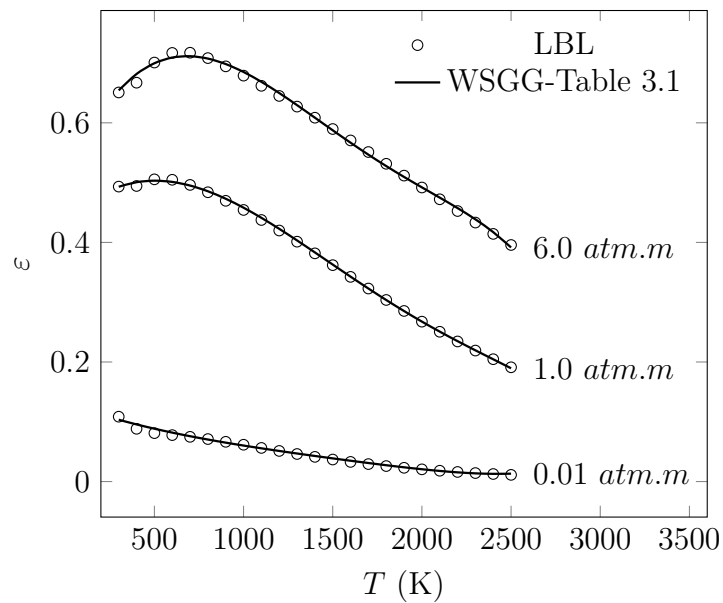


Figure 5.3 – Comparison between emittances for MR= 1 and $p_a = 0.5 \text{ atm}$.

Finally, there is presented the total emittances for a partial pressure of 1.0 atm, and MR= 1.

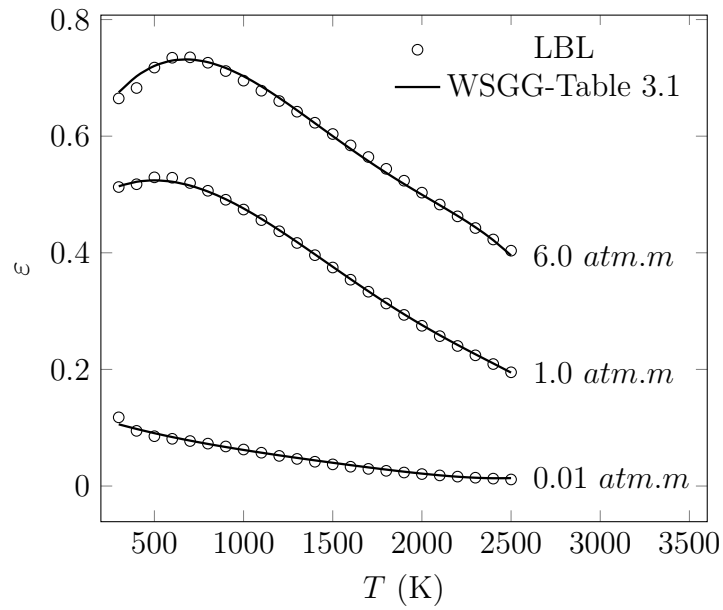


Figure 5.4 – Comparison between emittances for MR= 1 and $p_a = 1.0 \text{ atm}$.

The following figures will present a few examples of fitted emittances for MR= 2. Figure 5.5 shows three different pressure-path-length for a partial pressure of 0.075 atm.

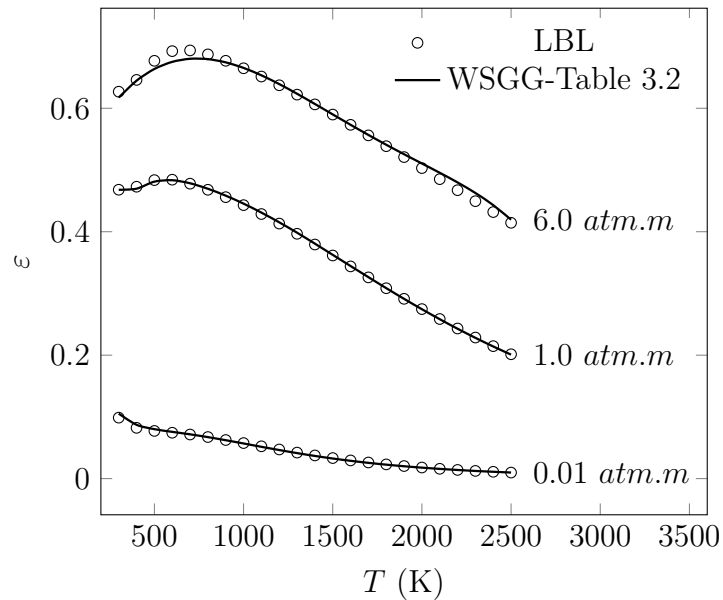


Figure 5.5 – Comparison between emittances for MR= 2 and $p_a = 0.075 \text{ atm}$.

Figure 5.6 represents a medium with a partial pressure of 0.3 atm, which is the same partial pressure for which Dorigon et al. [2013] generated WSGG correlations.

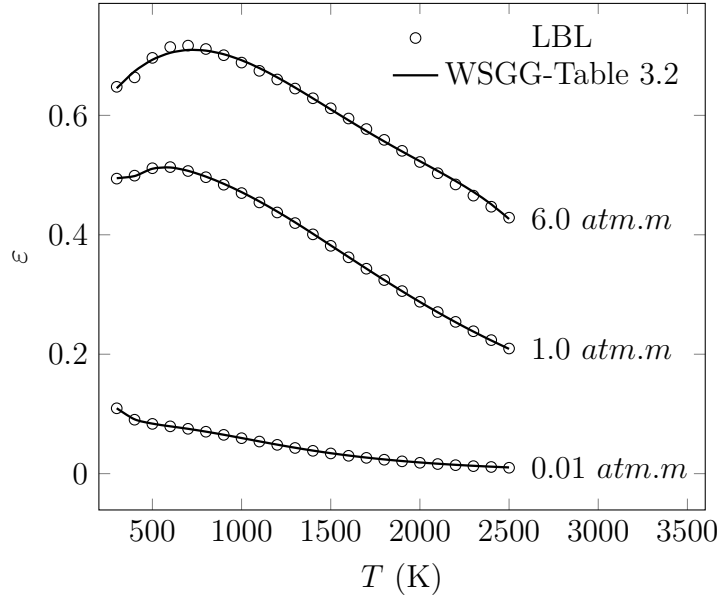


Figure 5.6 – Comparison between emittances for MR= 1 and $p_a = 0.3 \text{ atm}$.

Next, Figure 5.7 represents a partial pressure of 0.6 atm, and also three pressure-path-lengths.

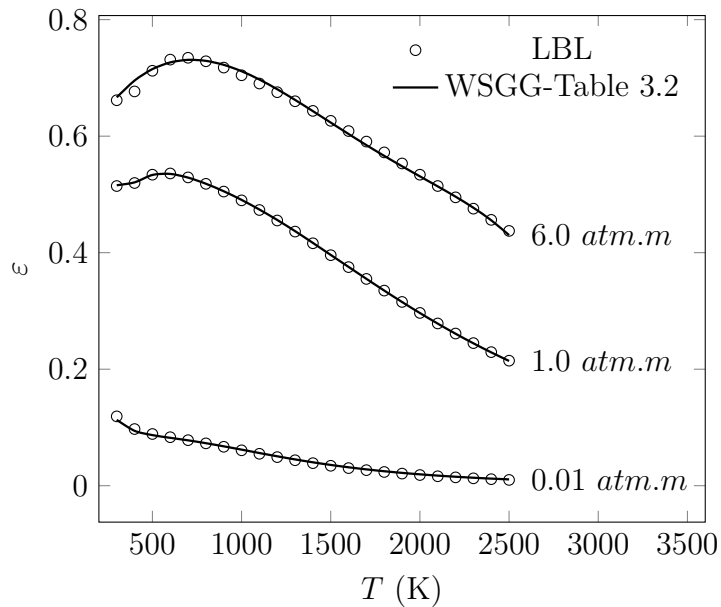


Figure 5.7 – Comparison between emittances for MR= 2 and $p_a = 0.6 \text{ atm}$.

At last, it is presented a plot for partial pressure of 1.0 atm and MR= 2. Note that the deviations tended to increase as the pressure-path-length and the partial pressure increased.

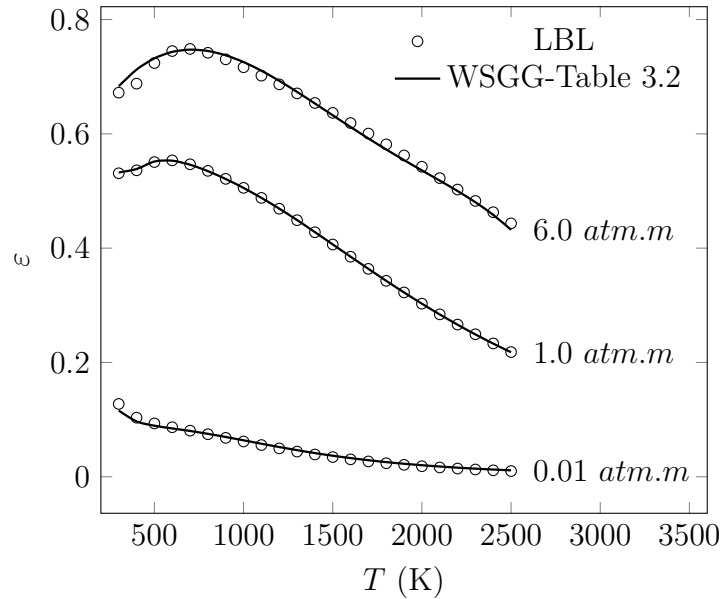


Figure 5.8 – Comparison between emittances for MR= 2 and $p_a = 1.0 \text{ atm.}$

5.1.2 Results for the Radiative Heat Source and Heat Flux

The following are the results obtained when using the correlations presented at Tables 3.1, and 3.2. The results obtained were named to its respective MR as WSGG-Table 3.1, or WSGG-Table 3.2 and were compared with the results obtained by Dorigon et al. [2013], which were labeled as Dorigon et al.

For the first case tested, p1.1, the deviations obtained when using the WSGG correlations of this work were slightly better than those obtained when using the correlations from Dorigon et al. The maximum and average deviations for the radiative heat source were 1.45%, and 0.60% when using this work's correlations against 2.51%, and 0.87% when using the correlations from Dorigon et al. Figure 5.9 shows both correlations behavior for the radiative heat source.

The maximum and average deviations for the radiative heat flux were 0.97%, and 0.59% when using this work's correlations against 1.92%, and 1.14% when using the coefficients from Dorigon et al. Figure 5.10 shows both correlations behavior for the radiative heat flux.

The second case, p1.2, has two peaks for the maximum temperature within the medium. The deviations for the maximum radiative heat source when using this work's coefficients were 3.00%, and 3.79% when using the correlations from Dorigon et al. The

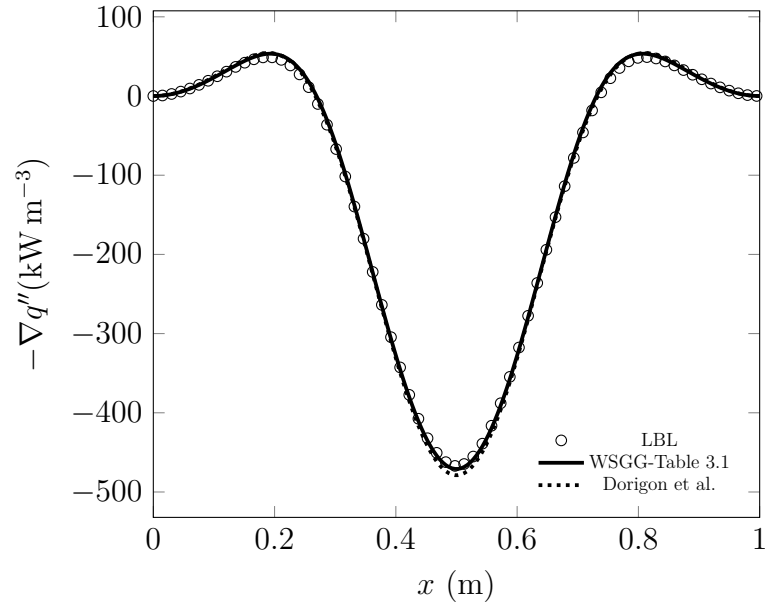


Figure 5.9 – Comparison of results for the radiative heat source for Case p1.1, where $T(x) = [400 K + (1400 K)\sin^2(\pi x/X)]$, $Y_{CO_2} = 0.1\sin^2(\pi x/X)$, and $Y_{H_2O}(x) = Y_{CO_2}(x)$.

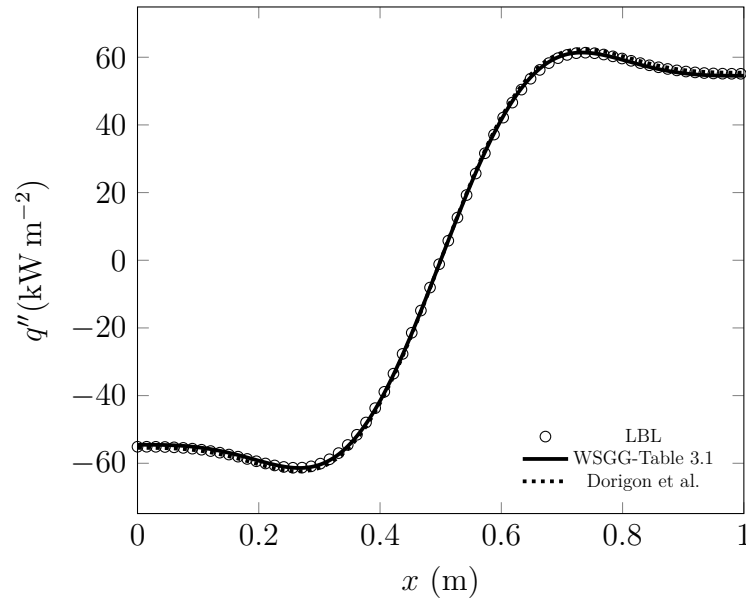


Figure 5.10 – Comparison of results for the radiative heat flux for Case p1.1, where $T(x) = [400 K + (1400 K)\sin^2(\pi x/X)]$, $Y_{CO_2} = 0.1\sin^2(\pi x/X)$, and $Y_{H_2O}(x) = Y_{CO_2}(x)$.

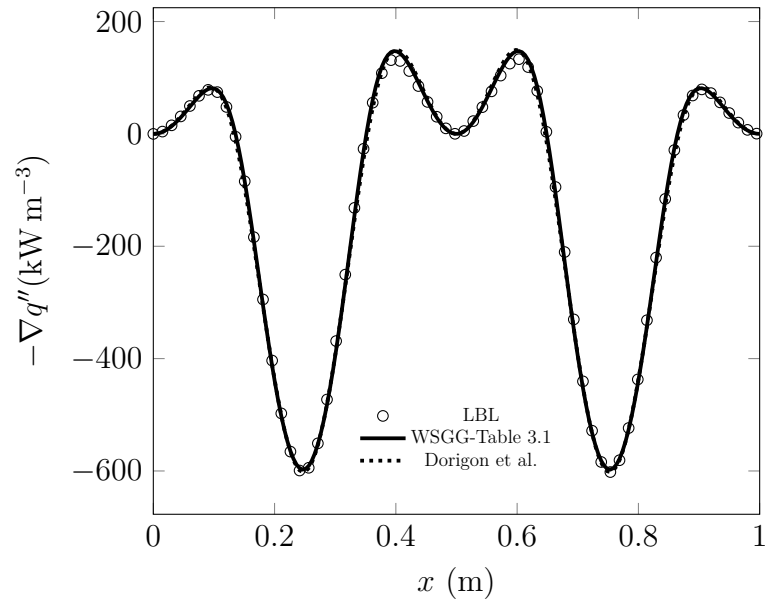


Figure 5.11 – Comparison of results for the radiative heat source for Case p1.2, where

$$T(x) = [400 \text{ K} + (1400 \text{ K})\sin^2(2\pi x/X)], \quad Y_{CO_2} = 0.1\sin^2(2\pi x/X), \quad \text{and}$$

$$Y_{H_2O}(x) = Y_{CO_2}(x).$$

average radiative heat source deviations were 0.94% and 1.22% for the correlations from this work and those presented by Dorigon et al., respectively. Figure 5.11 shows the plot between the two WSGG correlations and the LBL integration for Case p1.2 for the radiative heat source.

On the other hand, the deviations for the maximum radiative heat flux when using this work's correlations were 1.40%, and 2.11% when using the correlations from Dorigon et al. The average radiative heat flux deviations were 0.42% and 1.12% for the correlations from this work and those presented by Dorigon et al., respectively. Figure 5.12 illustrates the performance of both WSGG models against the benchmark LBL integration for the radiative heat flux.

In the last case proposed in the work by Dorigon et al. for $MR=1$, Case p1.3, the deviations were smaller when using the correlations provided by Dorigon et al. The maximum and average radiative heat source deviations when using this work's correlations were 2.93%, and 0.90%. Those obtained from the usage of the correlations presented by Dorigon were 2.68%, and 0.82%. Figure 5.13 plots the results obtained for the Case p1.3 for the radiative heat source.

Likewise, the maximum and average radiative heat flux deviations when using

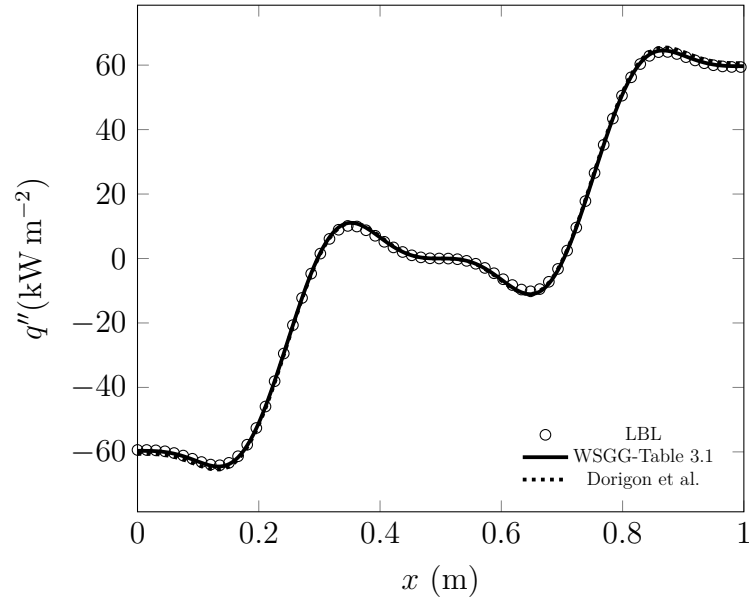


Figure 5.12 – Comparison of results for the radiative heat flux for Case p1.2, where

$$T(x) = [400 \text{ K} + (1400 \text{ K})\sin^2(2\pi x/X)], Y_{CO_2} = 0.1\sin^2(2\pi x/X), \text{ and}$$

$$Y_{H_2O}(x) = Y_{CO_2}(x).$$

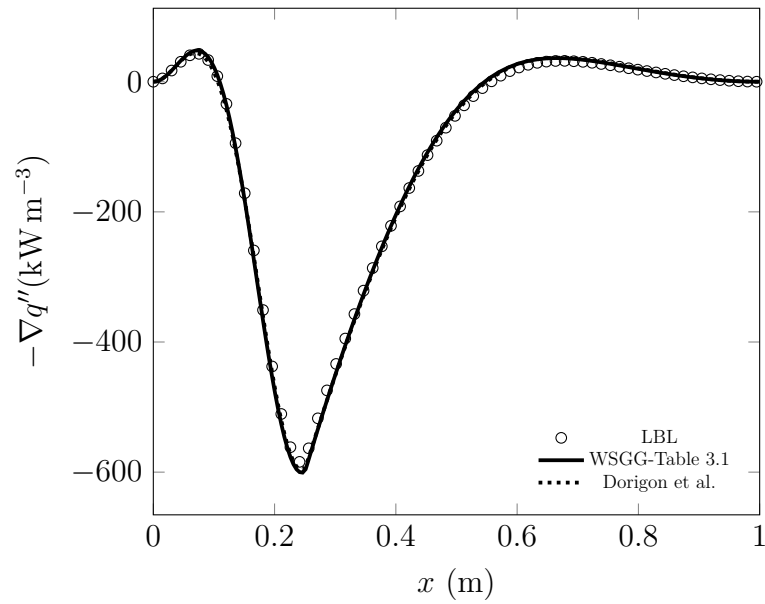


Figure 5.13 – Comparison of results for the radiative heat source for Case p1.3.

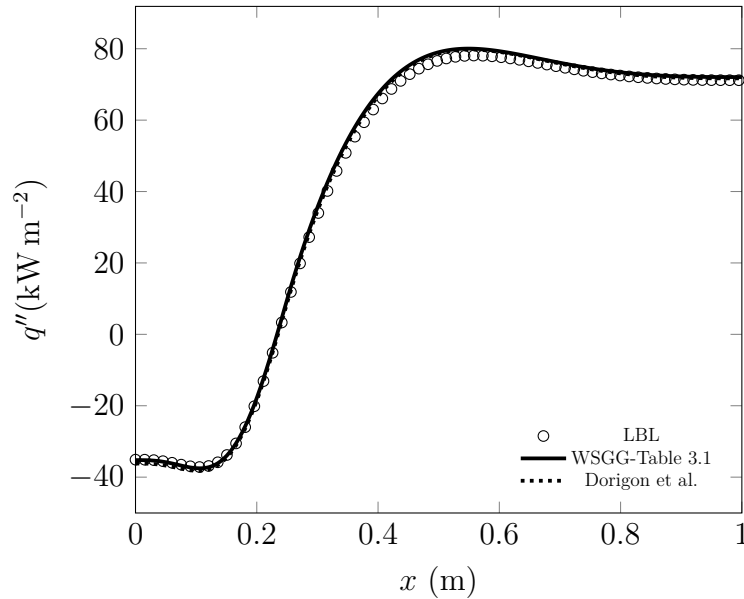


Figure 5.14 – Comparison of results for the radiative heat flux for Case p1.3.

this work's correlations were 3.49%, and 1.67%. Those obtained from the usage of the correlations presented by Dorigon were 2.60%, and 1.36%. Figure 5.14 plots the results obtained for the radiative heat flux for Case p1.3.

For the first case proposed by this work, p1.4, the WSGG correlations from this work had a slightly better performance when compared with those from work done by Dorigon et al. The maximum radiative heat source deviation obtained when using this work's WSGG correlations was 2.32%, against 2.40% that was obtained when using the correlations from the work by Dorigon et al. The average radiative heat source followed the same behavior, with 0.98% against 1.16%. Figure 5.15 shows the results obtained for the radiative heat source for Case p1.4.

Conversely, the results obtained for the maximum, 3.03%, and average, 1.55%, radiative heat flux were significantly better when compared with the deviations obtained when using the correlations presented by Dorigon et al., namely 4.61%, and 3.18%. Figure 5.16 shows the behaviors of the WSGG correlations when compared with the values obtained using the LBL integration for the radiative heat flux.

The last case for a $MR=1$, Case p1.5, has also, like Case p1.2, two peaks for the maximum temperature; however, the partial pressures for the species were higher. The results for the maximum and average deviations for the radiative heat source obtained using this work's correlations were respectively 3.94%, and 1.84%. Those yielded from

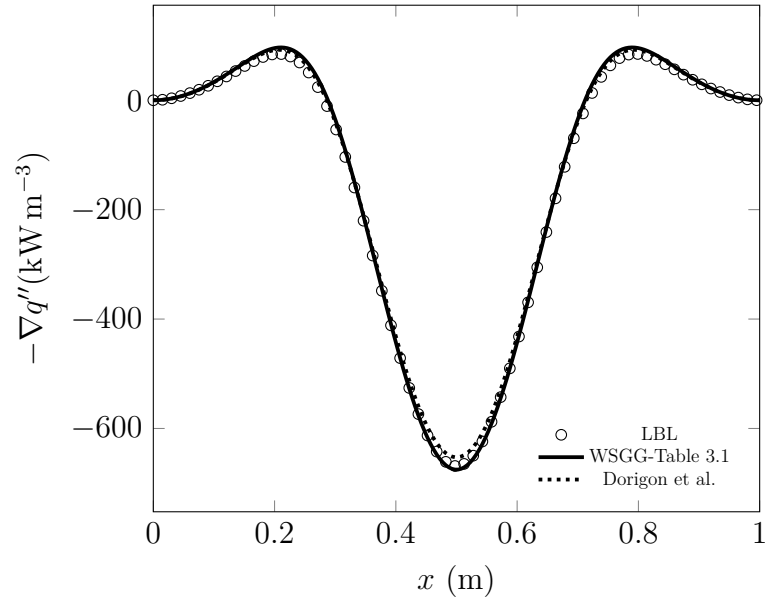


Figure 5.15 – Comparison of results for the radiative heat source for Case p1.4, where $T(x) = [300 K + (1500 K)\sin^2(\pi x/X)]$, $Y_{CO_2} = 0.4\sin^2(\pi x/X)$, and $Y_{H_2O}(x) = Y_{CO_2}(x)$.

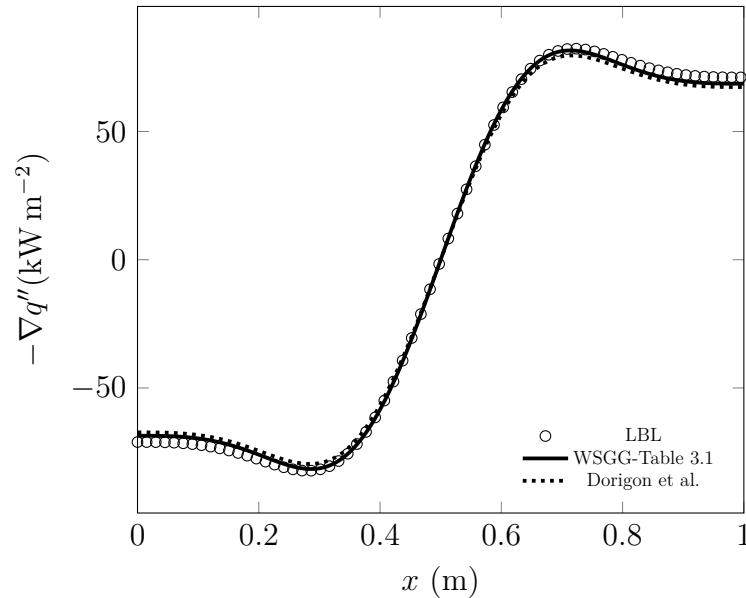


Figure 5.16 – Comparison of results for the radiative heat flux for Case p1.4, where $T(x) = [300 K + (1500 K)\sin^2(\pi x/X)]$, $Y_{CO_2} = 0.4\sin^2(\pi x/X)$, and $Y_{H_2O}(x) = Y_{CO_2}(x)$.

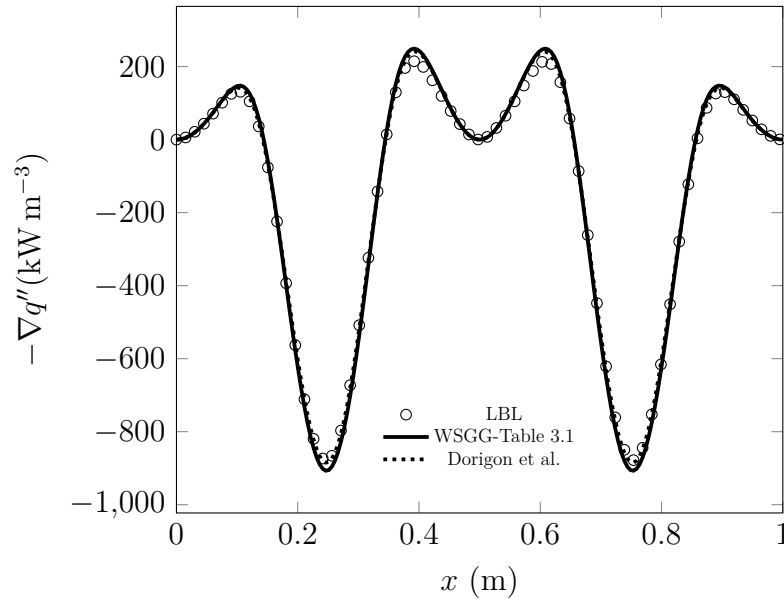


Figure 5.17 – Comparison of results for the radiative heat source for Case p1.5, where

$$T(x) = [300 \text{ K} + (1500 \text{ K})\sin^2(2\pi x/X)], Y_{CO_2} = 0.4\sin^2(2\pi x/X), \text{ and}$$

$$Y_{H_2O}(x) = Y_{CO_2}(x).$$

the usage of the correlations presented by Dorigon et al. were respectively 3.22%, and 0.93%. These results indicate that the correlations from Dorigon et al. performed better regarding the radiative heat source for the Case p1.5. Figure 5.17 shows the results for the radiative heat source for Case p1.5.

The results for the maximum and average deviations for the radiative heat flux obtained using this work's correlations were respectively 3.08%, and 1.07%. Those yielded from the usage of the correlations presented by Dorigon et al. were respectively 2.61%, and 1.65%, which indicates a better performance for this work correlations for the average radiative heat flux deviations. Contrariwise, the correlations from Dorigon et al. performed better for the maximum radiative heat flux. Figure 5.18 shows the plots for the radiative heat flux for Case p1.5.

The next five cases are those for a MR= 2. The temperature profiles, and molar concentration for CO₂, as stated before, were the same as the former five cases. In comparison with the cases with MR= 1, the cases with MR= 2 performed similarly.

In the first case considering a MR= 2, case p2.1, the maximum and average deviations for the radiative heat source when using the correlations from Table 3.2 were respectively 1.57%, and 0.73%. The results obtained when using the correlations from

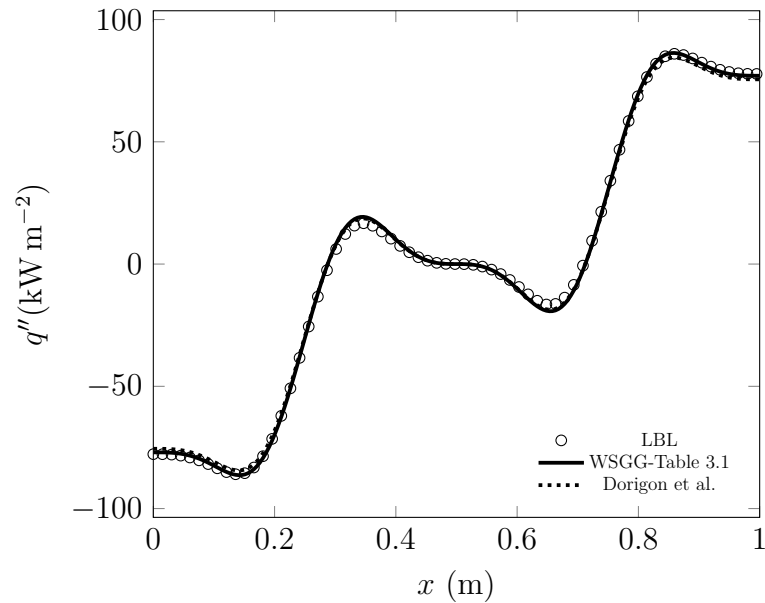


Figure 5.18 – Comparison of results for the radiative heat flux for Case p1.5, where

$$T(x) = [300 \text{ K} + (1500 \text{ K})\sin^2(2\pi x/X)], Y_{CO_2} = 0.4\sin^2(2\pi x/X), \text{ and}$$

$$Y_{H_2O}(x) = Y_{CO_2}(x)$$

Dorigon et al. work were 1.14% for the maximum radiative heat source, and 0.67% for the average radiative heat source, which indicated a slightly better performance for the coefficients presented by Dorigon et al. Figure 5.19 shows the behavior of the WSGG correlations and LBL integrations for the radiative heat source for Case 2.1.

Regarding the deviations for the radiative heat flux for the Case p2.1, the maximum and average results when using Table 3.2 were 1.09%, and 0.62%, respectively. These results were slightly better than those obtained when using Dorigon et al. correlations, which resulted in 1.60%, and 0.98% for the maximum and average deviations. Next, Figure 5.20 shows the plots of the respective results when using the different WSGG models, and LBL integration for the radiative heat flux for the Case p2.1.

For the Case p2.2, the correlations presented by this work performed a little better than those proposed by Dorigon et al. for both radiative heat source and radiative heat flux. Concerning the radiative heat source, the maximum and average deviations when using the correlations proposed by this work were 2.60%, and 0.93% against 2.63%, and 1.07% of those obtained when using the correlations presented by Dorigon et al. Following, Figure 5.21 shows the behavior of the WSGG correlations and LBL integrations for the radiative heat source for Case p2.2.

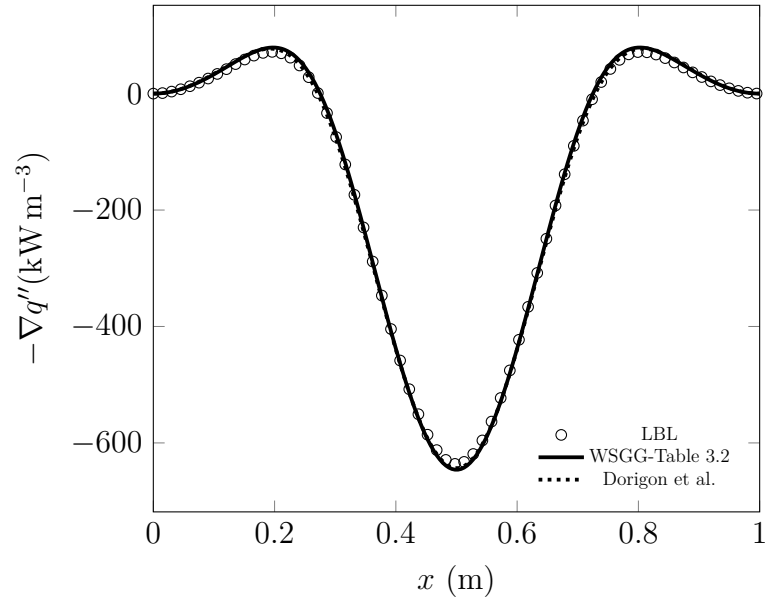


Figure 5.19 – Comparison of results for the radiative heat source for Case p2.1, where

$$T(x) = [400 K + (1400 K)\sin^2(\pi x/X)], Y_{CO_2} = 0.1\sin^2(\pi x/X), \text{ and}$$

$$Y_{H_2O}(x) = 2 \times Y_{CO_2}(x).$$

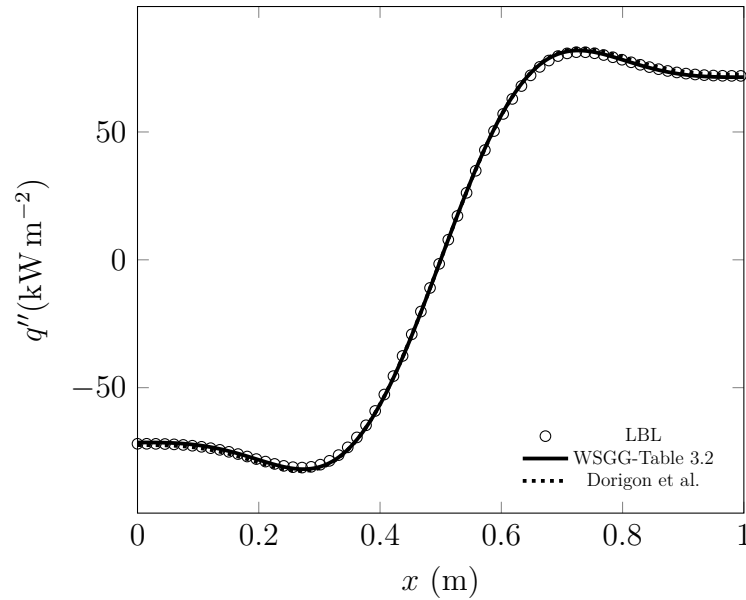


Figure 5.20 – Comparison of results for the radiative heat flux for Case p2.1, where

$$T(x) = [400 K + (1400 K)\sin^2(\pi x/X)], Y_{CO_2} = 0.1\sin^2(\pi x/X), \text{ and}$$

$$Y_{H_2O}(x) = 2 \times Y_{CO_2}(x).$$

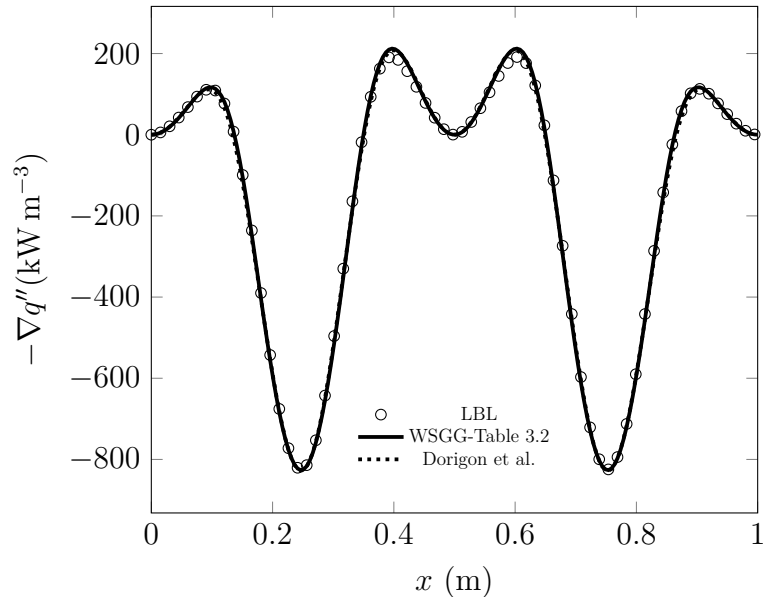


Figure 5.21 – Comparison of results for the radiative heat source for Case p2.2, where

$$T(x) = [400 \text{ K} + (1400 \text{ K})\sin^2(2\pi x/X)], \quad Y_{CO_2} = 0.1\sin^2(2\pi x/X), \quad \text{and}$$

$$Y_{H_2O}(x) = 2 \times Y_{CO_2}(x).$$

In respect of the deviations for the radiative heat flux for the Case p2.2, the maximum and average results when using Table 3.2 were 1.56%, and 0.68%, respectively. These results were slightly better than those obtained when using Dorigon et al. correlations, which resulted in 2.30%, and 1.09% for the maximum and average deviations. Figure 5.22 shows the plots of the respective results when using the different WSGG models and LBL integration for the radiative heat flux for the Case p2.2.

For the Case p2.3, the deviations were once again smaller when using the correlations provided by Dorigon et al. The maximum and average radiative heat source deviations when using this work's correlations were 3.71%, and 1.00%. Those obtained from using the correlations presented by Dorigon et al. were 2.27%, and 0.65%. Figure 5.23 plots the results obtained for the Case p2.3 for the radiative heat source.

For the radiative heat flux, the results obtained when using the correlations presented by this work were 4.25%, and 2.11% for the maximum and average deviations, whereas the results obtained when using the WSGG correlations reported by Dorigon et al. were 2.24%, and 1.22% for the maximum, and average deviations. Figure 5.24 depicts the results obtained for the radiative heat flux for the Case p2.3.

The first case proposed by this work for a medium with a MR= 2, Case p2.4,

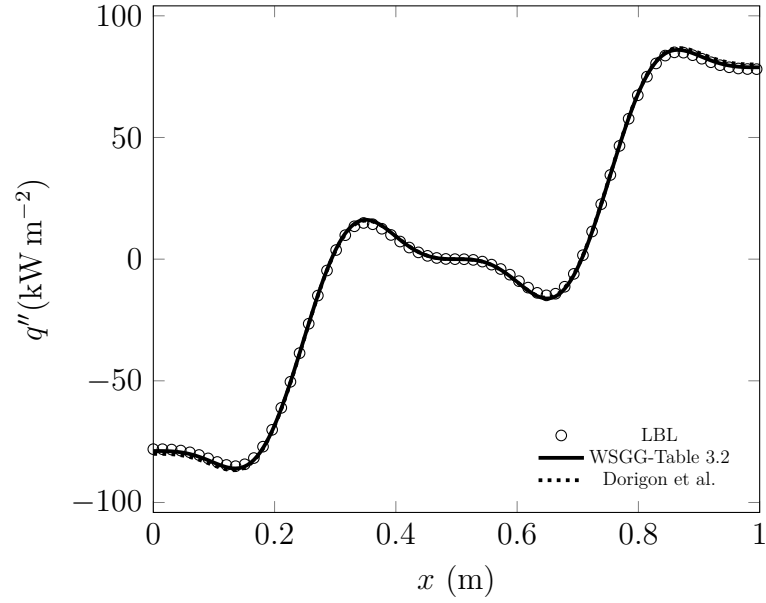


Figure 5.22 – Comparison of results for the radiative heat flux for Case p2.2, where

$$T(x) = [400 \text{ K} + (1400 \text{ K})\sin^2(2\pi x/X)], Y_{CO_2} = 0.1\sin^2(2\pi x/X), \text{ and}$$

$$Y_{H_2O}(x) = 2 \times Y_{CO_2}(x).$$

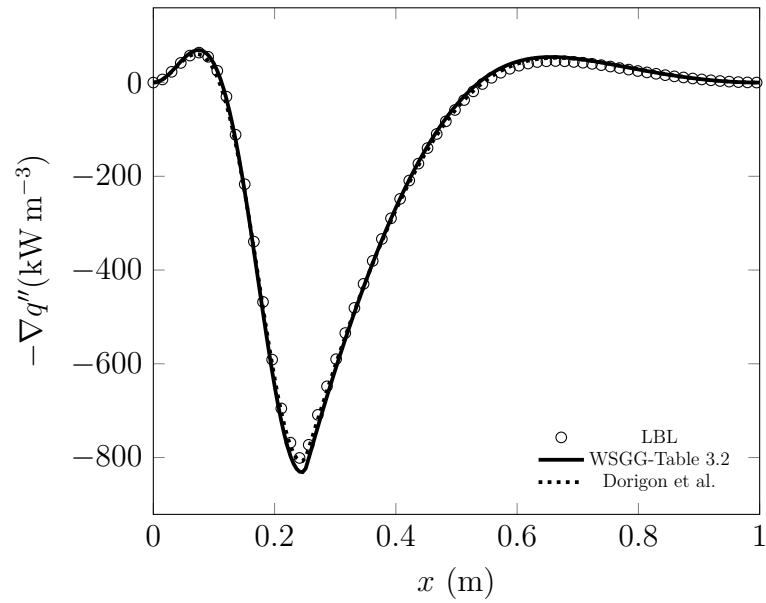


Figure 5.23 – Comparison of results for the radiative heat source for Case p2.3.

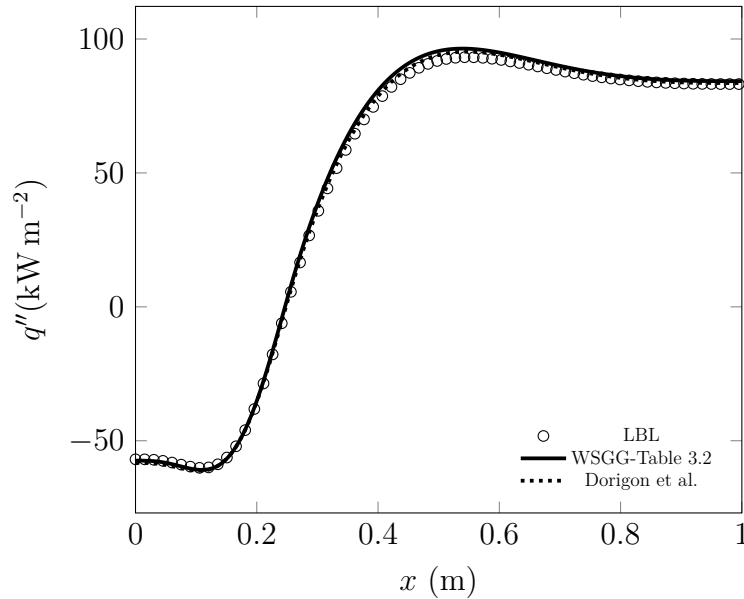


Figure 5.24 – Comparison of results for the radiative heat flux for Case p2.3.

followed the same temperature, and CO_2 shape profiles as Case p1.4. The deviations regarding the radiative heat source when using the correlations proposed by this work were 1.96%, maximum, and 0.79%, average. Figure 5.25 shows the behavior of the WSGG correlations and the LBL integration for the radiative heat source for Case p2.4.

The maximum and average deviations for the radiative heat flux for the Case p2.4 when using the correlations presented by this work were respectively 2.85%, and 1.33%, against 2.72%, and 1.70% for those obtained when using the correlations proposed by Dorigon et al. Note that for the radiative heat flux, only the average deviation was slightly smaller when using the correlations from this work. Figure 5.26 shows the results obtained in comparison with an LBL integration for the radiative heat flux for Case p2.4.

Finally, the last profile for the scenario with a varying partial pressure, Case p2.5. In this case, the maximum and average deviations for the radiative heat source when using the correlations from Table 3.2 were respectively 3.74%, and 1.46%. Those obtained when using the correlations from the Dorigon et al. work were 3.00%, maximum, and 0.74%, average. The following picture shows the plots for the two WSGG models and the LBL integrations for the radiative heat source for Case p2.5.

At last, the deviations when using the correlations presented by this work for the radiative heat flux for Case p2.5 were 2.82%, maximum, and 0.91%, average. The results provided by the correlations proposed by Dorigon et al. were a little better, 1.92% for

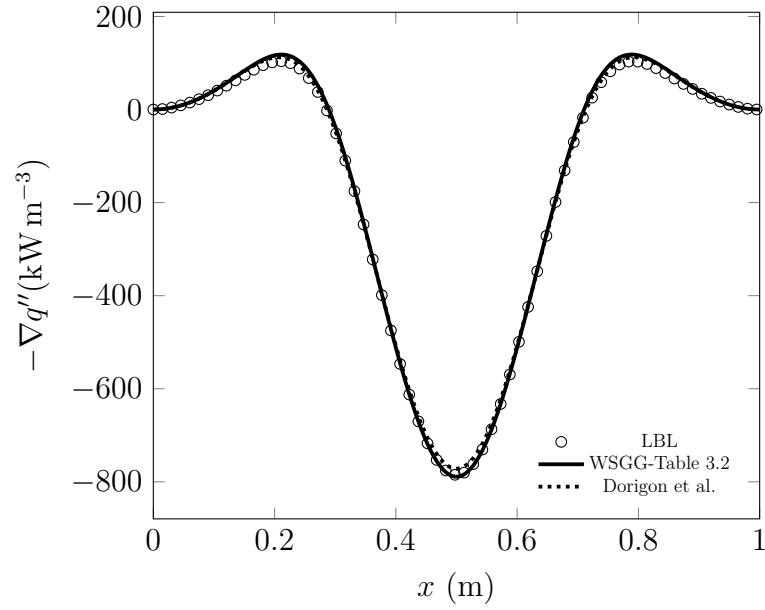


Figure 5.25 – Comparison of results for the radiative heat source for Case p2.4, where

$$T(x) = [300 \text{ K} + (1500 \text{ K})\sin^2(\pi x/X)], Y_{CO_2} = 0.3\sin^2(\pi x/X), \text{ and}$$

$$Y_{H_2O}(x) = 2 \times Y_{CO_2}(x).$$

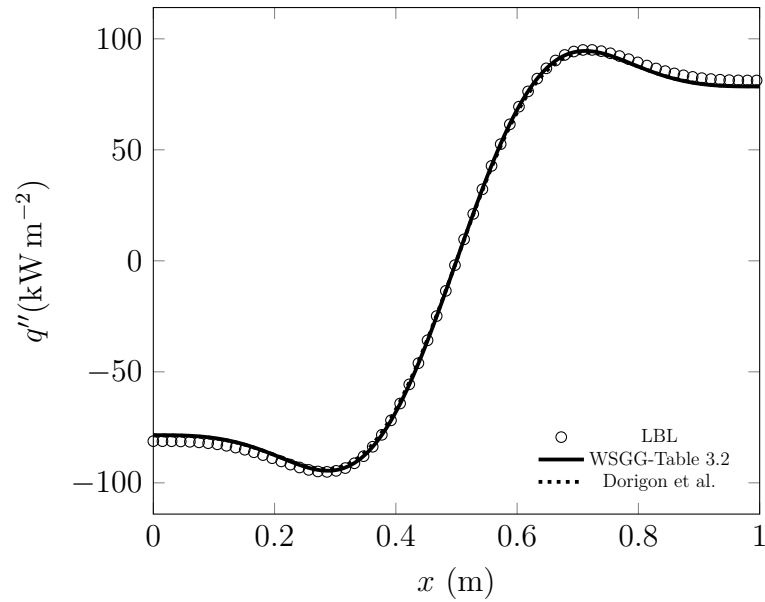


Figure 5.26 – Comparison of results for the radiative heat flux for Case p2.4, where

$$T(x) = [300 \text{ K} + (1500 \text{ K})\sin^2(\pi x/X)], Y_{CO_2} = 0.3\sin^2(\pi x/X), \text{ and}$$

$$Y_{H_2O}(x) = 2 \times Y_{CO_2}(x).$$

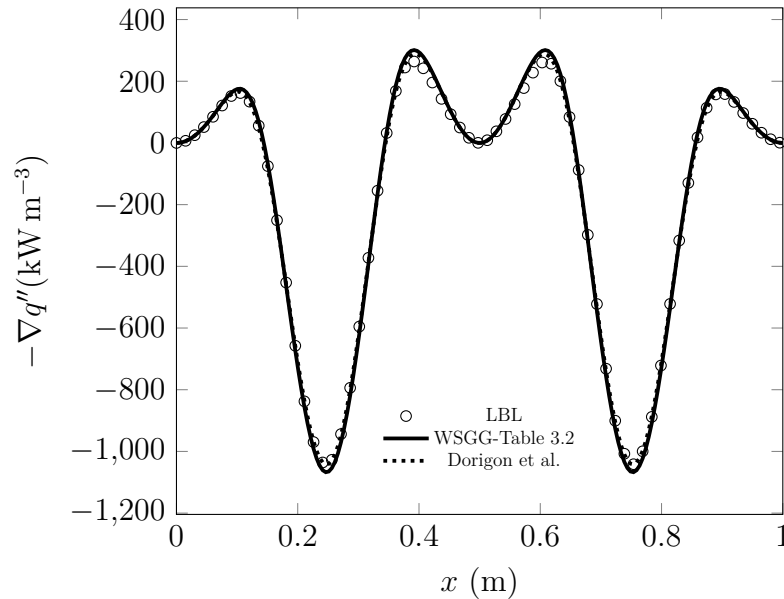


Figure 5.27 – Comparison of results for the radiative heat source for Case p2.5, where

$$T(x) = [300 K + (1500 K)\sin^2(2\pi x/X)], Y_{CO_2} = 0.3\sin^2(2\pi x/X), \text{ and}$$

$$Y_{H_2O}(x) = 2 \times Y_{CO_2}(x).$$

the maximum deviation, and 0.82% for the average. Figure 5.28 depicts the behaviors of the three models along the proposed domain.

As a way of turning the reading and understanding of this work easier, the maximum and average (in parenthesis) deviations are presented in Table 5.1. Note that the results for this work are under the columns named either WSGG-Table 3.1, or WSGG-Table 3.2. The results were obtained using Equations (4.20a), and (4.20b), for the radiative heat flux, and radiative heat source, respectively. Also, note that at the end of the table is two extra rows for the mean value of all maximum and average deviations of the two WSGG models used on the scenario with a varying partial pressure.

Other authors' correlations could have been compared, however, the coefficients proposed by Dorigon et al. [2013] have shown a better accuracy when it comes to WSGG correlations for open atmosphere combustions. This way, putting other results would not contribute considerably for this work, and in truth would only turn the plots more difficult to read from, which would be understandable if the results being compared had a great relevance.

Note that, even though the partial pressure contributed to a change in the absorption coefficient, well pronounced on the total emittance, accounting for the partial

Table 5.1 – Maximum and (Average) Deviations from LBL calculations for cases using correlations from Tables 3.1 and 3.2, in percentage (%).

Case	Heat Source		Heat Flux	
	WSGG-Table 3.1	Dorigon et al.	WSGG-Table 3.1	Dorigon et al.
p1.1	1.45	2.51	0.97	1.92
	(0.60)	(0.87)	(0.59)	(1.14)
p1.2	3.00	3.79	1.40	2.11
	(0.94)	(1.22)	(0.42)	(1.12)
p1.3	2.93	2.68	3.49	2.60
	(0.90)	(0.82)	(1.67)	(1.36)
p1.4	2.32	2.40	3.03	4.61
	(0.98)	(1.16)	(1.55)	(3.18)
p1.5	3.94	3.22	3.08	2.61
	(1.84)	(0.93)	(1.07)	(1.65)
	WSGG-Table 3.2	Dorigon et al.	WSGG-Table 3.2	Dorigon et al.
p2.1	1.57	1.14	1.09	1.60
	(0.73)	(0.67)	(0.62)	(0.98)
p2.2	2.60	2.63	1.56	2.30
	(0.93)	(1.07)	(0.68)	(1.09)
p2.3	3.71	2.27	4.25	2.24
	(1.00)	(0.65)	(2.11)	(1.22)
p2.4	1.96	1.70	2.85	2.72
	(0.79)	(1.67)	(1.33)	(1.70)
p2.5	3.74	3.00	2.82	1.92
	(1.46)	(0.74)	(0.91)	(0.82)
Mean	2.72	2.53	2.45	2.46
	(1.02)	(0.98)	(1.10)	(1.43)

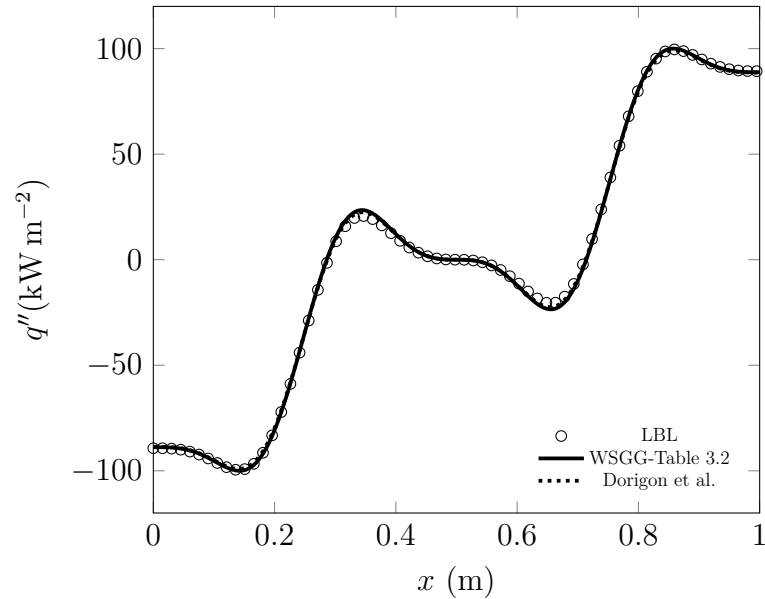


Figure 5.28 – Comparison of results for the radiative heat flux for Case p2.5, where

$$T(x) = [300 \text{ K} + (1500 \text{ K})\sin^2(2\pi x/X)], \quad Y_{CO_2} = 0.3\sin^2(2\pi x/X), \quad \text{and}$$

$$Y_{H_2O}(x) = 2 \times Y_{CO_2}(x).$$

pressure variations in the WSGG model did not significantly increase the accuracy of the method when solving the radiative heat source and flux. These findings indicate that the dependence of the WSGG model on the partial pressure is small insofar the MR of the model is the same as the medium.

5.2 Results for Varying MR

5.2.1 Results for the Total Emittance

The amount of possible total emittances plots for the case with a varying MR is large, therefore, it was chosen only three MR values for being shown. Figure 5.29 shows the fitting for emittances for a MR= 0.5, and Figure 5.30 shows the fitted emittances for a MR= 1 for three different pressure-path-length.

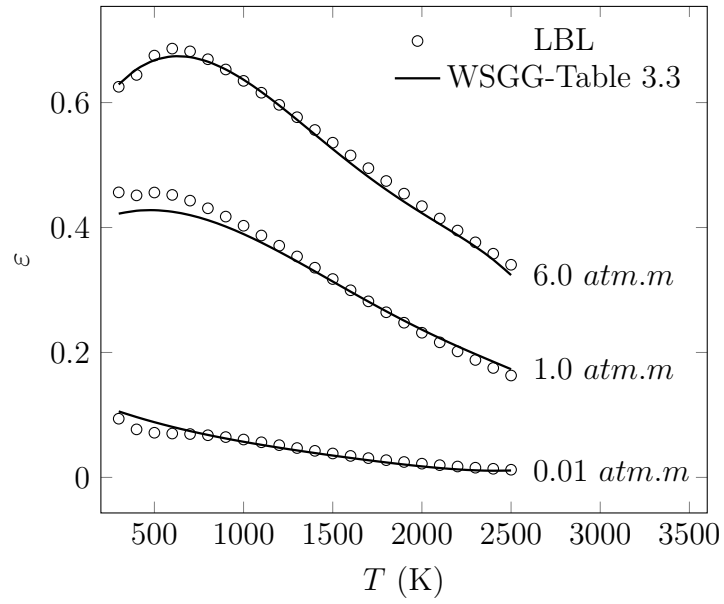


Figure 5.29 – Comparison between emittances for MR= 0.5.

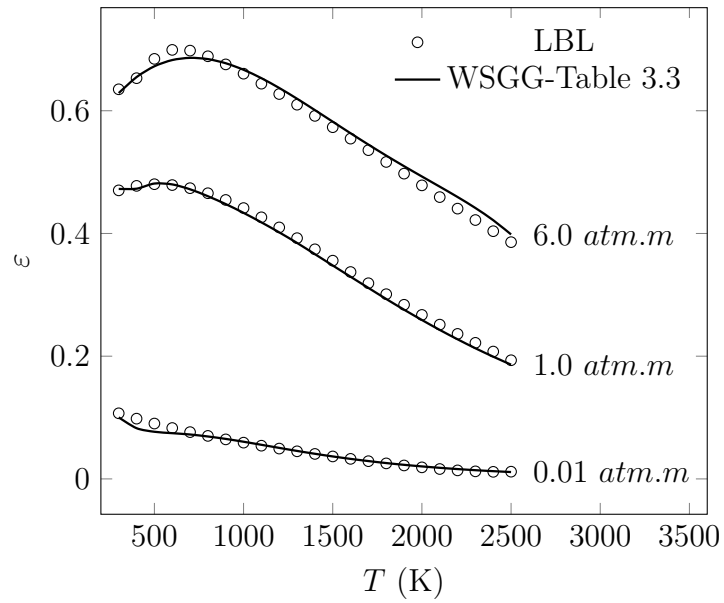


Figure 5.30 – Comparison between emittances for MR= 1.

Finally, there is presented a fitting for emittances where the MR is set to be equal to 2.

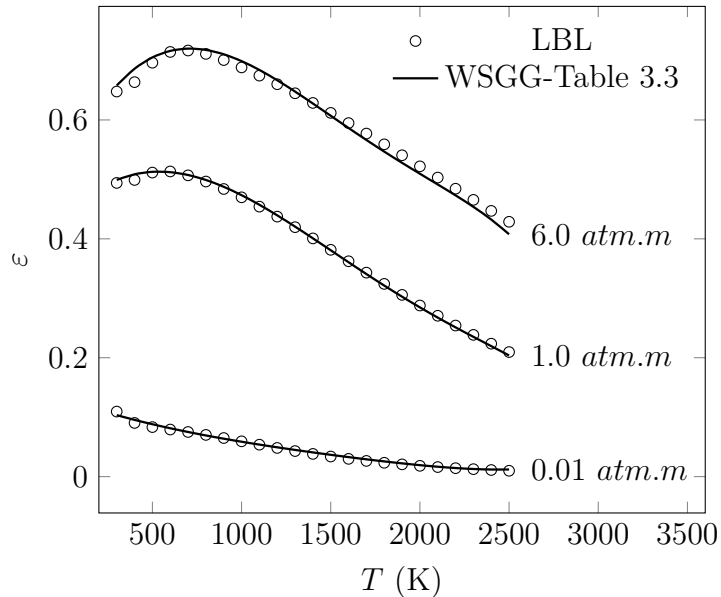


Figure 5.31 – Comparison between emittances for MR= 2.

5.2.2 Results for the Radiative Heat Source and Heat Flux

The results of this study are denoted as WSSG-Table 3.3, and WSSG-Table 3.4, while those of Kangwanpongpan et al. [2012], and Bordbar et al. [2014] are denoted as Kang. et al., and Bordbar et al., respectively. It is noteworthy to point out that the results of radiative heat source in the two volumes close to both walls were not considered when obtaining the maximum, and average deviations for Cases m1.1 to m3.5. Apparently, the discontinuity between the domain temperature and walls greatly disturbs the accuracy of all correlations. It is thought that, since the radiative heat source is the divergent of the heat flux, the abrupt variation caused by the discontinuity makes the deviations to become non-meaningful.

It is important to mention that, differently of the author-to-author comparisons made at the scenario with varying partial pressures, in this scenario the comparisons of author-to-author numbers were not done for all the cases; the comparisons were made when most important observations were available. Note that the first two profiles, which have both a homogeneous temperature, were not depicted along this work, so that it is possible to focus on the more complex profiles.

When using the correlation of WSGG-Table 3.3, the deviations regarding the radiative heat source for the Case m1.1 were no greater than 4.14%, with an average value

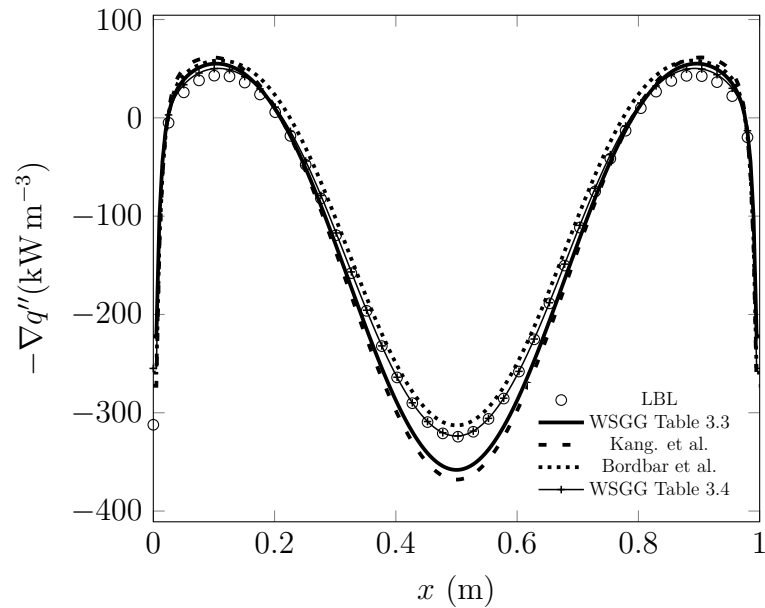


Figure 5.32 – Comparison of results for the radiative heat source for Case m2.1, where $T(x) = [1400 K - (400 K)\cos(2\pi x/X)]$, $Y_{CO_2} = 0.8$, and $Y_{H_2O} = 0.1$.

of 0.73%. For the Case m1.2, the maximum radiative heat source deviation was 5.33%, and the average value was 0.36%. When it comes to the heat flux, the maximum value obtained was of 9.26%, Case m1.1, and 2.35%, Case m1.2. The average values for the heat flux were 3.40% for Case m1.1, and 1.09% for Case m1.2. As expected, the results obtained from WSGG-Table 3.4 were better than those of WSGG-Table 3.3, both in radiative heat source and radiative heat flux.

As pointed before, Cases m2.1, and m2.2 have a constant MR, being homogeneous in its molar concentrations, but have an inhomogeneous temperature profile. For Case m2.1, the maximum value for the radiative heat source deviation when using WSGG-Table 3.3 was 8.87%, and the average value was 3.85%. Correlations from WSGG-Table 3.4 presented maximum values for radiative heat source deviation of 2.17%, and 0.96% for the average radiative heat source deviation. For the Case m2.1, the lowest deviations regarding both radiative heat source, and radiative heat flux were obtained when using the correlations from WSGG-Table 3.4. Figure 5.32 shows the plots for the four WSGG models and the LBL integration for the radiative heat source for Case m2.1.

When using correlations from Table 3.3, the maximum and average deviations for the radiative heat flux were 9.95% and 7.38%. On the other hand, the maximum and average deviations for the radiative heat flux when using Table 3.4 were 3.92%, and 1.01%.

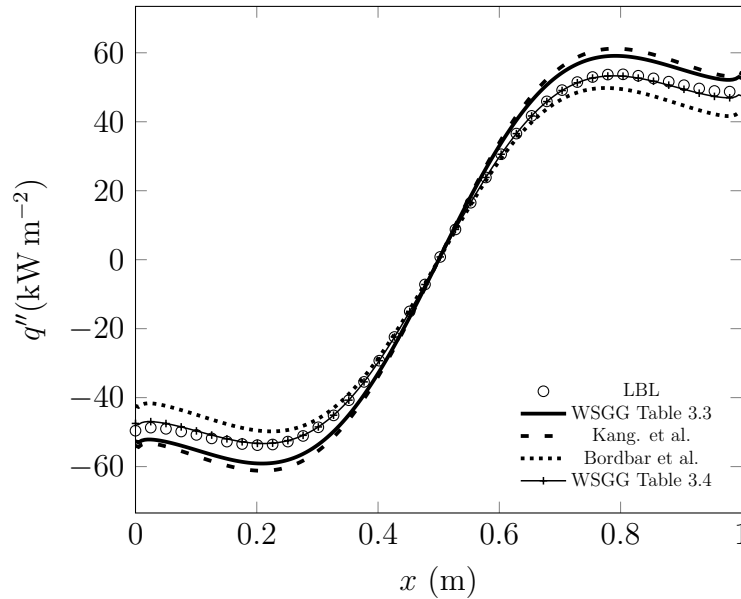


Figure 5.33 – Comparison of results for the radiative heat flux for Case m2.1, where

$$T(x) = [1400 \text{ K} - (400 \text{ K})\cos(2\pi x/X)], Y_{CO_2} = 0.8, \text{ and } Y_{H_2O} = 0.1.$$

Figure 5.33 shows the comparison between the WSGG models and the LBL integration for Case m2.1.

For the Case m2.2 the maximum and average deviations for the radiative heat source when using the coefficients from Table 3.3 were 3.98%, and 1.37%, respectively. Correlations from Table 3.4 presented a maximum value for radiative heat source of 4.24%. The mean value for the radiative heat source was 1.26%, which was slightly smaller than the average deviation obtained when using the correlations from Table 3.3. For this case, the maximum deviations were smaller when using the correlations presented by Bordbar et al. Conversely, for the average deviation, the lowest results were obtained using the correlations presented by this work. Figure 5.34 shows the curves for the radiative heat source for Case m2.2.

The deviations for the radiative heat flux for Case m2.2 presented a smaller maximum value when using correlations from Kang. et al., and a smaller average deviation when using the correlations from Table 3.4. The deviations for the maximum and average radiative heat flux when using Table 3.4 were 3.95%, and 0.70%. For Table 3.3 the results were higher, 4.29%, maximum, and 1.93%. Figure 5.35 shows the results for the radiative heat flux for Case m2.2.

The mean deviations obtained for Case m3.1, when using Table 3.3 were 3.71%,

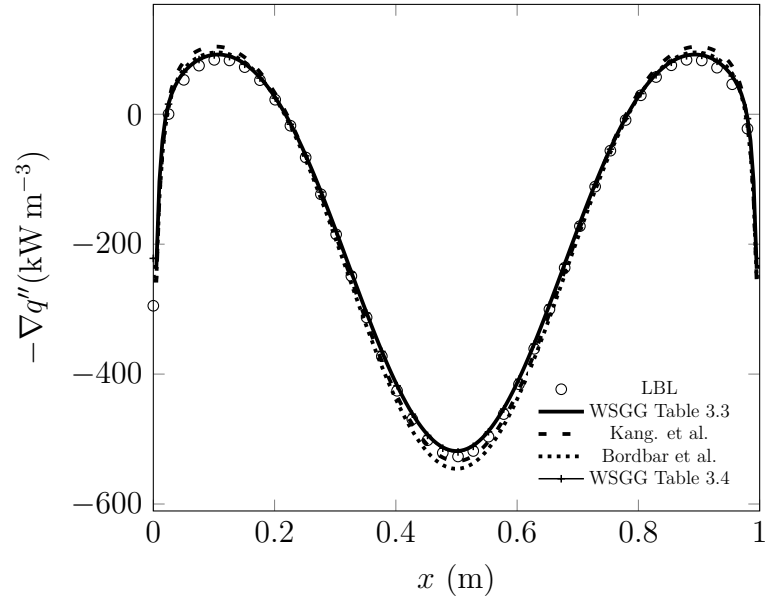


Figure 5.34 – Comparison of results for the radiative heat source for Case m2.2, where $T(x) = [1400 K - (400 K)\cos(2\pi x/X)]$, $Y_{CO_2} = 0.48$, and $Y_{H_2O} = 0.48$.

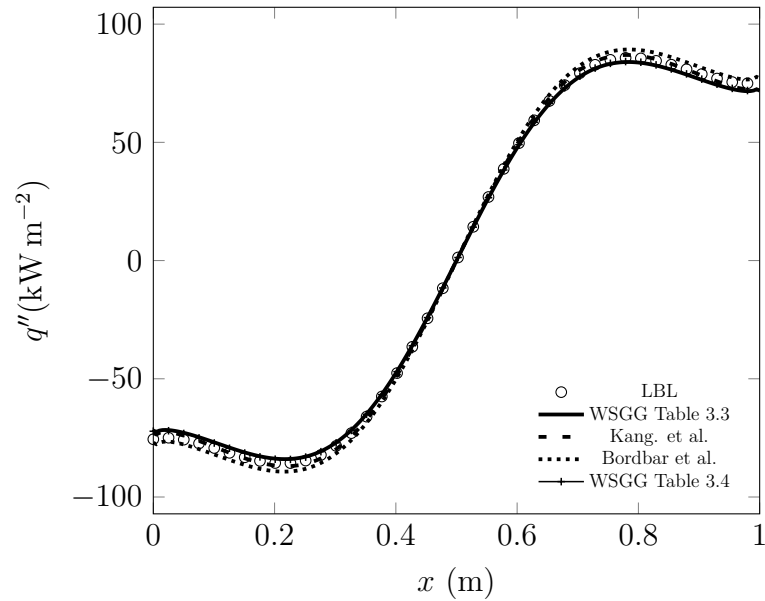


Figure 5.35 – Comparison of results for the radiative heat flux for Case m2.2, where $T(x) = [1400 K - (400 K)\cos(2\pi x/X)]$, $Y_{CO_2} = 0.48$, and $Y_{H_2O} = 0.48$.

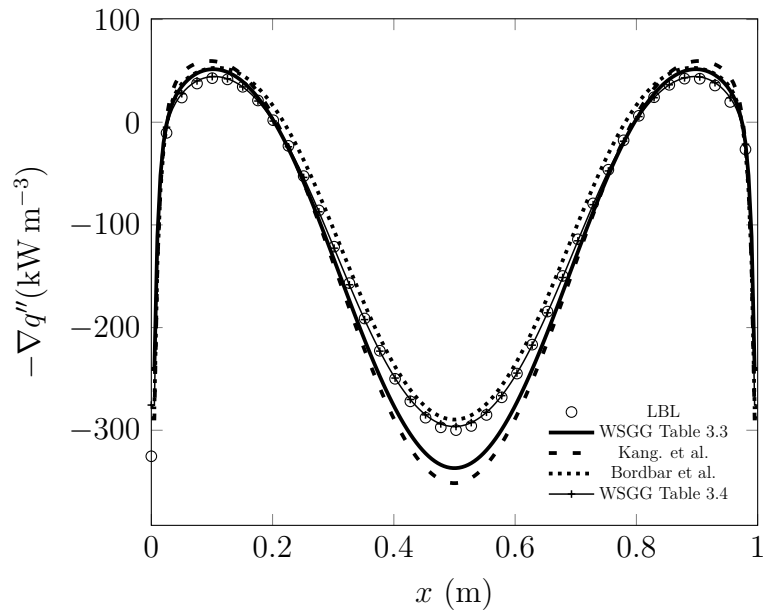


Figure 5.36 – Comparison of results for the radiative heat source for Case m3.1, where

$$T(x) = [1400 \text{ K} - (400 \text{ K})\cos(2\pi x/X)], Y_{CO_2} = 0.8, \text{ and}$$

$$Y_{H_2O}(x) = [0.12 + 0.04\cos(2\pi x/X)].$$

and 9.05%, for radiative heat source, and radiative heat flux, respectively. When it comes to the maximum deviations, the results obtained using Table 3.3 were 9.17% for the radiative heat source, and 11.78% for the radiative heat flux. The coefficients of Bordbar et al. [2014] were the ones with a better performance on this profile among the correlations accounting for a wide range of MR. However, the deviations obtained when using the Table 3.4 were way smaller than those presented by Bordbar et al. [2014]. When using the correlations from Table 3.4, the maximum values were 1.38% for radiative heat source, and 1.17% for radiative heat flux. Mean deviation values were 0.42%, and 0.21% for radiative heat source, and radiative heat flux, respectively. It is important to stress out that the correlations that are given by Table 3.4 were obtained using a narrow range of MR. However, the partial pressures of the participating media of Case m3.1 varied from 0.88 to 0.96, whereas the participating media when generating the emittances of correlations given by Table 3.4 varied from 0.1125 to 0.2. The respective curves of Case m3.1 are shown on Figures 5.36, and 5.37.

In the Case m3.2 occurs a phenomenon with a non-physical behavior when using three out of the four WSGG correlations that were tested on this work. Around the middle of the domain, where the temperature is higher, the magnitude of the radiative heat source

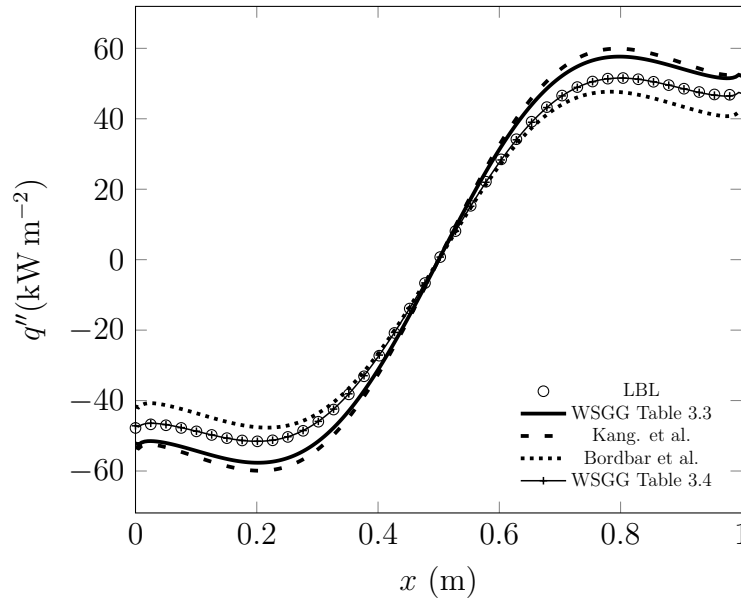


Figure 5.37 – Comparison of results for the radiative heat flux for Case m3.1, where

$$T(x) = [1400 \text{ K} - (400 \text{ K})\cos(2\pi x/X)], Y_{CO_2} = 0.8, \text{ and}$$

$$Y_{H_2O}(x) = [0.12 + 0.04\cos(2\pi x/X)].$$

decreased instead of increasing. It is believed that the MR range of the media, range of 0.57-4.0 (note that the MR range crosses the unitary mark), contributes to this behavior. Another contribution might come from the fact that the coefficients of the WSGG models do not behave well under such an extension. For Case m3.2, the best results obtained when using a wide MR range model come from Table 3.3. These results were just slightly better than those obtained by using Kang. et al., and Bordbar et al. correlations, though. Also, these results cannot be considered good results, for their deviations hover around 10% for both radiative heat source and radiative heat flux, maximum or average.

Table 3.4 correlations for $MR > 1$ were also tested on this case, although these correlations were not intended for a MR smaller than 1. The performance was as not as good as the performance presented on Case m3.1, but was still better than the performance of other correlations, and was the one that did not shows any sign of non-physical behaviors. Note that they were not great, just slightly better; however, better in this specific case did not mean good results. One may have to question the relevance of a medium with such a wide variation in the MR values. Figures 5.38, and 5.39 show the behavior of the WSGG models and the LBL integration for the radiative heat source and radiative heat flux for Case m3.2.

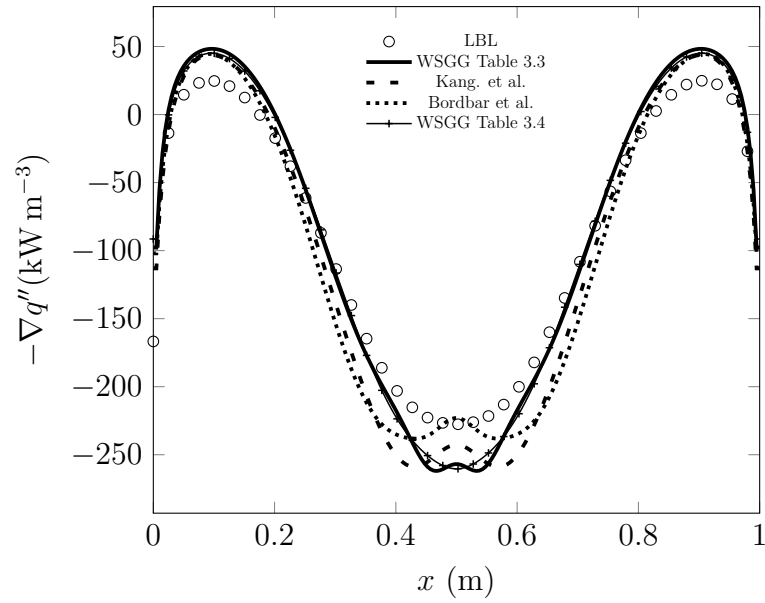


Figure 5.38 – Comparison of results for the radiative heat source for Case m3.2, where $T(x) = [1400 \text{ K} - (400 \text{ K})\cos(2\pi x/X)]$, $Y_{CO_2}(x) = [0.12 + 0.09\cos(2\pi x/X)]$, and $Y_{H_2O} = 0.12$.

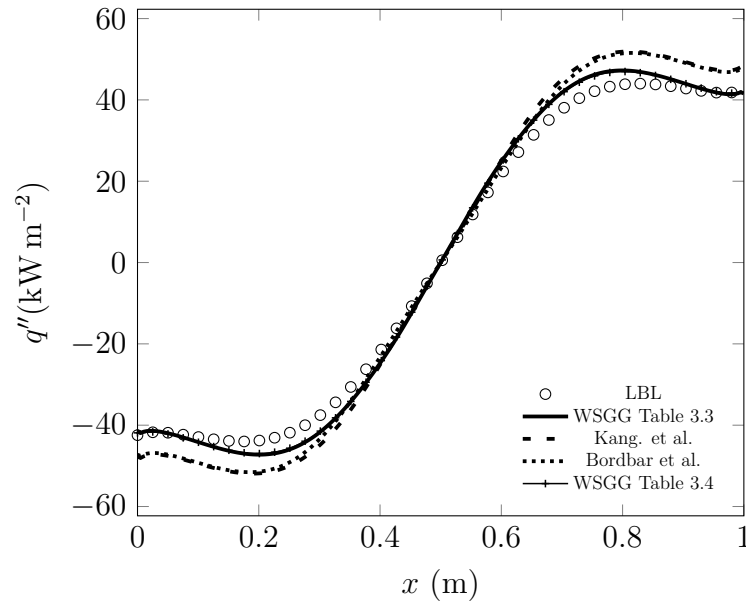


Figure 5.39 – Comparison of results for the radiative heat flux for Case m3.2, where $T(x) = [1400 \text{ K} - (400 \text{ K})\cos(2\pi x/X)]$, $Y_{CO_2}(x) = [0.12 + 0.09\cos(2\pi x/X)]$, and $Y_{H_2O} = 0.12$.

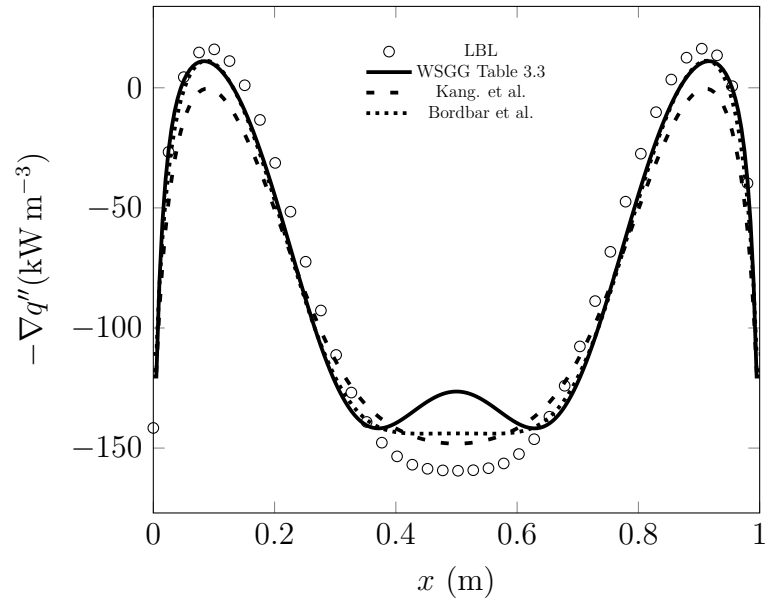


Figure 5.40 – Comparison of results for the radiative heat source for Case m3.3, where

$$T(x) = [1400 \text{ K} - (400 \text{ K})\cos(2\pi x/X)], Y_{CO_2} = 0.12, \text{ and}$$

$$Y_{H_2O}(x) = [0.12 + 0.09\cos(2\pi x/X)].$$

Cases m3.3 to m3.5 were subjected only to the wide MR range models since all of these cases have a MR that crosses upwards or downwards from MR= 1. Regarding Case m3.3, the best results were obtained using the correlations presented by Bordabar et al., being 7.09% for maximum radiative heat source, and 4.72% for radiative heat flux. Mean deviation values for this same WSGG correlation were 4.30%, and 2.86% for radiative heat source, and radiative heat flux, respectively.

Case m3.3 was the only profile where the correlations presented by this paper did not perform better than any of the other two authors correlations. Note that in Case m3.3 occurred the same non-physic behavior that happened in the Case m3.2, even though the MR range for Case m3.3 was smaller. However, this non-physic behavior did not occur on Cases m3.4, and m3.5, which had also a considerably large MR range.

Figures 5.40, and 5.41 illustrates the behavior of the WSGG models in comparison with the LBL integration for Case m3.3.

Figure 5.41 may be intriguing. Note that the plotted results using Table 3.3 seem to work out better. However, note that the results provided by Kang. et al., and Bordbar et al. fit closer to the most part of the curve diverging only close to the walls. Therefore, on average, they perform better.

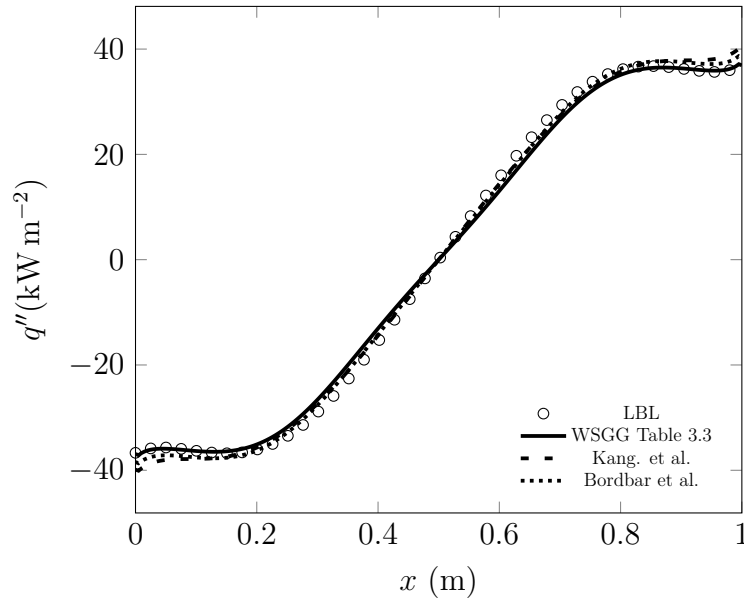


Figure 5.41 – Comparison of results for the radiative heat flux for Case m3.3, where

$$T(x) = [1400 \text{ K} - (400 \text{ K})\cos(2\pi x/X)], Y_{CO_2} = 0.12, \text{ and}$$

$$Y_{H_2O}(x) = [0.12 + 0.09\cos(2\pi x/X)].$$

On Cases m3.4, and m3.5, the correlations from Table 3.3 were the ones with a best overall performance with the only exception being the maximum deviation for the radiative heat source, where the correlations of Bordbar et al. for Case m3.5 returned a 6.66% deviation against 7.33% when using Table 3.3. The other deviations were all smaller than those provided by the two other authors, with an emphasis on the radiative heat flux values, in which the Table 3.3 correlations were around two times better than the others.

For Case m3.4 the maximum deviation for the radiative heat source when using Table 3.3 was 8.85%, and the average was 4.45%. Figure 5.42 shows the comparison of the results for all the models for Case m3.4.

When it comes to the radiative heat flux, the maximum, and average deviations when using Table 3.3 were respectively 4.85%, and 2.63%. Figure 5.43 depicts the behaviors of the four WSGG models against the LBL integrations for the radiative heat flux for Case m3.4.

In the Case m3.5, WSGG correlations from Table 3.3 returned a maximum deviation of 7.33%, and a average of 3.00%. Bordbar et al. correlations, on the other hand, returned 6.06%, maximum, and 3.03%, average. Figure 5.44 presents the plots of the

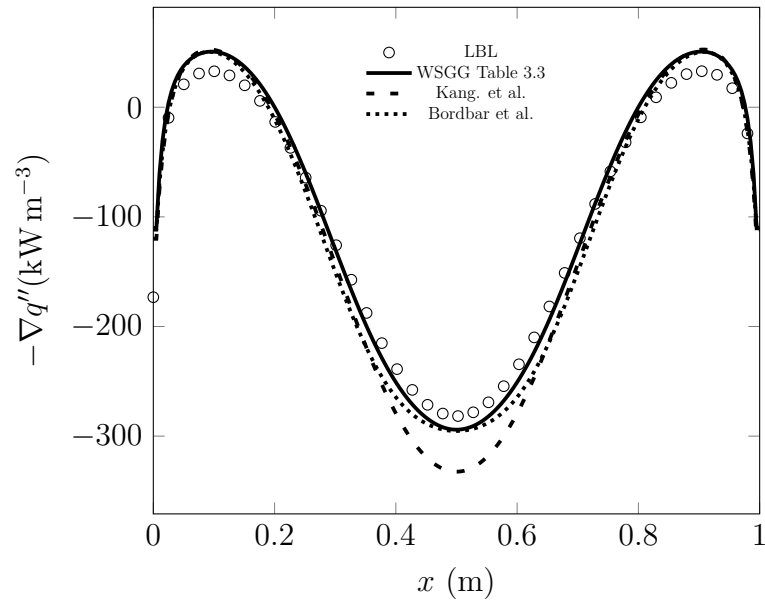


Figure 5.42 – Comparison of results for the radiative heat source for Case m3.4, where $T(x) = [1400\text{ K} - (400\text{ K})\cos(2\pi x/X)]$, $Y_{CO_2}(x) = [0.15 + 0.075\cos(2\pi x/X)]$, and $Y_{H_2O} = 0.15$.

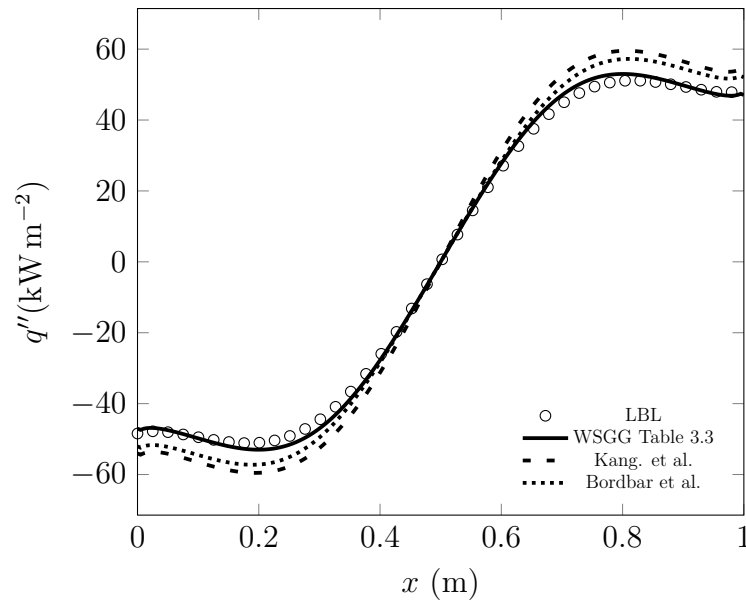


Figure 5.43 – Comparison of results for the radiative heat flux for Case m3.4, where $T(x) = [1400\text{ K} - (400\text{ K})\cos(2\pi x/X)]$, $Y_{CO_2}(x) = [0.15 + 0.075\cos(2\pi x/X)]$, and $Y_{H_2O} = 0.15$.

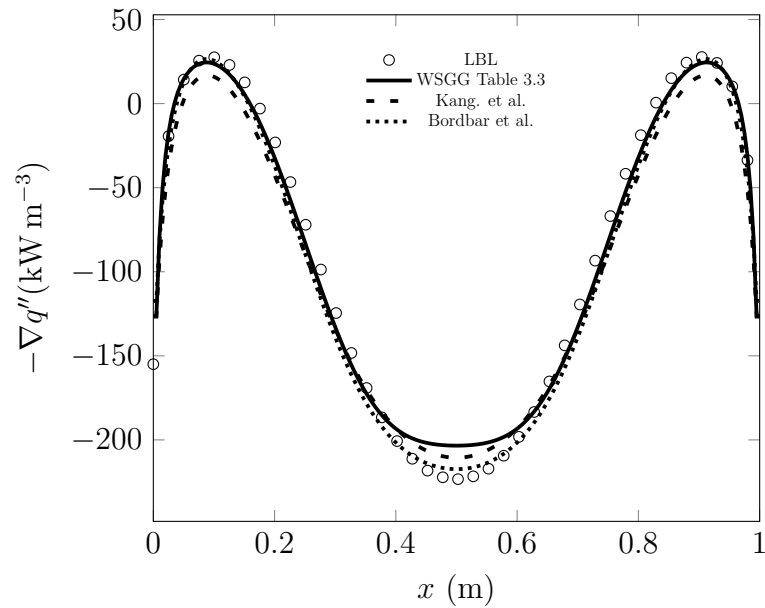


Figure 5.44 – Comparison of results for the radiative heat source for Case m3.5, where

$$T(x) = [1400 \text{ K} - (400 \text{ K})\cos(2\pi x/X)], Y_{CO_2} = 0.15, \text{ and}$$

$$Y_{H_2O}(x) = [0.15 + 0.075\cos(2\pi x/X)].$$

comparison between the WSGG models and the LBL integration for the radiative heat source for Case m3.5.

Regarding the radiative heat flux for Case m3.5, the maximum deviation when using the correlations from Table 3.3 was 3.33%, and the average deviation was 1.68%. Figure 5.45 shows the results for the radiative heat flux for Case m3.5.

For Cases m4.1, and m4.2, the best results were given by the Table 3.4, where the radiative heat flux deviations were significantly smaller than those proposed by Kang. et al., and Bordbar et al. When it comes to the radiative heat source, the deviations were significantly smaller only on case 4.2. In case 4.1, the deviations were just shy smaller from those obtained when using Bordbar et al. correlations. The WSGG correlations from Table 3.3 also performed better than the other authors' correlations, being the maximum deviation value for the radiative heat source the only exception. However, as pointed out before, the best overall results were obtained using the correlations from Table 3.4.

For Case m4.1, the results obtained when using Table 3.3 regarding the radiative heat source were 5.04%, maximum deviation, and 1.24%, average. When using Table 3.4 the maximum and average deviations were respectively 3.47% and 1.44%. The results for the radiative heat source for Case m4.1 are plotted on Figure 5.46.

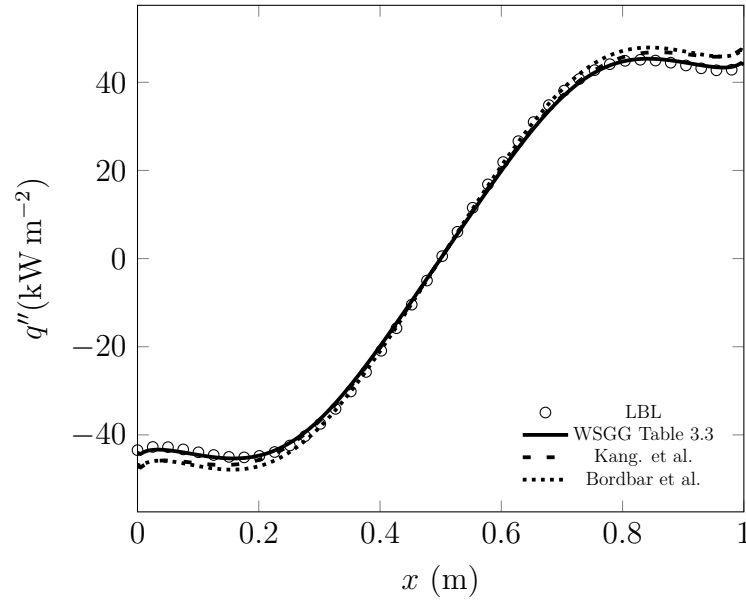


Figure 5.45 – Comparison of results for the radiative heat flux for Case m3.5, where

$$T(x) = [1400 \text{ K} - (400 \text{ K})\cos(2\pi x/X)], Y_{CO_2} = 0.15, \text{ and}$$

$$Y_{H_2O}(x) = [0.15 + 0.075\cos(2\pi x/X)].$$

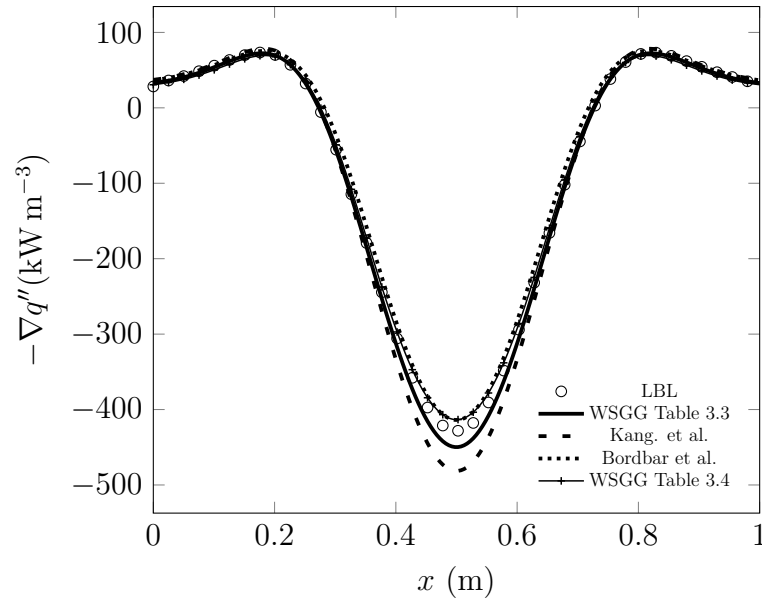


Figure 5.46 – Comparison of results for the radiative heat source for Case m4.1, where

$$T(x) = [400 \text{ K} + (1400 \text{ K})\sin^2(\pi x/X)], Y_{CO_2}(x) = [0.1 + 0.7\sin^2(\pi x/X)], \text{ and}$$

$$Y_{H_2O} = 0.1.$$

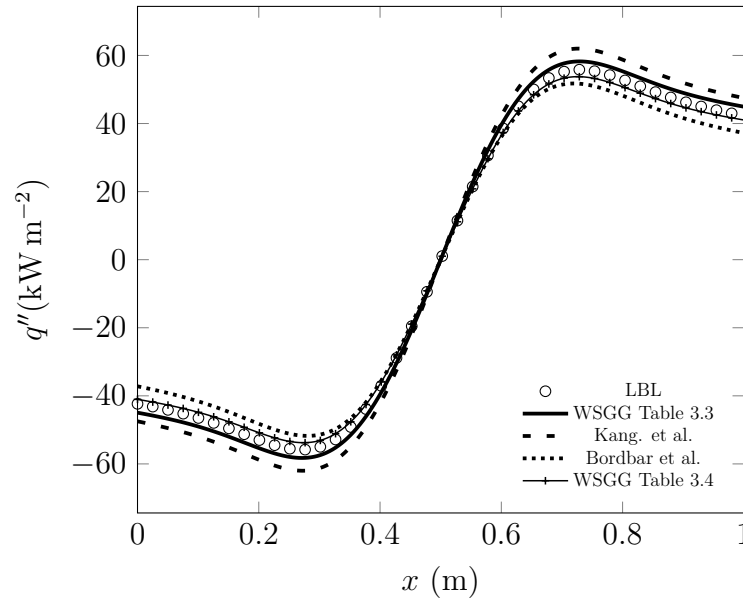


Figure 5.47 – Comparison of results for the radiative heat flux for Case m4.1, where

$$T(x) = [400 \text{ K} + (1400 \text{ K})\sin^2(\pi x/X)], Y_{CO_2}(x) = [0.1 + 0.7\sin^2(\pi x/X)], \text{ and}$$

$$Y_{H_2O} = 0.1.$$

For the radiative heat flux, the maximum and average deviations when using Table 3.3 were 4.72%, and 3.88%, respectively. When using Table 3.4 the maximum and average deviations were respectively 3.88%, and 2.73%. Figure 5.47 compares the results for the radiative heat flux for Case m4.1.

For the Case m4.2, the maximum deviations for the radiative heat source when using Tables 3.3, and 3.4 were 4.04%, and 3.68%. The average deviations were 2.20%, and 1.88%, respectively. Figure 5.48 shows the comparison for the radiative heat source between the WSGG models and the LBL integrations for Case m4.2.

With respect to the radiative heat flux, the maximum and average deviations when using Table 3.3 were respectively 6.36%, and 1.69%. The results obtained when using Table 3.4 were slightly better being 5.51%, maximum deviation, and 1.39%, average deviation. Figure 5.49 presents the results for the radiative heat flux for a graphic comparison between the WSGG models and the LBL integration for Case m4.2.

To summarize the results and make the comparison between all the models it is provided a table. Table 5.2 shows the deviations for the maximum and average (in parenthesis) radiative heat source and radiative heat flux on the 11 cases presented in the varying MR scenario. Like in Table 5.1, there is also two rows at the end of Table

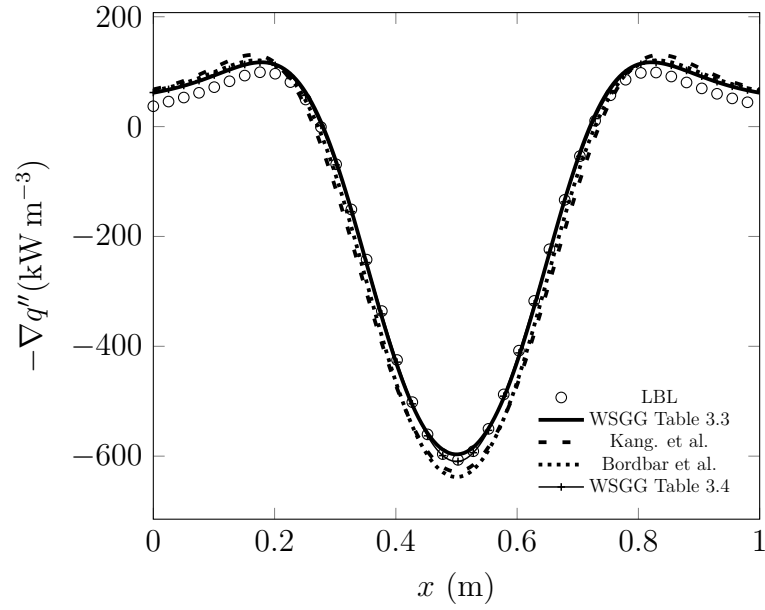


Figure 5.48 – Comparison of results for the radiative heat source for Case m4.2, where

$$T(x) = [400 K + (1400 K)\sin^2(\pi x/X)], Y_{CO_2} = 0.1, \text{ and}$$

$$Y_{H_2O}(x) = [0.1 + 0.3\sin^2(\pi x/X)].$$

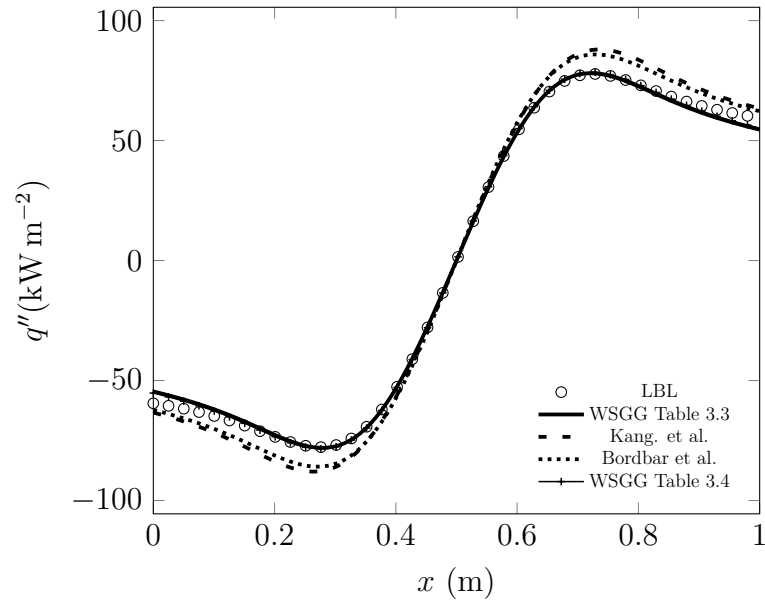


Figure 5.49 – Comparison of results for the radiative heat flux for Case m4.2, where

$$T(x) = [400 K + (1400 K)\sin^2(\pi x/X)], Y_{CO_2} = 0.1, \text{ and}$$

$$Y_{H_2O}(x) = [0.1 + 0.3\sin^2(\pi x/X)].$$

5.2 representing the mean value of the maximum and average deviations of each WSGG correlation.

The results presented in this section evinces that accounting for the MR variation within the WSGG model influences the results obtained for both radiative heat source and flux. The results obtained for a varying partial pressure scenario have shown a weak dependence of the partial pressure variation and the final results when using WSGG models. This finding turned itself even more evident after obtaining good results using WSGG correlations for a varying MR scenario that were fitted for different partial pressures than the partial pressures of the medium on which these correlations were tested.

Moreover, the cases with an extreme MR value have shown that using WSGG correlations for a wide MR range is a disadvantage, for the accuracy considerably diminishes. It seems that it is not a wise approach to increase the extent of the correlations and sacrifice its exactness, for the real problems may not have such wide MR variations.

Table 5.2 – Maximum and (Average) Deviations from LBL calculations for cases using the correlations from Tables 3.3 and 3.4, in percentage (%).

Case	Heat Source				Heat Flux			
	WSSG Table3.3	WSSG Table3.4	Kang. et al.	Bordbar et al.	WSSG Table3.3	WSSG Table3.4	Kang. et al.	Bordbar et al.
m1.1	4.14 (0.73)	2.91 (0.37)	15.09 (1.72)	9.39 (0.40)	9.26 (3.40)	4.72 (1.85)	21.96 (8.32)	2.06 (0.83)
m1.2	5.33 (0.36)	1.00 (0.12)	7.81 (0.71)	7.33 (1.22)	2.35 (1.09)	0.92 (0.53)	6.94 (1.97)	11.75 (4.05)
m2.1	8.87 (3.85)	2.17 (0.96)	11.46 (5.67)	4.71 (3.83)	9.95 (7.38)	3.92 (1.01)	13.85 (10.06)	13.40 (6.53)
m2.2	3.98 (1.37)	4.24 (1.26)	5.27 (2.02)	3.59 (2.10)	4.29 (1.93)	3.95 (0.70)	3.05 (1.17)	4.10 (2.84)
m3.1	9.17 (3.71)	1.38 (0.42)	12.80 (5.71)	4.91 (3.11)	11.78 (9.05)	1.17 (0.21)	16.26 (12.15)	11.86 (6.16)
m3.2	14.53 (7.24)	12.85 (6.58)	18.97 (8.70)	18.80 (8.37)	9.52 (5.50)	8.98 (5.20)	18.59 (12.73)	17.40 (10.78)
m3.3	13.67 (5.12)	-	8.69 (5.59)	7.09 (4.30)	7.52 (3.44)	-	8.64 (3.47)	4.72 (2.86)
m3.4	8.85 (4.45)	-	18.01 (8.21)	11.39 (6.17)	4.85 (2.63)	-	16.80 (12.35)	12.04 (7.85)
m3.5	7.33 (3.00)	-	7.48 (4.56)	6.66 (3.03)	3.33 (1.68)	-	8.12 (3.12)	7.32 (3.56)
m4.1	5.04 (1.24)	3.47 (1.44)	12.42 (3.43)	4.96 (2.39)	4.72 (3.88)	3.88 (2.73)	11.13 (9.02)	9.21 (6.26)
m4.2	4.04 (2.20)	3.68 (1.88)	9.99 (5.76)	7.71 (4.51)	6.36 (1.69)	5.51 (1.39)	13.69 (8.25)	10.58 (6.86)
Mean	7.72 (3.02)	3.96 (1.63)	11.64 (4.73)	7.87 (3.58)	6.72 (3.79)	4.13 (1.70)	12.58 (7.51)	9.49 (5.33)

6 FINAL COMMENTS AND CONCLUSIONS

This work proposed a method to obtain WSGG correlations for varying partial pressures or mole ratios based on the paper by Wang and Xuan [2019]. It was expected, that accounting for the varying partial pressure on the weighting function, w_i , over a pressure-path-length, would yield better results in comparison with correlations that account only for the temperature in the weighting function. In reality, for the majority of cases with varying partial pressure, the model proposed by this work performed better. However, the cases with larger partial pressure variations showed results that were skewed towards the correlation from Dorigon et al., which in turn bases its weighting function solely on temperature.

To put in numbers, if the total of cases for a varying partial pressure is considered, the correlations presented by this work performed better in 50% of times regarding the average radiative heat source, 70% to the average radiative heat flux, 40% in regards of the maximum radiative heat source, and 50% concerning the maximum radiative heat flux. Conversely, if only the cases with a larger partial pressure variation are considered, the correlations presented by this work performed better in 50% of times regarding the average radiative heat source, 75% with respect to the average radiative heat flux, 25% in regards of the maximum radiative heat source, and 25% concerning the maximum radiative heat flux.

This skewness towards the results obtained when using Dorigon et al. correlations for the profiles with a higher partial pressure variation might be fortuitous, for Dorigon et al. fitted the WSGG model only for temperature variations. On the other hand, this fact cannot be neglected. If the dependence of the WSGG model on the partial pressure were higher than the uncertainty added by using a second weighting factor, then the results obtained when using such correlations would have been better than those yielded from Dorigon et al. correlations.

This way, it is concluded by this work that, adding an extra weighting factor into the weighting function does not bring a clear advantage when it comes to profiles with varying partial pressure insofar the MR of the WSGG correlations is the same of the medium. It is relevant to point out, though, that the correlations presented by this work provided very satisfactory results, and the fact that the comparisons were made against

a well-behaved set of coefficients may have contributed to these minor improvements.

In another development, this work investigated the possible improvements when accounting for the variation of the mole ratio along a given pressure-path-length. While the differences between the results yielded by the correlations from this work and Dorigon et al. were not impressive, the same does not hold when it comes to the comparison among the correlations for a medium with a varying mole ratio, especially for the radiative heat flux. In a few cases, however, the correlations proposed for a MR range of 0.125-4.0 performed worse than the correlations from Bordbar et al. [2014].

Quantitatively, the WSGG correlation for an MR range of 0.125-4.0 performed better in 7 out of 11 cases, 64% of times, in respect of the average radiative heat source and flux. Regarding the maximum radiative heat source, and radiative heat flux, the coefficients provided by this work performed better in 5 out of 11 cases, 45% of times, and 8 out of 11, 73% of times, respectively.

From the last two paragraphs, it is possible to conclude that the correlations presented by this work provided better results in general and, if the results were not the better, the deviations from other models were not too pronounced. However, as mentioned in Section 5.2.2, some of the profiles presented deviations that should not be considered good. It happens partly because of the medium profile itself, partly due to the wide range for which the correlations were fitted. As a way to address this issue, this work provided two sets of coefficients for smaller MR ranges of 0.125-1.0, and 1.0-4.0.

The correlations for a narrow MR range performed better in 7 out of 8 cases, concerning the maximum radiative heat source. About the average radiative heat source, these correlations performed better than all of the other WSGG correlations. Similarly, the performance of these correlations were better in 6 out of 8 cases, 75% of times, for the maximum radiative heat flux, and 88% of times for the average radiative heat flux. Note that the deviations provided by the narrow MR range correlations were also significantly smaller.

The results obtained when using these correlations of smaller MR ranges were far better than what was expected, in a way that bears questioning the real necessity and applicability of profiles with such wide MR variations. It seems unlikely real oxy-fuel combustions where the medium would change from being predominantly composed by CO_2 to being composed mainly by H_2O , or vice-versa.

Concerning this matter, this work provided evidence supporting the use of two separated WSGG correlations for media with a varying MR, one for $MR < 1$, and other for $MR > 1$. Although they were used only in one profile that shows the non-physical behavior, the WSGG coefficients for a narrow MR range were the only correlations that did not cause the occurrence of the non-physical behavior in the middle of the domain for the radiative heat source. Therefore, they might be less susceptible to unexpected behaviors. Also, the split correlations demonstrated a very stable solution for the profile with a low MR range, described by Kangwanpongpan et al., 2012, as a real oxy-fuel scenario.

Finally, the WSGG coefficients provided by this work for varying MR scenarios seem to be more adequate, even in an unlikely situation where the MR range crosses upwards or downwards the mark of 1, especially if the main task is the final result for the radiative heat flux.

6.1 Possibilities for Future Work

After considering the findings, this work proposes the following further research:

- Test the new correlations for profiles with two-dimensional domains to check their respective robustness in more complex profiles;
- Verify the possibility, and viability of improving the narrow MR range correlations in terms of pressure-path-length and spectral resolution;
- Include the total pressure variable in addition to the mole ratio and the temperature into the weighting function, and check the resultant accuracy;
- Verify the importance of the pressure-path-length range in the final precision of the WSGG correlations.

BIBLIOGRAPHIC REFERENCES

Procedure for Estimation and Reporting of Uncertainty Due to Discretization in CFD Applications, **Journal of Fluids Engineering**, vol. 130(7), 2008.

Bhatia, V. **Textbook of Astronomy and Astrophysics with Elements of Cosmology**. CRC Press, 2001.

Bordbar, M. H., Weel, G., and Hyppänen, T. A line by line based weighted sum of gray gases model for inhomogeneous CO₂H₂O mixture in oxy-fired combustion, **Combustion and Flame**, vol. 161(9), p. 2435 – 2445, 2014.

Brittes, R. d. S. **Desenvolvimento de um novo modelo para integração espectral da RTE em problemas não homogêneos e não isotérmicos**. Tese de doutorado, Universidade Federal do Rio Grande do Sul, 2015.

Cassol, F., Brittes, R., Centeno, F. R., da Silva, C. V., and França, F. H. R. Evaluation of the gray gas model to compute radiative transfer in non-isothermal, non-homogeneous participating medium containing CO₂, H₂O and soot, **Journal of the Brazilian Society of Mechanical Sciences and Engineering**, vol. 37(1), p. 163–172, 2015.

Cassol, F., Brittes, R., França, F. H., and Ezekoye, O. A. Application of the weighted-sum-of-gray-gases model for media composed of arbitrary concentrations of H₂O, CO₂ and soot, **International Journal of Heat and Mass Transfer**, vol. 79, p. 796 – 806, 2014.

Chandrasekhar, S. **Radiative Transfer**. Dover, 1960.

Coelho, F. R. and França, F. H. WSGG correlations based on HITEMP2010 for gas mixtures of H₂O and CO₂ in high total pressure conditions, **International Journal of Heat and Mass Transfer**, vol. 127, p. 105 – 114, 2018.

Dorigon, L. J., Duciak, G., Brittes, R., Cassol, F., Galarça, M., and França, F. H. WSGG correlations based on HITEMP2010 for computation of thermal radiation in non-isothermal, non-homogeneous H₂O/CO₂ mixtures, **International Journal of Heat and Mass Transfer**, vol. 64, p. 863 – 873, 2013.

Edwards, D. K. and Menard, W. A. Comparison of Models for Correlation of Total Band Absorption, **Appl. Opt.**, vol. 3(5), p. 621–625, 1964.

Fischer, J., Gamache, R., Goldman, A., Rothman, L., and Perrin, A. Total internal partition sums for molecular species in the 2000 edition of the HITRAN database, **Journal of Quantitative Spectroscopy and Radiative Transfer**, vol. 82(1-4), p. 401–412, 2003.

Hottel, H. and Sarofim, A. Radiative transport, **McCravv Hill, New York**, vol. , 1965.

Hottel, H. C. **Radiant Heat Transmission**. In McAdams, W. H., editor, Heat Transmission. McGraw-Hill Book Company, New York, 3rd edition, 1954.

Howell, J., Menguc, M., and Siegel, R. **Thermal Radiation Heat Transfer**. CRC Press, 2015.

IBM. **SPSS Modeler 18.0 Documentation**. <https://www.ibm.com/support/pages/spss-modeler-180-documentation#en>, 2020. Acesso em: 11-04-2020.

IEA. **Total primary energy supply by fuel, 1971 and 2017**. <https://www.iea.org/data-and-statistics/charts/total-primary-energy-supply-by-fuel-1971-and-2017>, 2017. Acesso em: 03-02-2020.

Incropera, F., DeWitt, D., Bergman, T., and Lavine, A. **Fundamentals of Heat and Mass Transfer**. Wiley, 2007.

Johansson, R., Leckner, B., Andersson, K., and Johnsson, F. Account for variations in the H₂O to CO₂ molar ratio when modelling gaseous radiative heat transfer with the weighted-sum-of-grey-gases model, **Combustion and Flame**, vol. 158(5), p. 893 – 901, 2011.

Kangwanpongpan, T., França, F. H., da Silva, R. C., Schneider, P. S., and Krautz, H. J. New correlations for the weighted-sum-of-gray-gases model in oxy-fuel conditions based on HITEMP 2010 database, **International Journal of Heat and Mass Transfer**, vol. 55(25), p. 7419 – 7433, 2012.

Marquardt, D. W. An Algorithm for Least-Squares Estimation of Nonlinear Parameters, **Journal of the Society for Industrial and Applied Mathematics**, vol. 11(2), p. 431–441, 1963.

Mazurek, R. d. S. **Evaluation of the WSGG and SLW models for the radiative transfer prediction in non-isothermal homogeneous and non-homogeneous media**. Dissertação de mestrado, Universidade Federal do Rio Grande do Sul, 2019.

Modest, M. F. The Weighted-Sum-of-Gray-Gases Model for Arbitrary Solution Methods in Radiative Transfer, **Journal of Heat Transfer**, vol. 113(3), p. 650–656, 1991.

Modest, M. F. **Radiative heat transfer**. Academic press, 2013.

Neter, J., Kutner, M. H., Nachtsheim, C. J., and Wasserman, W. **Applied Linear Statistical Models**. Irwin, Chicago, 1996.

Rothman, L., Gordon, I., Barber, R., Dothe, H., Gamache, R., Goldman, A., Perevalov, V., Tashkun, S., and Tennyson, J. HITEMP, the high-temperature molecular spectroscopic database, **Journal of Quantitative Spectroscopy and Radiative Transfer**, vol. 111(15), p. 2139 – 2150, 2010.

Rothman, L. S., Wattson, R. B., Gamache, R., Schroeder, J. W., and McCann, A. **HITRAN HAWKS and HITEMP: high-temperature molecular database**. In Dainty, J. C., editor, *Atmospheric Propagation and Remote Sensing IV*, vol. 2471, p. 105 – 111. International Society for Optics and Photonics, SPIE, 1995.

Smith, T. F., Shen, Z. F., and Friedman, J. N. Evaluation of Coefficients for the Weighted Sum of Gray Gases Model, **Journal of Heat Transfer**, vol. 104(4), p. 602–608, 1982.

Wang, A. and Modest, M. F. Importance of Combined Lorentz-Doppler Broadening in High-Temperature Radiative Heat Transfer Applications, **Journal of Heat Transfer**, vol. 126(5), p. 858–861, 2004.

Wang, B. and Xuan, Y. An improved WSGG model for exhaust gases of aero engines within broader ranges of temperature and pressure variations, **International Journal of Heat and Mass Transfer**, vol. 136, p. 1299 – 1310, 2019.

Wang, P., Fan, F., and Li, Q. Accuracy evaluation of the gray gas radiation model in CFD simulation, **Case Studies in Thermal Engineering**, vol. 3, p. 51 – 58, 2014.

Ziemniczak, A. **Geração de novas correlações da soma-ponderada-de-gases-cinza para espécies individuais de gases participantes**. Dissertação de mestrado, Universidade Federal do Rio Grande do Sul, 2014.

APPENDIX A – WSGG Coefficients for Other Configurations

A.1 Varying MR

Table A.1 – WSGG Correlations for a varying MR with $p_{H_2O} + p_{CO_2} = 1$

i	1	2	3	4
$k_{p,i}(atm^{-1}m^{-1})$	1.83102×10^{-1}	1.68029×10^0	1.09974×10^1	1.30561×10^2
$c_{i,0}$	1.80066×10^{-1}	2.58400×10^{-1}	5.33847×10^{-1}	8.21148×10^{-1}
$c_{i,1}$	1.26540×10^0	6.76020×10^{-1}	3.62651×10^{-1}	-9.93379×10^{-1}
$c_{i,2}$	-1.16789×10^0	-4.17270×10^{-1}	-6.55053×10^{-1}	6.17547×10^{-1}
$c_{i,3}$	3.64236×10^{-1}	4.74353×10^{-2}	2.11390×10^{-1}	-1.70697×10^{-1}
$c_{i,4}$	-	-	-	-
$c_{i,5}$	-	-	-	-
$c_{i,6}$	-4.65925×10^{-3}	6.72352×10^{-4}	-2.23918×10^{-3}	2.13366×10^{-3}
$d_{i,0}$	5.20696×10^{-1}	1.95170×10^{-1}	1.61337×10^{-1}	1.96870×10^{-1}
$d_{i,1}$	1.45748×10^{-1}	5.08562×10^{-1}	2.57504×10^{-1}	3.23957×10^{-2}
$d_{i,2}$	-9.13278×10^{-2}	-2.43616×10^{-1}	-8.88919×10^{-2}	-2.20912×10^{-2}
$d_{i,3}$	-	-	-	-
$d_{i,4}$	7.28863×10^{-3}	1.66380×10^{-2}	4.62223×10^{-3}	1.56020×10^{-3}
$d_{i,5}$	-	-	-	-
$d_{i,6}$	-2.34007×10^{-4}	-5.08278×10^{-4}	-1.27992×10^{-4}	-4.72009×10^{-5}